Aalborg Universitet

Silicon Heterojunction Solar Cells with Transition Metal Oxide as the Hole Transport Layers

Li, Fengchao

Publication date:
2020

Document Version
Publisher's PDF, also known as Version of record

Link to publication from Aalborg University

Citation for published version (APA):
Li, F. (2020). *Silicon Heterojunction Solar Cells with Transition Metal Oxide as the Hole Transport Layers*. Aalborg Universitetsforlag. Ph.d.-serien for Det Ingeniør- og Naturvidenskabelige Fakultet, Aalborg Universitet

General rights
Copyright and moral rights for the publications made accessible in the public portal are retained by the authors and/or other copyright owners and it is a condition of accessing publications that users recognise and abide by the legal requirements associated with these rights.

? Users may download and print one copy of any publication from the public portal for the purpose of private study or research.
? You may not further distribute the material or use it for any profit-making activity or commercial gain
? You may freely distribute the URL identifying the publication in the public portal ?

Take down policy
If you believe that this document breaches copyright please contact us at vbn@aub.aau.dk providing details, and we will remove access to the work immediately and investigate your claim.

Downloaded from vbn.aau.dk on: August 24, 2021

SILICON HETEROJUNCTION SOLAR CELLS WITH TRANSITION METAL OXIDE AS THE HOLE TRANSPORT LAYERS

BY
FENGCHAO LI

DISSERTATION SUBMITTED 2020

AALBORG UNIVERSITY
DENMARK

SILICON HETEROJUNCTION SOLAR CELLS WITH TRANSITION METAL OXIDE AS THE HOLE TRANSPORT LAYERS

by

Fengchao Li

AALBORG UNIVERSITY
DENMARK

Dissertation submitted

.

Dissertation submitted: 31-8-2020

PhD supervisor: Associate Prof. Donghong Yu,
Aalborg University

Assistant PhD supervisor: Prof. Fengzhen Liu,
University of Chinese Academy of Sciences,

PhD committee: Associate Professor Casper Steinmann (chairman)
Aalborg University

Professor Morten Madsen
University of Southern Denmark

Associate Professor Stefano Polizzi
Ca'Foscari University of Venice

PhD Series: Faculty of Engineering and Science, Aalborg University

Department: Department of Chemistry and Bioscience

ISSN (online): 2446-1636
ISBN (online): 978-87-7210-803-2

Published by:
Aalborg University Press
Kroghstræde 3
DK – 9220 Aalborg Ø
Phone: +45 99407140
aauf@forlag.aau.dk
forlag.aau.dk

© Copyright: Fengchao Li

Printed in Denmark by Rosendahls, 2020

CV

Fengchao Li was born on June 9th, 1988 in Wenshui County, Lvliang City, Shanxi Province, China,who is a joint Ph.D. student of Aalborg University and University of Chinese Academy of Sciences under the Double Ph.D Program at the Sino-Danish Center for Education and Reasarch. He carried out doctoral research and studied in the Department of Chemistry and bioscience, Faculty of Engineering and Science, Aalborg Unversity.

Silicon heterojunction solar cells with transition metal oxide as the hole transport layers

ENGLISH ABSTRACT

Novel silicon heterojunction (SHJ) solar cells with dopant-free asymmetric heterocontacts have gained great attention in photovoltaic technology in recent years. Transition metal oxides (TMO), represented by MoO_x, WO_x, and VO_x, have been widely used as hole transport layers (HTLs) in them due to their wide bandgap, large work function (⩾6.0 eV), and high optical transmittance. This PhD thesis focused on fabrication and characterization of different TMO materials, and their optimization as HTLs for SHJ solar cells, including charge transport mechanisms.

A novel hot wire oxidation–sublimation deposition (HWOSD) technique, as an optimal technology, was developed to fabricate MoO_x,WO_x, and VO_x thin films. The effects of hot wire temperature, oxygen pressure, and annealing temperature on morphology, microstructure, composition, and opto-electronic properties of the TMO films were systematically studied. The amorphous TMO films with smooth surface, uniform thickness, and excellent photo-electric properties were obtained. The "conformal" coverage was realized on the textured silicon substrate. The results of XPS confirm that the ratio of oxygen to transition metal in MoO_x, WO_x, and VO_x are 2.94, 2.91, and 2.32, respectively. TMO films possess good optical transmittance, especially the average transmittance of WO_x film in the range of 300-1200 nm reaches 97.46%. The conductivity of MoO_x and WO_x thin films is 2.58×10^{-6} S/cm and 5.14×10^{-7} S/cm, respectively. MoO_x thin films exhibit good field passivation effects on the i a-Si:H /c-Si/i a-Si:H structured wafers, whose minority carrier lifetime is 1.3 ms. The KPM result indicates that MoO_x and WO_x have significantly different contact potential, when n-Si is contacted with MoO_x and WO_x. The results show that MoO_x, WO_x, and VO_x films fabricated by HWOSD have the potential to be used as excellent HTLs for SHJ solar cells.

The photovoltaic performance of SHJ solar cells with MoO_x as HTL was systematically optimized from three aspects: interface passivation layer, film thickness, and annealing process. It is found that i a-Si:H had the best passivation effect at MoO_x/Si interface, and the SiO_x layer obtained by UV-O_3 treatment also showed good passivation potential. The SHJ solar cell with a power conversion efficiency (PCE) of 21.10% (V_{OC}: 713 mV, J_{SC}: 37.50 mA/cm^2, and FF: 78.92%) was obtained at the thickness of 14 nm MoO_x film by pre-annealing-HF process. Compared with the SHJ solar cells with WO_x or VO_x as HTLs, the ones with MoO_x as HTL pronounced the best performance. In addition to the work function of TMO films, the density and its distribution of the defect states in the bulk and at the interface are important factors affecting the performance of WO_x and VO_x solar cells. WO_x as antireflective layer and MoO_x as HTL were applied to fabricate the lithography-free

and dopant-free back-contact SHJ solar cells, which obtained PCE of 20.24% (V_{OC}: 696 mV, J_{SC}: 38.61 mA/cm^2, and FF: 75.31%).

The charge transport mechanism of heterojunction solar cells with MoO_x, WO_x and VO_x as HTLs were studied based on the measurement and analysis of high frequency *C-V*, dark *J-V* and dark *J-V-T* characteristics of the solar cells. The *C-V* fitting results indicated the MoO_x solar cell's potential V_D and barrier width X_D are 0.76 V and 0.368 μ m, 0.67 V and 0.277 μ m for WO_x solar cell, 0.56 V and 0.188 μ m for VO_x solar cell, respectively. The relationship between $1/C^2$ and voltage revealed the trends of the defect-state density at interfaces was $MoO_x < WO_x < VO_x$. The dark *J-V* curves of the three solar cells were fitted by the double diode model. In the voltage region of $0.4\ V < V < 0.6\ V$, the *J-V* relationship basically conforms to the ideal diode characteristics (ideal factor n ~ 1). In the voltage region of $0.15\ V < V < 0.4\ V$, the three solar cells have larger ideal factors (n = 3.68, 3.62, and 3.76), which indicate that the transport mechanism of the novel heterojunction may be different from the depletion recombination current (n ~ 2). The *J-V-T* characteristics of heterojunction solar cells with MoO_x, WO_x, and VO_x as HTLs were analyzed. It is found that the current density has the characteristic of tunneling current in the low voltage region, whose the factor A_1 is independent on temperature, while the average value of ideal factor n is large with no definite value. In the high voltage region, the current density conforms to the ideal diode law. Based on the junction characteristic and *J-V-T* characteristics of MoO_x /silicon heterojunction, the *J-V-T* curve of MoO_x /Si heterojunction solar cells were simulated by using the electron thermionic current density J_{Te} and the tunneling current density J_{Tu} representing the thermionic emission and thermal-assisted tunneling process of electrons and the defect assisted tunneling process of holes, respectively. The simulation results showed that the effective barrier height φ_{Bn}=0.98eV at the interface of MoO_x / silicon heterojunction presented both strong inversion region being formed on the surface of crystalline silicon and the high inversion barrier indicating high potential V_{OC}. The barrier height obtained by fitting was basically consistent with the built-in potential of MoO_x /Si heterostructure determined by *C-V* measurement ($\varphi_{Bn} \approx V_D + (E_c - E_F)$). According to the simulation results, we believe that MoO_x /Si heterostructure is a Schottky-like junction with high barrier or strong inversion characteristic. The lower barrier height of WO_x and VO_x devices implied that the surface of crystalline silicon was not strong inversion, which may be related to the Fermi level pinning caused by the high density of states of interface defects.

Keywords: Transition metal oxide films, Materials characterization, Silicon heterojunction solar cells, Transport mechanism.

CHINAESE ABSTRACT

以 MoO_x、WO_x 和 VO_x 为代表的过渡金属氧化物（TMO）以其较宽的禁带宽度，较大的功函数（≥6.0 eV）以及高透过率被作为空穴选择传输层(HTLs)，广泛地应用于新型硅异质结太阳电池中，是近年来光伏领域的研究热点之一。但该类太阳电池目前仍然存在以下问题需要解决：（1）缺少适合产业化推广的优质氧化物薄膜的制备方法。（2）该类器件的输运机制有待进一步研究。本论文提出并采用热丝氧化升华沉积法来制备 TMO 薄膜，从 TMO 薄膜材料的制备与表征、以 TMO 为 HTLs 的硅异质结太阳电池的性能优化和该类太阳电池的输运机制三个方面展开研究。

系统地研究了热丝温度、氧气压和退火温度等工艺条件对 TMO 薄膜的形貌、微结构、成分、光电性能的影响，得到了表面光滑、厚度均匀、光电性能优良的非晶 TMO 薄膜，并在织构晶硅衬底上实现了“保角”覆盖。XPS 分析得到 MoO_x、WO_x 及 VO_x 中氧与过渡金属比例分别为 2.94、2.91 和 2.32；三种 TMO 薄膜都具有好的光透性。MoO_x 薄膜对 i a-Si:H/c-Si/i a-Si:H 结构的硅片表现出了好的场钝化效应，样品少子寿命达 1.3 ms；KPM 测试表明 MoO_x 和 WO_x 与 n-Si 接触时存在显著的接触电势差。以上研究结果表明，采用热丝氧化升华沉积法制备的 MoO_x、WO_x 和 VO_x 薄膜具备成为硅异质结太阳电池空穴选择传输层的潜力。

从界面钝化层、薄膜厚度和退火工艺三个方面对以 MoO_x 为 HTL 的硅异质结太阳电池性能进行了系统优化。比较了包括 i a-Si:H、SiO_x 和 i a-Si:H/SiO_x 在内的三种钝化层对 MoO_x/Si 界面的钝化作用，发现 i a-Si:H 具有最好的钝化效果，而 i a-Si:H/SiO_x 复合层使器件性能下降，在后续工艺中需要避免界面处 SiO_x 的形成。采用前退火-HF 处理工艺（Pre-annealing-HF），在 MoO_x 薄膜厚度为 14 nm 时得到了光电转换效率为 21.10%（V_{OC} 为 713 mV，J_{SC} 为 37.50 mA/cm^2，FF 为 78.92%）的硅异质结太阳电池。相比于以 WO_x 或 VO_x 为 HTLs 的硅异质结太阳电池，以 MoO_x 为 HTL 的硅异质结太阳电池表现最优。除了功函数，材料和界面处的缺陷态密度和分布是影响 WO_x 和 VO_x 电池性能的重要因素。将 WO_x 作为减反层和 MoO_x 作为 HTL 应用于新型免光刻背接触硅异质结太阳电池，该器件具有良好的性能表现：V_{OC} 为 696 mV，J_{SC} 为 38.61 mA/cm^2, FF 为 75.31%，Eff 为 20.24%。

结合太阳电池的高频 *C-V* 和暗态 *J-V-T* 等测试分析，对以 MoO_x、WO_x 或 VO_x 为 HTLs 的硅异质结太阳电池的载流子输运机制进行了研究。在 0.4 V＜V＜0.6 V 电压范围，电池的 *J-V* 关系基本符合理想二极管特性；在 0.15 V＜V＜0.4 V 电压区域，三种电池都具有较大的理想因子（室温下 n 分别为：3.68, 3.62 和 3.76），电流密度具有隧穿电流的特点（因子 A_1 不随温度变化，n 值很大且随

温度变化）。用热激活电流密度 J_{Te} 代表电子的热发射和热辅助隧穿过程，用隧穿电流密度 J_{Tu} 表示空穴的缺陷态辅助隧穿过程，对 MoO_x/晶硅异质结太阳电池的 *J-V-T* 曲线进行了模拟。模拟给出 MoO_x/晶硅异质结界面的势垒 φ_{Bn}=0.98eV，表明晶硅表面形成强反型区域，高的反型势垒使得该类太阳电池具有高 V_{OC} 的潜力。拟合得到的势垒高度与 *C-V* 测试确定的 MoO_x/晶硅异质的内建电势基本符合（$q\varphi_{Bn}\approx V_D+(E_c-E_F)$）。根据模拟结果，我们认为 MoO_x/晶硅异质结为多子和少子协同工作的具有高势垒或强反型特征的类肖特基器件。拟合得到的 WO_x 及 VO_x 器件的势垒比较低，表明晶硅表面并未达到强反型，这可能是与界面缺陷态密度过高引起的费米能级钉扎有关。

关键词：过渡金属氧化物薄膜，材料特性，硅异质结太阳电池，输运机制；

DANSK RESUME

Nye silicium heterojunction (SHJ) solceller med dopantfri asymmetriske heterokontakter har fået stor opmærksomhed inden for solcellerteknologi i de senere år. Overgangsmetaloxider, transition metal oxides (TMO), repræsenteret af MoO_x, WO_x og VO_x, er blevet brugt i vid udstrækning som hultransportlag (HTL'er) i dem på grund af deres brede båndgap, store arbejdsfunktion ($\geq$6,0 eV) og høj optisk transmission. Denne ph.d.-afhandling fokuserede på fabrikation og karakterisering af forskellige TMO-materialer og deres optimering som HTL'er for SHJ solceller, inklusive ladetransportmekanismer. SHJ solceller fra ultratynde siliciumfilm og dens blev også undersøgt.

En ny hot wire oxidation-sublimation deposition (HWOSD) teknik, som en optimal teknologi, blev udviklet til at fremstille tynde film MoO_x, WO_x og VO_x. Virkningerne af varmetrådstemperatur, iltryk og annealingtemperatur på morfologi, mikrostruktur, sammensætning og optoelektroniske egenskaber af TMO-filmene blev systematisk undersøgt. De amorfe TMO-film med glat overflade, ensartet tykkelse og fremragende fotoelektriske egenskaber blev opnået. Den "konforme" dækning blev realiseret på det teksturerede siliciumsubstrat. Resultaterne af XPS bekræfter, at forholdet mellem ilt og overgangsmetal i MoO_x, WO_x og VO_x er henholdsvis 2,94, 2,91 og 2,32. TMO-film har god optisk transmittans, især når WO_x-filmens gennemsnitlige transmission i intervallet 300-1200 nm 97,46%. Konduktiviteten for tynde film af MoO_x og WO_x er henholdsvis $2{,}58\times10^{-6}$ S/cm og $5{,}14\times10^{-7}$S cm. MoO_x-tynde film udviser gode feltpassiveringseffekter på i a-Si:H/c-Si/i a-Si:H-strukturerede wafere, hvis minoritetsbærerlevetid er 1,3 ms. KPM-resultatet indikerer, at MoO_x og WO_x har signifikant forskellige kontaktpotentialer, når n-Si bringes i kontakt med MoOx og WOx. Resultaterne viser, at MoO_x, WO_x og VO_x film, der er fremstillet af HWOSD, har potentialet til at blive brugt som fremragende HTL'er til SHJ solceller.

Den fotovoltaiske ydeevne af SHJ-solceller med MoO_x som HTL blev systematisk optimeret ud fra tre aspekter: interface-passiveringslag, filmtykkelse og annealingproces. Det har vist sig, at i a-Si:H havde den bedste passiveringseffekt ved MoO_x/Si-grænseflade, og SiO_x-laget opnået ved UV-O_3-behandling viste også godt passiveringspotentiale. SHJ-solcellen med en effektkonverteringseffektivitet (PCE) på 21,10% (V_{OC}: 713 mV, J_{SC}: 37,50 mA/cm^2 og FF: 78,92%) blev opnået ved tykkelsen på 14 nm MoO_x-film ved præ-annealing-HF behandle. Sammenlignet med SHJ solceller med WO_x eller VO_x som HTL'er, udtalte dem med MoO_x som HTL den bedste ydeevne. Foruden arbejdsfunktionen af TMO-film er densiteten og dens fordeling af defekttilstandene i bulk og ved grænsefladen vigtige faktorer, der påvirker ydeevnen for WO_x og VO_x solceller. WO_x som antireflekterende lag og MoO_x som

HTL blev anvendt til at fremstille de litografifrie og dopantfri back-contact SHJ solceller, der opnåede PCE på 20,24% (V_{OC}: 696 mV, J_{SC}: 38,61 mA/cm^2 og FF: 75,31 %).

Ladningstransportmekanismen for heterojunction solceller med MoO_x, WO_x og VO_x som HTL'er blev undersøgt baseret på måling og analyse af højfrekvente *C*-*V*, mørke *J*-*V* og mørke *J*-*V*-*T* egenskaber af solcellerne. Resultaterne af *C*-*V*-tilpasning viste, at MoO_x-solcellens potentielle V_D og barrierebredde X_D er 0,76 V og 0,368 μm, 0,67 V og 0,277 μm for henholdsvis WO_x-solcelle, 0,56 V og 0,188 μm for VO_x-solcelle. Forholdet mellem 1/C^2 og spænding afslørede tendenser for defekt-tilstand tæthed ved grænseflader var $MoO_x < WO_x < VO_x$. De mørke *J*-*V*-kurver fra de tre solceller blev monteret efter dobbeltdiodmodellen. I spændingsområdet på $0,4V < V < 0,6$ V svarer *J*-*V*-forholdet grundlæggende til de ideelle diodeegenskaber (ideel faktor n ~ 1). I spændingsområdet på $0,15\ V < V < 0,4$ V har de tre solceller større ideelle faktorer (n = 3,68, 3,62 og 3,76), som indikerer, at transportmekanismen for den nye heterojunktion kan være forskellig fra depleteringsrekombinationsstrømmen (n ~ 2). J-V-T-egenskaberne for heterojunktions-solceller med MoO_x, WO_x og VO_x som HTL'er blev analyseret. Det konstateres, at strømtætheden har karakteristikken for tunnelstrøm i lavspændingsområdet, hvis faktor A1 er uafhængig af temperaturen, mens den gennemsnitlige værdi af idealfaktor n er stor uden nogen bestemt værdi. I højspændingsområdet er strømtætheden i overensstemmelse med den ideelle diodelov. Baseret på junctionskarakteristikken og *J*-*V*-*T*-karakteristika for MoO_x/silicium heterojunction blev *J*-*V*-*T*-kurven for MoO_x/Si heterojunction solceller simuleret ved hjælp af elektronens termioniske strømtæthed J_{Te} og tunneldrivstrømstætheden J_{Tu}, der repræsenterer den termioniske emission og den termisk assisterede tunnelproces af henholdsvis elektroner og den defekte understøttede tunnelproces af huller. Simuleringsresultaterne viste, at den effektive barrierehøjde φ_{Bn}=0.98eV ved grænsefladen mellem MoO_x/silicium heterojunction præsenterede både stærk inversionsregion, der blev dannet på overfladen af krystallinsk silicium, og den høje inversionsbarriere, der indikerer højt potentiale V_{OC}. Barrierehøjden opnået ved montering var dybest set i overensstemmelse med det indbyggede potentiale for MoOx/Si heterostruktur bestemt ved *C*-*V*-måling ($\varphi_{Bn} \approx V_D + (E_c - E_F)$). Ifølge simuleringsresultaterne mener vi, at MoO_x/Si heterostruktur er et Schottky-lignende kryds med høj barriere eller stærk inversionskarakteristik. Den nedre barrierehøjde på WO_x og VO_x enheder antydede, at overfladen af krystallinsk silicium ikke var stærk inversion, hvilket kan være relateret til Fermi-niveau-fastgørelse forårsaget af den høje tæthed af tilstande med grænsefladedefekter.

Nøgleord: Overgangsmetaloxidfilm, materialekarakterisering, heterojunction solceller, transportmekanisme.

ACKNOLEGEMENT

This thesis is submitted for assessment to the Faculty of Engineering and Science, Aalborg University in fulfillment of the PhD degree. This thesis is based on scientific paper listed in Section 1.3. The work was performed at the Section of Chemistry and Bioscience at Aalborg University and Sino-Danish College at University of Chinese Academy of Sciences.

I would like to thank my supervisor, Associate Professor Donghong Yu, for all the guidance, help, support, and encouragement. I was impressed by his profound knowledge, solid theoretical foundation, keen insight and rigorous academic research. Thank you for all the meeting and the discussions, which have helped me to become a researcher. Professor Yu is humble and approachable, and has given me lots of care and inspiration in daily life, which would be useful to all my life. On the occasion of the completion of my Ph.D. thesis, I hope that I can extend my respect and sincere thanks to professor Yu!

I would also like to give great thanks to my supervisor, Professor Fengzhen Liu from University of Chinese Academy of Sciences, for her great guidance on my whole PhD project during my entire PhD study. Her rigorous academic attitude, profound professional knowledge, meticulous research style, and amiable and modest way of treating people are worth learning and imitating all my life. Thank for her selfless teaching and teaching in the process of theoretical study and scientific research experiment.

Thanks to all the teachers, students, and staffs in the Department of Chemistry and Bioscience at the University of Aalborg. I would like to say thank you to Annemarie Davidsen who gave me a lot help during the Ph.D. time, and I would also like to say thank you to Anna-Sophie, Ang Qiao, Theany，Chengwei Gao，Zhencai Li，Jiajia Yan，Linling Tan，Rasmus, Xianzheng Ma, Xiangting Ren and others who I met in my Ph.D. career at AAU. Thank you for your love and support during my long career, and sincerely wish you good health and good luck!

LIST OF PUBLICATIONS

PUBLICATIONS IN PEER REVIEWED JOURNALS

1. **Fengchao Li**, Yurong Zhou*, Ying Yang, Gangqiang Dong, Yuqin Zhou， Fengzhen Liu*, **Donghong Yu**, *et al.* Silicon heterojunction solar cells with MoO_x hole selective layer by hot wire oxidation-sublimation deposition. **Solar RRL**, 2020, 1900514.

2. **Fengchao Li,** Zongheng Sun, Yurong Zhou*, Qi Wang, Qunfang Zhang, Gangqiang Dong, Fengzhen Liu**, Zhenjun Fan, Zhenghao Liu, Zhengxiong Cai,Yuqin Zhou, **Donghong Yu**. Lithography-free and dopant-free back-contact silicon heterojunction solar cells with solution-processed TiO_2 as the efficient electron selective layer. **Solar Energy Materials and Solar Cells**, 2019, 203: 110196.

ORAL AND POSTER PRESENTASTIONS AT CONFERENCES

1. **Fengchao Li**, Yurong Zhou, Fengzhen Liu, Rongzong Shen, Ming Liu. Molybdenum oxide fabricated by hot-wire oxidation sublimation method is used as hole transport layer of silicon heterojunction solar cells, China Renewable Energy Conference 2018 (Beijing), August 2018.

2. **Fengchao Li**, Yurong Zhou*, Gangqiang Dong, Rongzong, Shen, Yanbin Shi, Fengzhen Liu*. Transition metal oxides hole-selective layers by hot-wire oxidation-sublimation deposition for novel Si heterojunction solar cells application. PVSEC-29, November 4-8, 2019 .

PATENT

1. **Fengchao Li,** Yurong Zhou, Fengzhen Liu, Rongzong Shen, Ming Liu, a fabrication method of molybdenum oxide film and silicon heterojunction solar cell using molybdenum oxide film as hole transport layer, patent application No.: 2018113132632.(Chinese patent, substantive examination)

TABLE OF CONTENTS

CHAPTER 1. INTRODUCTION... 1

1.1 THE DEVELOPMENT OF SOLAR CELL 2
1.1.1 Photovoltaic effect.. 2
1.1.2 Classification of solar cells.. 2
1.13 Development of crystalline silicon solar cells.. 4
1.1.4 The novel dopant-free silicon heterojunction solar cells 8
1.2 THE SIGNIFICANCE AND RESEARCH FOCUS OF THIS PHD THESIS 14
1.3 THE CONTENT OF THIS PHD THESIS 15

CHAPTER 2. EXPERIMENTAL AND METHODS 17

2.1 MATERIAL FABRICATION 17
2.1.1 Cleaning and preparation of substrates.. 17
2.1.2 Fabrication of MoO_x, WO_x, and VO_x films.. 17
2.2 CHARACTERIZATION OF MATERIAL PROPERTIES 18
2.3 FABRICATION OF SOLAR CELLS 19
2.3.2 Preparation of amorphous silicon passivation layer 19
2.3.3 Preparation of transparent conductive film 20
2.3.4 Preparation of electrodes... 20
2.4 CHARACTERIZATION METHODS FOR SOLAR CELLS 20
2.4.1 The J-V characterization for solar cells.. 20
2.4.4 Dark I-V measurement on solar cells 24

CHAPTER 3. FABRICATION AND CHARACTERIZATION OF MOO_X, WO_X, AND VO_X THIN FILMS... 27

3.1 OPTIMIZATION OF FABRICATING PARAMETERS OF TMO THIN FILMS 28
3.1.1 The effect of hot wire temperature in the fabrication of MoO_x, WO_x, and VO_x thin films 28
3.1.2 Effect of oxygen pressure on the deposition of MoO_x and WO_x............. 30
3.2 MATERIAL FEATURES OF FILMS OF MOO_X, WO_X, AND VO_X 32
3.2.1 Morphology of MoO_x, WO_x and VO_x thin films....................................... 32
3.2.2 Structural characteristics of MoO_x, WO_x, and VO_x 34
3.2.3 The electronic structure of MoO_x， WO_x, and VO_x 36
3.2.4 Optical properties of MoO_x, WO_x, and VO_x.. 38
3.2.5 Electrical characteristics of MoO_x and WO_x.. 39
3.3 EFFECT OF ANNEALING ON OPTICAL AND STRUCTURAL PROPERTIES OF TMO THIN FILMS ... 42
3.4 SUMMARY 45

CHAPTER 4. OPTIMIZATION OF HENTEROJUNCTION SOLAR CELL WITH MOO_X, WO_X, AND VO_X 47

4.1 OPTIMIZATION OF NOVEL SILICON HETEROJUNCTION SOLAR CELLS WITH MoO_x AS HTL..... 47
4.2 THE PERFORMANCE COMPARISON AMONG THE SHJ SOLAR CELLS WITH MoO_x, WO_x, AND VO_x AS HTLS........ 58
4.3 APPLICATION OF MoO_x AND WO_x IN LITHOGRAPHY-FREE AND DOPANT-FREE BACK CONTACT HETEROJUNCTION CELLS........ 62
4.4 CONCLUSION 64

CHAPTER 5. TRANSPORT MECHANISM OF SILICON HETEROJUNCTION SOLAR CELLS 67

5.1 HIGH FREQUENCY CAPACITANCE-VOLTAGE (*C-V*) CHARACTERISTICS OF SHJ SOLAR CELLS ... 67
5.2 DARK *J-V* CHARACTERISTICS OF SHJ SOLAR CELLS AT ROOM TEMPERATURE 70
5.4 SUMMARY........ 83

CHAPTER 6. SUMMARY AND PROSPECT 85

6.1 SUMMARY........ 85
6.2 PROBLEMS AND FUTURE PROSPECTS........ 87

BIBLIOGRAPHY 89

APPENDICES 101

Appendix A. Paper Ⅰ

Appendix B. Paper Ⅱ

Chapter 1. Introduction

Energy has been driving the historical progress on civilization of mankind, of which level has been marked by the types of energy and the way of utilization. From the perspective of cosmology, solar radiation is the sole passive energy resource, whose persistent and sustainable lighting conditions creates the indispensable external environment for lives on earth. In the early stage of organism, plants and microorganisms firstly took advantages of photosynthesis , and then continuously evolved higher vegetation and animals. The remains of early plants and animals were buried underground during tens of thousands of years as geological deposits for storing solar energy in the form of fossil energy on earth. Our ancestors learned "drilling wood for fire" signifing that humans could actively use energy according to their own needs, initiating the evolutionary development of human civilization. In the tenth century BC, the ancient Egyptians and the Babylonians learned to use oil, while Chinese began to use coal, as fuel, indicating that mankind had begun to recognize and use fossil energy. Human beings realized the transformation from fossil energy to mechanical energy until the 1760s, at the beginning of the first industrial revolution. Since entering the "electric age" in the 1960s, human beings have transformed fossil energy into electrical one, furthermore promoting the development of human civilization[1]. However, such rapid development has led to the massive consumption of traditional fossil energy and the continuous deterioration of the living environment. These current situations undoubtedly put forward new requirements and refreshed standards for human energy utilization technologies and energy types. Renewable and sustainable energy such as solar energy and high technology energy such as nuclear energy have become the important focus in not only fundamental research but also industrial productions.

Although nuclear energy has the advantages of no greenhouse gas emission, abundant raw material reserves and convenient transportation, it also needs to solve the uncontrollable risks caused by the safe disposal of nuclear waste, the special site selection of power plants and the intense nuclear reaction. The Chernobyl incident in Ukraine and the Fukushima nuclear leak in Japan have all put forward higher requirements for the high standard design and construction, safe operation and crisis management of nuclear power plants. Compared with nuclear energy, the utilizing of solar energy shows much more advantages than that: (1) abundant reserves; (2) efficient and clean; (3) no polluted emissions; (4) no need for mining, storage and transportation; (5) no safety risk. At present, the utilization forms of solar energy are mainly solar-thermal utilization, photochemical utilization, and photoelectric utilization. Among them, the photoelectric utilization using solar cells as photoelectric conversion devices shows its huge potential[2].

1.1 The development of solar cell

1.1.1 Photovoltaic effect

The essence of solar cells converting solar energy into electrical one is the photovoltaic effect. Photovoltaic effect is that when a specific substance or device is illuminated, its internal charge state and distribution will be altered to produce electromotive force and current[3]. As early as 1839, the photoelectric effect was accidentally discovered when two metal platinum sheets were immersed in solution by the French scientist AE Becquerel[4]. When it was exposed to light, an extra electric potential was generated at both ends of the electrode, and the phenomenon was named photovoltaic effect, followed by the report of the photovoltaic effect of selenium (Se) by W. G. Adams and R. E. Day in 1877. The very first the solid-state photovoltaic effect was pronounced by C. Fritts in 1883, with a current flow generated from a device of Au/Se/Metal was under solar irradiation. For exploring its working principle, Fritts farsightedly put forward his idea: "You can store this current, or you can transfer it to where you want ...", suggesting the application of photovoltaic technology. In 1904, Hallwachs discovered that copper combined with cuprous oxide (Cu/Cu2O) had certain photosensitive properties. In 1930s, Schottky also discovered the photovoltaic effect that could convert light into voltage on solid phase copper oxide (Cu2O). All these researches had inspired scientists to devote themselves on converting solar energy into electrical one, therefore developing solar cells to meet the continuous pursuit of human energy in the future[5].

1.1.2 Classification of solar cells

The booming era of solar cells didn't really come until the second half of the 20th century. In 1954, researchers from Bell Laboratory in the United States discovered the photovoltaic phenomenon from single crystal silicon p-n junctions and reported a single crystal silicon solar cell with a photoelectric conversion efficiency (PCE) of 4.5%, which officially launched the era of crystalline silicon solar cells[6]. Junior solar cells were mainly used in aerospace fields such as satellites. In the following half a century, burst out about the development of miscellaneous science and technology for solar cells, and their power conversion efficiency was also continuously updated[7]. The National Renewable Energy Laboratory (NREL) in USA began to trace the year-by-year progress chart of record PCEs of various solar cells since 1975, as shown in Figure 1.1[8]. From the perspective of the absorption layer materials used in solar cells, they can be divided into: silicon-based solar cells, compound solar cells, organic solar cells, and perovskite solar cells, etc. Silicon-based solar cells can be further sub-divided into: single crystalline silicon solar cells, polycrystalline silicon solar cells, and amorphous silicon solar cells. From the battery

structure points of view, they can be divided into: single-junction solar cells and multi-junction solar cells.

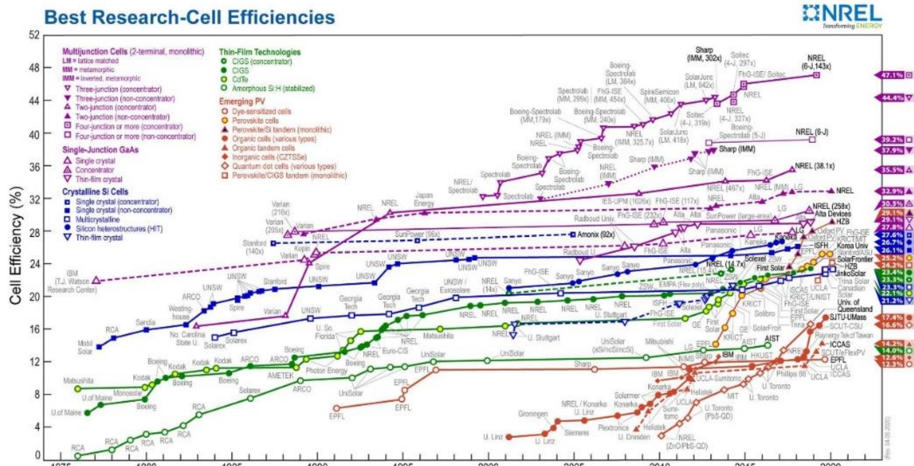

Figure 1.1 The record PCEs of various solar cells published by NERL[8].

Based on the concept of "the third generation" solar cell proposed by Martin Green of the University of New South Wales, Japanese scholar Yasi Kawasaki proposed the division standard of solar cell technology, which is commonly recognized by the solar cell community[9, 10], as follows:

The first generation of solar cell technology is represented by crystalline silicon, which has been fabricated by relatively mature technology, whose market share accounts for more than 90% of the current commercialized solar cell technology. The characteristics of this type of solar cell are: (1) relatively mature fabrication technology; (2) abundant silicon raw material in the earth's crust; (3) stable operation of the device, which has been practically applied to satellites and photovoltaic power plant and other aspects; (4) high PCEs; (5) complex preparation process and large energy consumption; (6) The high cost of silicon wafers and the long recycling period.

The second generation of solar cells are from thin-film technolgoy, mainly represented by GaAs, a-Si, CIGS, CdTe, and μ c-Si. These cells use high absorption coefficient materials, which only need a few microns thick to absorb full wavelength sunlight, greatly reducing the consumption of raw materials. However, there are some special elements included in , for example, Cd as a toxic element, being inevitably t harmful in both their fabrication and uses. Te, In, and Ga are rare elements in the earth's crust, restricting the commercialization of these types of solar cells to large

extents. As for the amorphous silicon solar cell, the development had been limited due to their inevitable light attenuation effect.

The third generation is the new concept solar cells, such as multi junction (band gap gradual change) solar cell, organic/polymer solar cell, perovskite solar cell, quantum dot solar cell, intermediate band (impurity band) solar cell, and hot carrier solar cell, including their corresponding tandem solar cells. Many of those are, at present, still in the early or infant stage of laboratory research . On the other hand, for certain types of solar cells, there are still gaps between the actual conversion efficiency and their theoretical expectance. Among of them, perovskite solar cell has gained more attention because of its low cost and simple preparation conditions, with its highest PCE of 25.2% in Figure 1.1). In addition, with the continuous improvement of the device fabrication technology, in the future, the tandem solar cells based on perovskite cells or polymer solar cell combined with crystalline silicon solar cell, could be the right direction of these third generation solar cells in the future. For the former, a record PCE of 29.1% had been reached by HZB research center, Germany (Figure 1.1). However, these two types solar cells are still facing the challenges from light attenuation and water decomposition, which need to be solved.

1.13 Development of crystalline silicon solar cells

Being originated in the 1960s, but boosted in the late 1980s, high-efficiency of crystalline silicon solar cells have been rapidly and successfully developed. For instance, the fabrication processes of crystalline silicon solar cell have been very mature, with its steadily increased PCE up to 26.7%[11, 12], which is gradually approaching to its theoretical limitation of 31% for single junction solar cells[13].

In the early stage of this type of solar cell's fabrication[14], different techniques had been adapted as following: (1) growth junction[15]: the part with PN junction structure was cut from the recrystallized material to fabricating solar cells; (2) implanted junction[16]: helium ion bombards the surface of silicon material to form implanted junction; (3) diffusion junction[6]: PN junction is formed by lithium or boron diffusion technology. On the basis of these three technologies, different design and manufacture of crystalline silicon solar cells were carried out, with its PCE of 10%.

With the development of semiconductor technology, a certain light trapping structure[17, 18], which is fabricated by micro-nano fabrication technology on the surface of silicon wafer, can greatly reduce the reflection loss. And the application of antireflection layer on the surface of solar cell can improve the short-circuit current density of solar cell (J_{sc}) and therefore to improve the PCE of solar cells[19]. In addition, the application of surface passivation technology[20], which was

implemented in the electrode area and the contact interface, can effectively passivate the dangling bonds, for both reducing the recombination of carriers in the region and improving significantly the open circuit voltage (V_{oc}) and fill factor (FF) of those solar cells. A number of advanced technologies including film fabrication, doping technology, photolithography, and screen printing have been applied in solar cell fabrication, leading the continuously inproved PCEs[21-24]. Several design structure of typical high efficiency solar cells are demonstrated as follows:

(1) Aluminum back surface field cell (Al-BSF solar cell)[25-27]: A p-type silicon wafers are used as the absorption layer, forming PN junctions with an n+ diffusion layer through a phosphorus doping process, and using SiNx as the anti-reactive passivation layer in the visible range for improving the anti-reflection absorption effect of the solar cells. Especially the back surface aluminum and silicon form a p+ heavily doped region during the sintering - recrystallization alloy, which can reduce the rates of carrier recombination at the solar cell back surface, thereby improving the Voc, Jsc, and the overall performance of solar cells. The manufacturing process of the solar cell with this structure (see Figure 1.2) was mainly divided into five steps: texture of the silicon wafer, phosphorus diffusion on the front surface, SiNx anti-reflection layer, sintering and preparation of the front and rear electrodes. These manufacturing process are in general regarded as low cost and easy realization with a PCE up to 20% obtained[28].

(2) Passivated emitter and rear solar cell (PERC)[29-31]: Based on the Al BSF solar cell, in order to further improve the passivation effect of the emitter and the back of the solar cells, n+ + heavy doping layer was fabricated in the n+ diffusion region to reduce Auger recombination and parasitic absorption, and to improve the carrier transport performance. Prior to the aluminum back field layer on the back of the battery, the aluminum oxide (Al_2O_3) passivation layer is fabricated, which not only passivates the back surface, but also ensures the good transport of carriers. In the structural design of the solar cell (manufacturing process and structure, see Figure 1.2), the application of passivation technology makes Voc of the solar cell further improved, with PCEs of 23% - 24% approached[32].

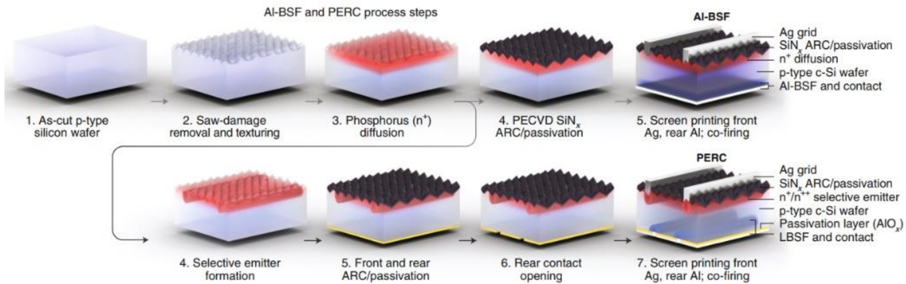

Figure 1.2 Fabrication process of the aluminum back field solar cells and the passivated emitter and rear solar cells[33].

(3) Interdigitated back contact solar cell (IBC solar cell)[34]: the structure design of the cell is shown in Figure 1.3. N-type silicon wafer is used as the absorption layer of the device, followed by n+ front surface field, SiO_2 passivation layer, and antireflection layer on the front surface for better absorbing light. The n-type and p-type doping layers, the porous SiO_2 passivation layer, and the metal grid lines are then fabricated on the back side of the solar cell. The advantage of such designed back contact solar cell is that the front surface of the electrode can keep from blocking sunlight and absorb visible light to the greatest extent. The interdigitated back contact can effectively limit the recombination loss. High-efficiency passivation and the use of back metal electrode can further reduce the series resistance of the device. However, the finger-like interdigitated structure on the back demands micro-nano processing technology such as photolithography, which increases the manufacturing cost of this kind of solar cell to large extent.

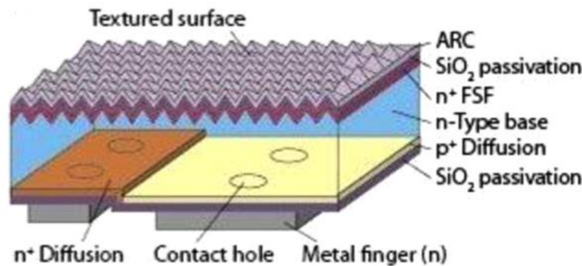

Figure 1.3 Schematic of the interdigitated back contact（IBC） solar cell[35].

(4) Silicon heterojunction solar cell (SHJ solar Cell)[36, 37]: with the development of high-quality non-destructive amorphous silicon (a-Si) technology, the passivation effect of a-Si on the surface defects of Si wafer has been significantly improved. Sanyo company[38] (Japan) designed a solar cell structure, as shown in Figure 1.4,

where PECVD technology was used to passivate the front and rear surfaces of silicon wafer with hydrogenated amorphous silicon a-Si:H, and then n-type and p-type a-Si were fabricated on the front and rear surfaces of the solar cell respectively, followed by the transparent conductive oxide (TCO) and the front and back metal electrodes. Due to the highly efficient passivation of a-Si:H and the transport of carriers by doped amorphous silicon film and TCO film, the solar cells obtained 745 mV V_{OC} and 81.5% FF. Then, applying metal grid electrode structure on the metal electrode on the back surface resulted SHJ solar cell with double-sided light receiving[39], as shown in Figure 1.4.

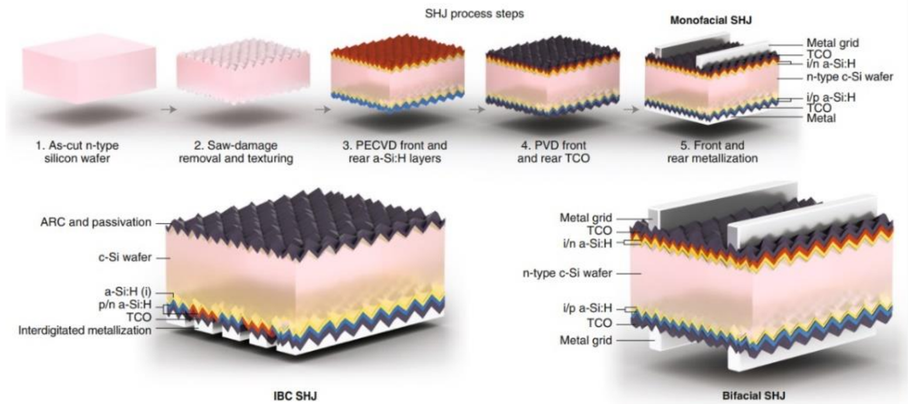

Figure 1.4 Fabrication process of The silicon heterojunction solar cells and the schematic of IBC-SHJ solar cells and bifacal SHJ solar cell[33].

(5) Silicon heterojunction solar cell with interdigitated back contacts, (IBC-SHJ solar cell) : Kaneka company in Japan reported a new type of solar cell in 2017, which combines the amorphous silicon passivation technology of silicon heterojunction solar cell with the interdigitated electrode structure of back-light surface of back contact solar cell, with its performance of V_{OC} of 738 mV, J_{SC} of 42.65 mA / cm^2, FF of 84.9%, and PCE of 26.7%. That has been the highest efficiency of single-junction crystalline silicon solar cellever[11, 12].

The conceptual schematic diagram of solar cell shown in Figure 1.5 can be obtained by analyzing and studying the structure of a high efficiency solar cell. High-performance solar cells should have the following characteristics: (1) high quality interface passivation layer, which can effectively reduce the recombination of carriers at the interface and greatly improving the V_{OC} of solar cells; (2)High-quality carrier selection transport layer, which can select and separate different carriers, allow one of the carriers to pass through and effectively block the other, realizing one-way transport of carriers, quickly exporting the separated carriers, and improving the

capability of collecting carriers of solar cells; (3) high standard silicon absorption layer under the premise of effective absorption of sunlight, in which recombination of carriers in silicon wafer could be minimized.

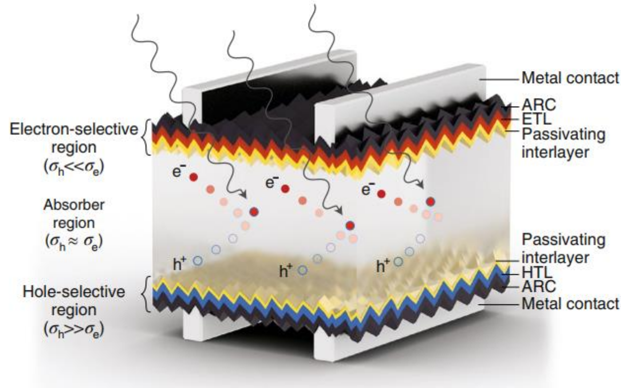

Figure1.5 The schematic of the conceptual solar cel[33]l.

Based on the analysis and summary of the development of crystalline silicon solar cells, researchers have focused on three aspects for: looking for high-quality passivation layer, developing high-quality carrier selection transport layer material, and exploring new silicon absorption layer, and made some progress.

1.1.4 The novel dopant-free silicon heterojunction solar cells

In order to develop high-quality carrier selective transport layer materials, world-wide studies have found that: molybdenum oxide (MoO_x)[40-43], tungsten oxide (WO_x)[44-46], vanadium oxide (VO_x)[47-49], nickel oxide (NiO_x)[50, 51], poly(3,4-ethylenedioxythiophene) and poly(styrene sulfonate) (PEDOT: PSS)[52, 53], graphene[54], carbon nanotubes[55], and other thin film materials with high work function can contact with crystalline silicon, realizing fast transport of holes but hinder the that of electrons. At the same time, materials with low work functions, such as zinc oxide (ZnO)[56-58], magnesium oxide (MgO)[59], lithium fluoride (LiF_x)[43, 51, 60], and titanium oxide (TiO_x)[60-62], are good electron selective transport materials. Among them, this thesis focuses on new silicon heterojunction solar cells that use MoO_x, WO_x, and VO_x as hole-selective transport layers (HTLs).

MoO_x as a hole-selective transport layer of crystalline silicon cells is concerned because its work function of up to 6.9 eV can cause a large crystalline silicon surface energy band-bending to realize the selective transport of holes, while keeping its nd bandgap of 3.0- 3.3 eV for greater light transmittance in the visible-light region[63].

In addition, the fabrication process of molybdenum oxide does not require the use of borane and other toxic/dangerous gases, which greatly reduces the production cost of solar cells.

In 2014, Corsin Battaglia et al.[40] reported MoO_x thin film by thermal evaporation and analyzed them using XRD, Raman and XPS methods, replacing the p-type a-Si with 15nm MoO_x for a direct contact the silicon wafer, as shown in Figure 1.6 (a). Such solar cells obtained V_{OC} of 580 mV and J_{SC} of 37.8 mA/cm^2, but fill factor of only 65%, therefore a final PCE 14.3%. Considering interface passivation, i a-Si was subsequently used as the passivation layer, and the thickness of MoO_x was reduced to obtain the structure shown in Figure 1.6 (b). The V_{OC} of the solar cell was increased to 711 mV, and the J_{SC} was 39.4 mA/cm^2, FF increased slightly to 67.2%, and its PCE rose to 18.8%[63].

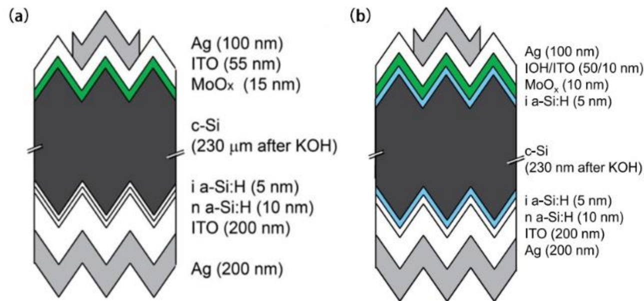

Figure 1.6 a) The schematic of a new MoO_x heterojunction solar cell without passivation layer[40]. (b) The schematic of MoO_x heterojunction solar cells with i a-Si as passivation layer[63].

Jonas geissbuhler *et al.*[42] studied the influence of conventional annealing process on MoO_x and hydrogenized indium tin oxide (IO:H/ITO). The structure of the solar cell was Cu/IO:H/ITO (65nm)/MoO_x (7 nm)/i a-Si:H/n-type FZ Silicon (230μm random pyramid surface texture)/i a-Si:H/n a-Si:H/ITO/Ag. The solar cell obtained its V_{OC} of 725.4 mV, J_{SC} of 38.60 mA/cm^2, FF of 80.36%,and PCE up to 22.50%.

In 2016, James bullock *et al[43].* developed a novel dopant-free asymmetric heterojunction solar cell (DASH solar cell) with MoO_x and LiF_x as HTLs and ETLs respectively. They proposed the concept of DASH solar cell with the structure shown in Figure 1.7. The solar cell performance of V_{OC} of 716 mV, J_{SC} of 37.07 mA/cm^2, FF of 73.15% and PCE of 19.42% was obtained. The concept of dash cell indicates that the replacement of p-type and n-type a-Si with materials with high and low work functions as carrier selective transport layers has become a new method for new

silicon heterojunction solar cells, and crystalline silicon solar cells have changed from traditional PN junction to interfacial junction with carrier selective transport functions.

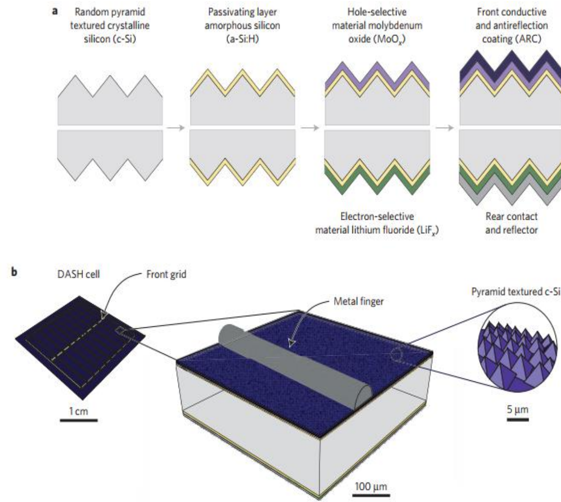

Figure1.7（a）The schematic of the dopant-free asymmetric heterocontacts solar cell.（b）3D representation showing the metal grid and texture of the front (sunward) side of the DASH cell[43].

Marco Della Noce et al.[64] studied the performance of MoO_x as HTLs in p-type SHJ solar cells, whose structure are shown in Figure 1.8 (a). P type textured FZ wafer was fabricated as absorption layer, MoO_x as HTLs and n µ c-SiO_x as ETLs respectively. PCE of 18.1% was obtained, with its *I-V* curve shown in Figure 1.8 (b).

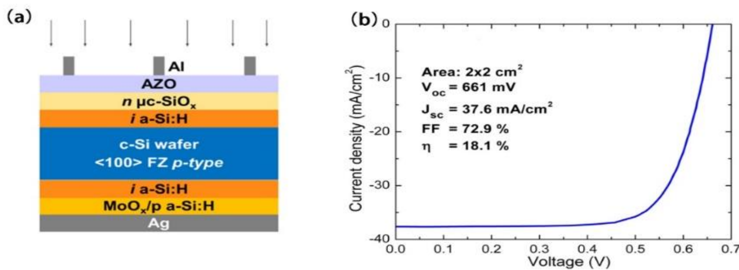

Figure1.8（a）The schematic of the p-type SHJ solar cell.（b）J-V characteristic of textured p-type SHJ solar cell with MoO_x[64].

Jianhua Shi *et al*[65]. fabricated a new SHJ solar cell structure for double-sided light receiving with MoO_x/p a-Si/i a-Si structure as the hole selective transport contact, as shown in Figure 1.9. With an optimized thickness of 3 nm for MoO_x layer, the best performance with V_{OC} of 730 mV, J_{SC} of 37.5 mA/cm^2, FF of 78.1%, and PCE of 21.8% was achievied as the highest.

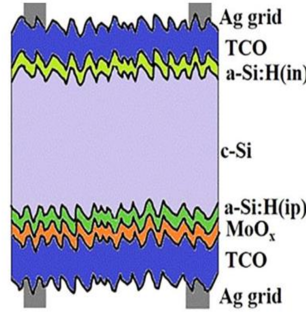

Figure 1.9 The schematics of the MoO_x based bifacal SHJ solar cell[65].

In 2020, Julie Dreon and *et al.*[41] conducted a systematic study on MoO_x, and further optimized the thickness of MoO_x and i a-Si:H. When the thickness of MoO_x and i a-Si:H was 4 nm and 6 nm respectively, the solar cell possessed a PCE of 23.5% as shown in Figure 1.10, being the highest efficiency of a novel silicon heterojunction solar cell with MoO_x as the hole transport layer.

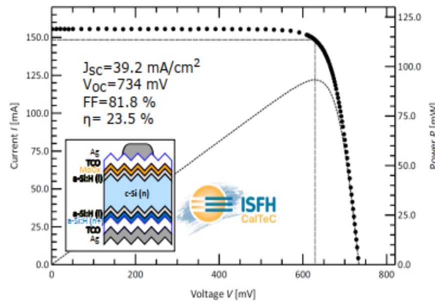

Figure 1.10 The J-V curves of the best solar cell with MoO_x as HTLs[41].

With the continuous research on solar cells using MoO_x as HTLs, the nature of the contact interface between MoO_x and other functional layers has gradually caught attention. Takefumi Kamioka *et al.*[66] found that when MoO_x was in contact with ITO, the interface work function of them would decrease by 0.41 eV compared to that

of MoO_x itself. The post-annealing process in the solar cell manufacturing process could also cause a significant drop in the work function of MoO_x. Davide Sacchetto and others[67] also paid attention to the phenomenon that the work function of MoO_x declined during the preparation of the ITO/MoO_x/i a-Si:H multilayer structure. Ming Gao *et al.*[68] found that SiO_x (Mo) interface layer was formed when MoO_x was in contact with n-type silicon wafer, being suppported by calculation using density functional theory (DFT). It is believed that there are two localized states in the SiO_x (Mo) interface layer which can realize the defect-assisted tunneling of the carrier, and there are three extended states at the same time that the carrier can tunnel through. Hisham Nasser studied the existence of a certain correlation between the doping concentration of MoO_x and the silicon wafer through a program of Silvaco TCAD for simulation. The structure of heterojunction solar cell is cathode contact/n + c-Si/n-type c-Si/MoO_x/anode contact. The simulation results show that, as the silicon wafer doping concentration increases from 1×10^{15} cm^{-3} to 1×10^{16} cm-3, the PCE drops from 11.16% to 6%.

Besides the thermal evaporation method for fabricating molybdenum oxide in the above-introduced research, other methods had been also explored. Martin Bivour *et al.*[69] used plasma enhanced atomic layer deposition technology (PEALD) to fabricate MoO_x thin films, and studied the effect of deposition conditions on the performance of these thin films; Johannes Ziegler *et al.*[70] fabricated MoO_x by PEALD technology as HTLs to manufactured solar cells, and believed that the device performance may be restricted by the low work function of MoO_x prepared by ALD technology.

In addition, some researchers[71-74] also used sputtering technology to fabricated MoO_x films, and studied the influence of various parameters on the performance of MoO_x materials during the sputtering process by means of XRD, AFM, contact potential, Raman, and SEM. However, the *J-V* curve of the MoO_x solar cell manufactured by the sputtering method also showed the S-type, which is believed to be caused by the trap state from the surface damage of the silicon wafer during the sputtering process. Electron beam deposition is another method for preparing MoO_x, R. Sivakumar *et al.*[75] conducted a more systematic study on the MoO_x film deposited by electron beam, focusing on the influence of substrate temperature on the structure, morphology and optical properties of MoO_x film. There are few reports on heterojunction solar cells with MoO_x thin films fabrcated by electron beam deposition technology. The solution method[76] was also attractive because of its low cost. Using HyMoO_x as the precursor solution, a MoO_x film was obtained by spin-coating the surface of the silicon wafer and then annealing at 150 °C[77]. At present, the PCE of silicon solar cells with MoO_x as HTLs fabricated by the solution method is up to 8.22% (V_{OC}: 463.6 mV, J_{SC}: 31.16 mA/cm^2, FF: 56.87%)[78]. The reason for the low

performance of the device may be that the precursor will form an SiO_x layer at the interface with the silicon wafer during the annealing process.

While studying MoO_x as HTLs, studies on WO_x and VO_x as HTLs is also progressed. Martin Bivour *et al.*[46] used thermal evaporation technology to fabricated WO_x thin film materials, and the PCE of nearly 18% was achieved. Mathias Mews[44] believed that the increase in the oxygen hole concentration in WO_x prepared by thermal evaporation technology caused the Fermi level of WO_x to rise, the work function to decrease, and the band-bending of the crystalline silicon surface to decrease, which directly affected the V_{OC} and FF of the solar cell. Subsequently, they used reactive sputtering to prepare WO_x thin films, and studied the influence of O_2 and Ar ratio and other process parameters on the photoelectric performance and device performance of WO_x, gaining an optimized PCE of 16.6% [79]. Chang-Yeh Lee [80]fabrcated WO_x thin film materials by ALD technology, and studied the effect of annealing temperature on the performance of WO_x materials. By studying the passivation effect of WO_x on silicon wafers, it was estimated that the open circuit voltage of solar cell with WO_x as HTLs might reach 730 mV. Kaifu Qiu and others[45] used WO_x and ZnS as HTLs and ETLs, respectively, to manufacture p-type silicon doped heterojunction solar cells, whose structure was Ag/ITO/ZnS/p Si/WO_x/Ag, and that solar cell gained a V_{OC} of 525 mV, J_{SC} of 33.75 mA/cm^2, FF of 61.37%, and final PCE of 10.94%. Osbel Almora[47] used V_2O_5 as HTLs to manufacture a solar cell with a structure of Ag/ITO/V_2O_5/n-type c-Si/(i/n)a-SiC_x:H/a-SiC/Ti/Al, which could obtain a PCE of 15.6 %, and the performance of the device was analyzed using *C-V* and impedance spectroscopy.

With the continuous improvement of the power conversion efficiency of novel heterojunction solar cells, the transport mechanism of carriers within the devices turned to be very important and fundamental to be the bridge the relationship betweem device structure and photovoltaic performance. The structural diagram of the solar cell with the structure of Ag/MoO_x/Si/Al under thermal equilibrium and illumination shows that MoO_x causes a barrier at the interface, which can hinder the transport of electrons[81]. Under lightening, the potential barrier can suppress the recombination of electrons and holes, and lead holes out through the band gap state. The research from Dongyun Chen *et al.*[82] confirmed that a non-crystalline a-SiO_x (Mo) buffer layer was formed at the contact interface between MoO_x and n-type silicon wafer during the thermal evaporation of MoO_x. The analysis using DFT theory found that: due to the hybridization of the 4d orbital electrons of Mo and the 2p orbital electrons of O, there are 5 local states in the band gap of the buffer layer, which showed that Mo element was doped in SiO_x. The deep defect level introduced by the doping has become a channel for assisting the tunneling of holes, so the transport mechanism in the photovoltaic device with MoO_x/SiO_x(Mo)/n-Si was explained as defect-levels assists tunneling. Further research by Ming Gao *et al.*[68] illustrated that the a-

SiO_x(Mo) band gap possessed 2 half-filled levels (localized states) and 3 unoccupied levels (extended states), respectively, being responsible for the hole defect-state assisted tunneling and direct tunneling. It is believed that the transport mechanism of MoO_x/n-Si solar cells should be described by a more reasonable tunnel-recombination model. Sentaurus software was used to simulate the structure of MoO_x/i a-Si:H/c-Si,by Christoph Messmer *et al.*[83] emonstrating that MoO_x with high work function could induce c-Si to form an induced junction at the contact interface. The buffer layer and the metal oxide together completed the transport of carriers at the interface. Since the conduction band of the metal oxide was lower than the valence band of the buffer layer, the carrier transport was achieved by band-band tunneling. Bulk traps near the valence band of the buffer layer helped carriers transport through trap-assisted tunneling. It was also pointed out that the transport mechanism of carriers dominated by the contact interface of high work function oxides represented by MoO_x was trap-assisted tunneling in the band gap. Dark current density–voltage–temperature of the heterojunction solar cell with MoO_x as HTLs was studied by García-Hernansanz R in Spain, whose transport mechanism was mainly controlled by the barrier formed by MoO_x and c-Si conduction band[84]. Above all, the transport mechanism of these devices has also been the focus of debate.

From the above literatures investigation, we can see that the current fabrication methods of MoO_x, WO_x, and VO_x thin film materials include thermal evaporation, sputtering, atomic layer deposition, electron beam deposition, and solution method. Among them, thermal evaporation is the most commonly used method for preparing MoO_x thin films. However, such a method is often accompanied by certain shortcomings such as high-purity demands on MoO_x powder as evaporation material, non-efficient utilization of evaporation materials and easy-crust, which restricted its commercial promotion to large extent. In addition, there are exsisting controversies in understanding the transport mechanism of this type of devices, which needs further investigation.

1.2 The significance and research focus of this PhD thesis

Based on the above-summrized literatures on solar cells, we know that research on the novel dopant-free silicon heterojunction solar cells with representative MoO_x has been of great importance in the field with great advantages of (1) wider band gaps of 3.0-3.3 eV that can not only ensure high transmittance of visible light, but also has small parasitic absorption itself; (2) high work functions in contact with crystalline silicon that can form an effective band bending, making an inversion layer near the surface of the silicon wafer to form an induced PN junction and realizng unidirectional selective transport of carriers; (3) good alternatives to the heavy doping process in traditional heterojunction solar cells, which greatly reduces the use of borane and phosphane gases; (4) simple material fabriction method and low equipment cost.

However, there are still some challenges: firstly, the current fabrication process is difficult for either accurate control or commercialization for large-scale stable production, e.g.,the material performance and their work functions; secondly, there still exist the incompatibility between the current solar cell structural design and the company's production process; thirdly, the understanding of the carrier transport mechanism of this type of device, which needs to be further explored so as to further develop the application potential of this type of battery.

Facing the current opportunities and challenges of this type of solar cells, we propose a new method of "hot-wire oxidation sublimation deposition" to fabricate MoO_x, WO_x, and VO_x for using them as a hole selective transport layer (instead of n-type crystalline silicon cell emitter) to develop new silicon heterojunction solar cells, and furthermore investigate their charge carrier transport properties for revealing charge combinaiton mechanism through *J-V-T* and *C-V* studies. Therefore this PhD project covers the following research contents:

(1)A new fabrication method of hot wire oxidation sublimation method for thin films of MoO_x, WO_x, and VO_x was established and developed. The processing parameters for such thin films fabrication were systematically optimized. The obtained micro-morphology, photoelectric properties, and electronic state of the thin films were analyzed and studied.

(2) The new silicon heterojunction solar cells with MoO_x, WO_x, and VO_x thin films fabricted by hot wire oxidation sublimation deposition as HTLs were developed. From the aspects of film thickness, passivation structure, and annealing process, the performance of solar cells were systematically optimized to improve the device performance.

(3) The transport mechanism of the solar cells was analyzed by means of *C-V*, dark *I-V*, and dark current density–voltage–temperature (*J–V–T*), combined with numerical simulation, for finally proposing a transport model in order to guide the research/fabrication of devices.

1.3 The content of this PhD thesis

According to the research content of the above plan, this PhD thesis is comprised of six chapters, as follows:

Chapter 1: Introduction

Chapter 2: Experimental methods and characterization

Chapter 3 Fabrication and characterization of MoO_x, WO_x and VO_x thin films

Chapter 4 The novel heterojunction solar cells with MoO_x, WO_x and VO_x thin films as HTLs

Chapter 5 Transport mechanism of the heterojunction solar cells

Chapter 6 Summary and Prospect

Chapter 2. Experimental and methods

In this chapter, the experiment and characterization methods in this thesis are introduced, which include: (1) material preparation; (2) characterization of material properties; (3) preparation of solar cells; (4) characterization methods of solar cells performance.

2.1 Material Fabrication

2.1.1 Cleaning and preparation of substrates

Glass substrates were applied for producing devices only for studying the optical property, conductivity, and morphology of thin films. They were cut into 2×2 cm^2 and immersed in detergent for sonication for 20 min, then flushed with deionized water for 5 min. They were again sonicated in acetone solution for 30 minutes and washed by deionized water for 3 minutes. Finally, ultrasonic cleaning for the substrates was performed in ethanol solution for 15 min, followed by drying under nitrogen[85-88].

Silicon wafers were employed as substrates of thin films fabrication for solar cells. The standard RCA cleaning method is adopted for their successive cleaning silicon in the following steps：(1) they were firstly cleaned in (SPM) solution, (H_2SO_4/H_2O_2 with a volume ratio of 5:1) at 120 °C for 20min; (2) afterwards they were added into HF solution (5%，wt/wt%) at room temperature for 10 min; (3) then they were placed in (APM) solution (NH_4OH: H_2O_2: H_2O with volume ratio of 1:2:5) at 80 °C for 20 min; (4) finally they were immersed in a mixture of HCl: H_2O_2: H_2O with a volume ratio of 1:2:5 (HPM solution) at 85 °C for 20 min, followed by 2 minute-long treatment in 4% HF solution[89, 90].

2.1.2 Fabrication of MoO_x, WO_x, and VO_x films

Hot-wire oxidation sublimation deposition (HWOSD) method was used to fabricate MoO_x, WO_x, and VO_x films, as shown in Figure 2.1: (a) In a vacuum chamber, oxygen and high temperature (in range of 600-1100 °C) hot wires of transition metals (such as:Mo, W, and V) were reacted, generating their oxides on surfaces, which sublimated simultaneously and spread into the whole chamber in the form of molecular clusters, then deposited on the substrate surface, forming the transition metal oxide thin film.

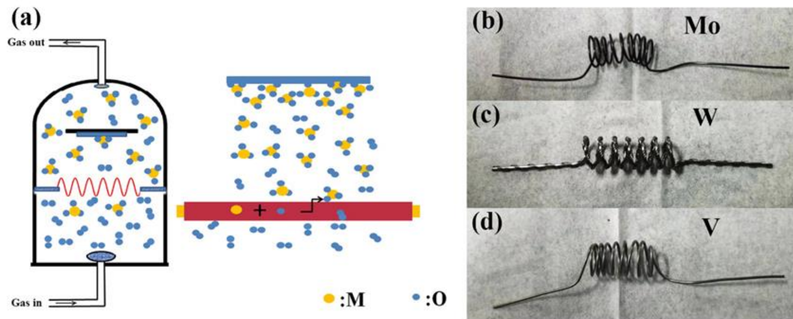

Figure 2.1 (a) Schematic diagram of hot-wire oxidation sublimation deposition method, (b) Molybdenum wire (diameter d = 1.0 mm), (c) Tungsten wire (Two tungsten wires with diameter d = 1.0 mm are intertwined), (d) Vanadium wire (diameter d = 1.0 mm).

Such process of fabricating thin film materials by HWOSD method contained the following stages: (1) Oxidation reaction: where a wire generated high temperature under the electric current due to its own electrical resistance, providing heat for its oxidation reaction with oxygen. The high-temperature transition metal on the surface of the hot wire was oxidized to generate a transition metal oxide. The current was controlled for the oxidation rates and the film quality. (2) Physical sublimation: high temperature influenced the sublimation rate, which in turn affected the growth rate of the oxide material on the substrate. (3) Diffusion deposition: The transition metal oxide sublimated from the surface of the hot-wire and entered into the vacuum chamber, with random diffusion for the deposition of the transition metal oxide film on the substrate surface.

2.2 Characterization of material properties

In this these， the characteristics of the materials of MoO_x, WO_x, and VO_x thin films were analyzed by the following methods, as listed in the Table 2.1

Table 2.1 Material characterization equipments of MoO_x, WO_x, and VO_x thin films

Characteristic of material	Test equipment	model of test equipment
Thickness	Step profiler	ERUKER-Dektak XT
Transmission and reflection	UV-VIS spectrophotometer	Hitachi UV4100
Morphology	SEM	Hitachi SU8010
Roughness and potential of surface	AFM/SPM	NT-MDT
Structure and phase	XRD	Rigaku, Ultima IV
Elemental composition	XPS	Thermo Scientific PHI5000
Effective minority lifetime	QSSPC	Sinton WCT-120

2.3 Fabrication of solar cells

In this study, the different structures of solar cells were designed. The fabrication process of solar cells mainly included the following steps:

2.3.1 Texture of silicon wafer

The silicon wafers were anisotropically etched for 8 minutes by a mixed solution of 6% NaOH and 2% isopropyl alcohol at 60-80 °C, followed by a post-treatment on textured silicon by using 2% tetramethylammonium hydroxide solution. Then RCA standard was implemented to remove impurities from the surface of textured silicon wafers.

2.3.2 Preparation of amorphous silicon passivation layer

The textured silicon wafer was rinsed in HF solution with concentration of 2% for 1 min to remove the oxide layer on the surface, and immediately put into the PECVD sample chamber. When the experimental conditions of 4×10^{-5} Pa and 200 °C was obtained, a certain amount of Ar gas was introduced, followed by SiH_4 and H_2 when glowing under RF power, the thickness was controlled by the sample baffle for preparation of the amorphous silicon film. Then, the samples were transferred to the

doping cavity through a manipulator to deposit n-type doped amorphous silicon films with the presence of certain proportions of PH_3, SiH_4, and H_2 as the precursor gas.

2.3.3 Preparation of transparent conductive film

In this work, optical transparent conductive films of the solar cell are composed of indium tin oxide (ITO) with their thickness of 70 nm-100 nm. They were sputtered by using oxide ceramic target of In_2O_3 and SnO_2 (weight ratio 90:10) firstly under vacuum (ca. 4×10^{-4} Pa) and then at the presence of a certain amount of Ar and O_2. The distance between the target and the sample was 5 cm, while the thickness of ITO thin films was controlled by the opening time of a baffle.

2.3.4 Preparation of electrodes

The front electrode (incident surface) was Ag grid, and the back electrode was Ag film and Mg/Al for different solar cell structures. They were thermally evaporated by using a molybdenum boat for Ag electrode, a high-temperature tapered ceramic boat for Mg electrode, and a tungsten spiral coil for Al electrode. According to the characteristics of different electrodes, mask plates with different structures were selected.

2.4 Characterization methods for solar cells

2.4.1 The *J-V* characterization for solar cells

J-V test under standard illumination conditions (AM1.5 100mW/cm^2, 25 °C) is the most direct characterization method to evaluate a solar cell's performance, as shown in Figure 2.2.

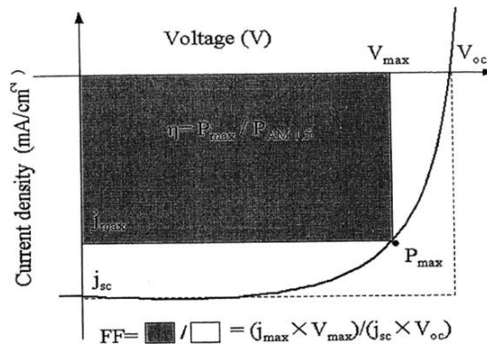

Figure 2.2 The scheme of J-V curve for a solar cell.

Open circuit voltage (V_{OC}) is the maximum voltage of the solar cell when its current is 0 under the standard sunlight irradiation. The essence of V_{OC} is the separation ability of the solar cell for its internal photo-generated carriers. In a *J-V* curve, the V_{OC} of solar cell is the intersection of the curve and x-axis. It is mainly affected by the built-in electric field, carrier recombination, and parallel resistance. In novel heterojunction solar cells, the potential height of the barrier formed by the contact between the carrier-selective transport layer and Si play a role in both the built-in electric field and the V_{OC} of a solar cell. According to the location of carrier recombination, interface recombination and internal recombination had been explored. In new heterojunction solar cells, the former is the dominated one. The reverse saturated current of a solar cell is the most important parameter to evaluate interface quality of a device, being reverse logarithm with its V_{OC}. Having the same order of magnitude with the series resistance, the parallel one can significantly affect the V_{OC} of the devices.

Short circuit current density (J_{SC}) refers to the maximum output current per unit area of solar cells which are short circuited under illumination conditions, i.e., when the V_{OC} is zero). In the *J-V* curve, J_{SC} of solar cell is the intersection of the curve and y-axis, which is generally considered to embody the carrier collection capacity of the whole device. J_{SC} is affected by various factors, such as the thickness of the absorption layer, the surface trapping characteristics, the optical absorption coefficient of each layered material, light coupling and light trapping effect. In addition, when the series resistance is too large, J_{SC} shows an obvious trend of decline.

Fill factor (FF) is defined as:

$$FF = \frac{I_{max} * V_{max}}{I_{sc*} * V_{oc}} \tag{2.1}$$

Where, I_{max} and V_{max} are respectively the output current and voltage corresponding to the maximum power point of the solar cell.

FF, as illustrated in Figure 2.2, is the proportion of the rectangular area of the shadow part of the solar cell in the *J-V* diagram in that of the dotted one formed by the two coordinate axes and V_{OC} and J_{SC}. FF of the device indicates the carrier loss in the process of internal transport, including recombination loss, resistance loss, and short-circuit loss. The more serious the carrier recombination in the device there are, the greater the recombination loss and the smaller FF will be. The series resistance of the device includes interface contact resistance and bulk resistance. With the increase of series resistance, the resistance loss of the device increases and the FF of the device decreases obviously. The short-circuit loss of the device is due to the decrease of its parallel resistance.

The series resistance includes the body resistance of each layer of the solar cell, the contact resistance of interface, the transverse resistance of the front surface grid electrode and back surface electrode, and the contact resistance of the contact interface. When the current through the device is 0, the series resistance has no effect on the V_{OC} of the solar cell. However, when the current passes through the device, a voltage drop will be generated at the output end of the solar cell due to the existence of series resistance. The larger the series resistance of the device is, the smaller the FF and J_{SC} become.

Parallel resistance shows the leakage current of the working junction of the solar cell, including the leakage from the junction inside and the junction edge caused by crystal defects and external deposition of dopants.

The power conversion efficiency (PCE) is the ratio of the electric energy generated by solar cells to all incident light energy, which is the most direct performance parameter of solar cells. Under the irradiation of standard solar light source AM1.5 (P_{in} = 100 mW/cm^2), the calculation formula of power conversion efficiency of solar cell is as follows:

$$\eta = \frac{J_{SC}*V_{OC}*FF}{P_{in}} = \frac{J_{SC}*V_{OC}*FF}{100\, mW/cm^2} \qquad (2.2)$$

Where as η stands for PCE, and J_{sc}, V_{oc}, and FF are as above-introduced.

2.4.2 Quantum efficiency of solar cells

The short-circuit current of the solar cell has a great dependency on the incident photon energy. In order to study the contribution of incident photons of different energies to short-circuit current, quantum efficiency (QE) spectra is a well-adopted evaluation method, which has two expressions: external quantum efficiency (EQE) and internal quantum efficiency (IQE). The most commonly used one is the EQE, which is the probability that photon with a wavelength of λ can provide a photon to the external circuit, expressed by the following formula:

$$EQE(\lambda) = \frac{I_{SC}(\lambda)}{q \cdot A \cdot Q(\lambda)} \qquad (2.3)$$

Where: Q (λ) is the incident photon density, and A is the area of the solar cell.

2.4.3 High frequency capacitance - voltage (*C-V*) of solar cells

There is a certain dependence between the capacitance and bias voltage of solar cells, the *C-V* analysis of solar cells has become a common method to study the PN junction

interface properties of solar cells[91]. It measures the relationship between the capacitance of the solar cell and the DC bias voltage applied to the solar cell when a high frequency perturbation AC voltage (1MHz, 10mV) is applied to the solar cell.

For a PN junction, the junction capacitance consists of barrier capacitance (C_T) and diffusion capacitance (C_D). When the AC voltage frequency of PN junction exceeds 1M, C_D can be ignored.

Under the reverse bias voltage, the barrier capacitance C_T of single-sided abrupt PN junction per unit area is as follows:

$$C_T = \sqrt{\frac{\varepsilon_r \varepsilon_0 q N_D}{2(V_D - V_F)}} \tag{2.4}$$

Where: ε_r is the dielectric constant of the silicon wafer, ε_0 is the vacuum dielectric constant, N_D is the doping concentration of the silicon wafer, V_D is the contact potential difference of the abrupt junction, and V_F is the applied bias voltage.

To square the equation (2.4) and take the reciprocal leads to:

$$\frac{1}{C_T^2} = \frac{2(V_D - V)}{\varepsilon_r \varepsilon_0 q N_D} \tag{2.5}$$

Furthermore, the derivative of V from equation (2.5) is obtained:

$$\frac{d\left(\frac{1}{C_T^2}\right)}{dV} = \frac{2}{\varepsilon_r \varepsilon_0 q N_D} \tag{2.6}$$

Plotting $1/C^2 \sim V$ curves from the experimental data could result in a straight line in an ideal case, whose slope will lead to the N_D value of the substrate. According to the intercept of the straight line on the X axis, the contact potential difference V_D of the abrupt PN junction can be obtained. At the same time, the barrier width X_D of p^+n single side abrupt junction is obtained as below:

$$X_D = x_n = \sqrt{\frac{2\varepsilon_r \varepsilon_0 V_D}{q N_D}} \tag{2.7}$$

For the transition metal oxide (TMO)/i a-Si:H/Si heterojunction, due to the great difference of work functions between TMO and n-type crystalline silicon, a large energy band bend occurs on the interface of crystalline silicon in the junction region, which shows the characteristics of barrier capacitance. In the third chapter, we will introduce the conductivity of TMO film in a magnitude of about 10^{-6} S/cm, which is

similar to that of medium doped amorphous silicon. It indicates that there is certain magnitude of free carriers in TMO, but the conductivity or carrier concentration of TMO does not reach the level of high doping. Therefore, the *C-V* characteristics of TMO/i a-Si:H/Si heterojunction can unseemly be analyzed completely according to the single side mutation PN junction. However, considering that the thickness of TMO and intrinsic amorphous silicon layers are relatively thin, the space charge region is mainly located on the side of crystalline silicon. When the DC bias voltage changes, it is the space charge area width mainly on the silicon side that would be adjusted. Moreover, we have observed the influence of bias voltage on capacitance. Therefore, the relative size of the intercept of *C-V* curve on the x-axis can still indicate the phase of built-in potential on the silicon side. In addition, song *et al.[92]*, pointed out that the slope of *C-V* curve can imply the quality of heterojunction interface to a certain extent under the same doping concentration of crystalline silicon substrate.

2.4.4 Dark *I-V* measurement on solar cells

Dark *I-V* of solar cells is usually used to study the recombination mechanism of carriers in devices. By studying the reverse saturation current density of dark *I-V* in negative bias region, the recombination of minority carriers at the interface of devices can be studied, and diode ideal factor and series and parallel resistance of the device can also be obtained. The dark *I-V* analysis of solar cells is based on a two-diode model, where an equivalent circuit diagram is shown in Figure 2.3. Diodes 1 and 2 represent the diffusion process of carriers and the recombination mechanism of depletion region of solar cells, respectively.

It can be seen from Figure 2.3 that the current of the solar cell is composed of four parts:

$$I(V) = I_{D1} + I_{D2} + I_{Rp} + I_L \qquad (2.8)$$

$$I(V) = I_{01}\left[exp\frac{q(V-IR_S)}{n_1 kT} - 1\right] + I_{02}\left[exp\frac{q(V-IR_S)}{n_2 kT}\right] + \frac{V-IR_S}{R_{sh}} + I_L \qquad (2.9)$$

Whereas I_{01} and I_{02} represent the saturation current of diodes 1 and 2 respectively, n_1 and n_2 represent the ideal factors of corresponding diodes, q is the electronic charge, K is the Boltzmann constant, T stands for the operating temperature of the device, and R_S and R_{SH} are the series resistance and parallel resistance of the device, respectively.

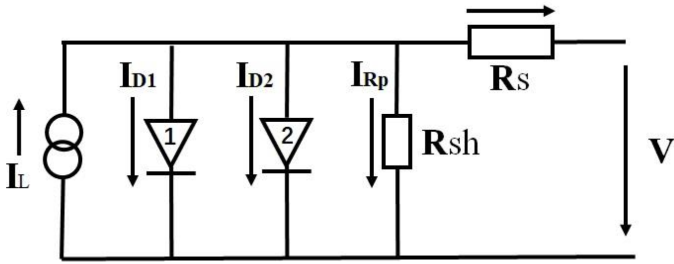

Figure 2.3 Equivalent circuit for two-diode model[93].

The contribution of two diodes to the device current is described from the first two terms in equation (2.9), which represents two different transport mechanisms. The diode current is affected by the ideal factor n and saturation current *I*. When n_1=1, it represents the carrier diffusion process in solar cells at room temperature. Diode 2 usually reflects the recombination process of depletion region, and the theoretical value of n_2 should be 2. In practical devices, tunneling and other processes will affect the value of n_2. Figure 2.4 shows the typical dark *I-V* curve of solar cells at room temperature, which is divided into four different regions to study the main factors affecting the current of solar cells: i.) when V< 0.15V, the current of solar cells in this region is mainly affected by the device parallel resistance R_{SH}; ii.) when 0.15 V< V <0.45V, the solar cell current is preferably affected by the second term in equation (2.9), that is, it is controlled by the non-ideal transport mechanism. For PN junction, it is generally considered as the composite current in the depletion region. iii.) when 0.45 V< V <0.6V, the current of the solar cell depends on the first term in equation (2.9), which is mainly affected by the ideal transport mechanism; iv.) when V>0.6 V, the series resistance becomes the main factor affecting the current. For specific devices, the division of the above voltage range will be slightly different.

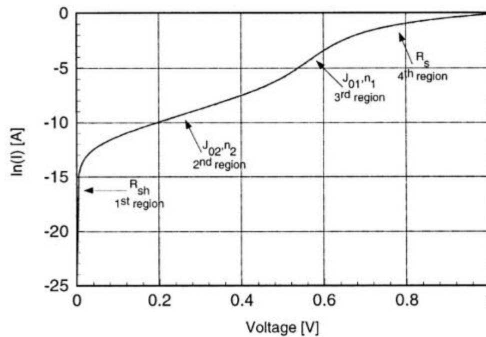

Figure 2.4 Representative dark I-V curve of a solar cell with the different regions[93].

In equation (2.9), when I >> I_0, the first two exponential terms can be approximated into follows:

$$I_{Di} = I_{oi}\left[exp\frac{q(V-IR_S)}{n_i kT}\right] \tag{2.10}$$

The logarithm of the above equation can be obtained:

$$lnI_{Di} = lnI_{0i} + K_i * V' \tag{2.11}$$

Whereas， $i = 1,2$; $K_i = q/(n_i kT)$; $V' = V - IR_s$;

According to equation (2.11), plotting lnI_{Di} versus V' will lead to a straight line. From its slope, the ideal factor n of the diode can be obtained. According to the intercept between the line and Y-axis, the dark saturation current of the diode can be obtained.

In addition, dark *I-V-T* curves are often used to analyze the transport mechanism of solar cells[94]. It is generally believed that there are four carrier transport mechanisms in silicon heterojunction devices including diffusion, thermal emission, recombination and tunneling. The relationship between current density and voltage is as follows:

$$J = J_0 \exp(A * V) \tag{2.12}$$

$$J_0 \propto exp(-E_a/KT) \tag{2.13}$$

Where J_0 is the saturation current density, corresponding to I_{01} and I_{02} of unit area in different voltage ranges; E_A is the activation energy, and the coefficient A is related to the transport mechanism of the device:

$$A = q/nkT \tag{2.14}$$

It shows that A is affected by the ideal factor and temperature. However, when tunneling is applied as the transport mechanism of the device, A becomes independent with temperature T.

Chapter 3. Fabrication and characterization of MoO_x, WO_x, and VO_x Thin Films

Transition metal oxide (TMO)， such as MoO_x, WO_x and VO_x， has been widely used as efficient catalysts in production of alcohol, alkane, olefin, and nitric oxide. In recent years, due to their wide band gap width, large work function (≥6.0 eV), and high transmittance, MoO_x, WO_x, and VO_x have been used as carrier selective transport layer materials in fabrication of semiconductor devices, especially solar cells. Remarkably, the new heterojunction solar cell with MoO_x film as the hole selective transport layer has achieved a power conversion efficiency of 22.5%, demonstrating the great potential of TMOs in the field of semiconductor devices[41].

At present, state-of-art fabrication methods of MoO_x,WO_x, and VO_x thin films are: thermal evaporation, electron beam evaporation, atomic layer deposition (ALD), sputtering, solution, and so on, with both obvious advantages and shortcomings from each own. For example, thermal evaporation is the most commonly method to fabricate TMO. The crystalline silicon solar cells with MoO_x as the hole-selective transport layer by this method have obtained the highest power conversion efficiency of 23.5%. However, such thermal evaporation method can easily cause splashing of the evaporated material, not only wasting raw materials but also limiting continuous large area production. Although electron beam evaporation and atomic layer deposition can produce high-quality TMO thin films, high cost of prevent from their large-scale industrial production. The main disadvantage of the sputtering method comes from easily causing damages to other functional layers on the substrate surface, affecting device interface characteristics and thus the performance of the solar cells. Even though solution method can be free of demanding expensive equipment, the material fabricated by this a way can hardly ensure uniformed film thickness and their work functions are low. As reported by Scott R. Hammond *et al.*[76], the work function of the MoO_x prepared by the solution method was 5.0 eV, being 1.9 eV lower than that prepared by thermal evaporation and not beneficial for energy bands' bending, thus affecting the open circuit voltage of the device.

In order to overcome the problems in the above-mentioned methods, based on previous achievements in our group, we proposed HWOSD method for fabricating MoO_x, WO_x and VO_x films. An amorphous MoO_x thin film material with excellent photoelectric performance had been obtained by this method. This chapter focuses on the HWOSD's working principle and optimization of certain processing parameters and material properties of these TMO thin films.

3.1 Optimization of fabricating parameters of TMO thin films

As having been briefly introduced in Chapter 2, when fabricating TMO films by HWOSD technology, the temperature of hot wire and oxygen pressure turn to be very important parameters affecting the film quality. Here in this chapter, we focus on optimizing the growth of thin films from these two aspects.

3.1.1 The effect of hot wire temperature in the fabrication of MoO_x, WO_x, and VO_x thin films

The temperature of hot-wire is one of the important parameters affecting the thin film preparation, which not only ensure its complete reaction with oxygen, but also promote the rapid sublimation of the generated TMO materials. Being controlled by adjusting the current of the hot-wire, the temperature must not be too high to prevent melting the hot-wire. by. Figure 3.1 shows the corresponding relationship between current and temperature of molybdenum wire (a), tungsten wire (b), and vanadium wire (b), respectively.

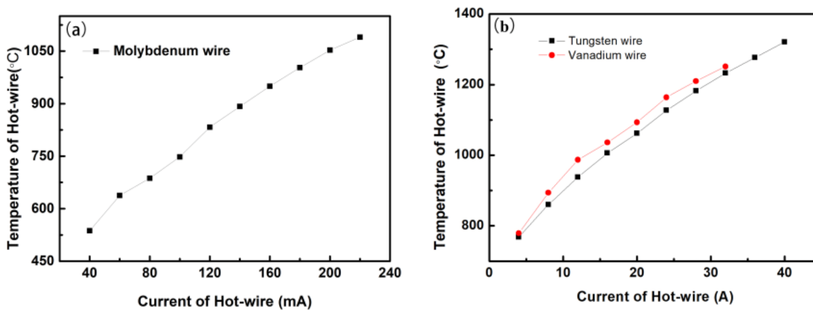

Figure 3.1 (a) Dependence of the molybdenum wire temperatures on current, (b) Dependence of the temperatures of tungsten wire and vanadium wire on current.

As can be seen in Figure 3.1, the current of the hot-wire is roughly linear with temperature, proving that the temperature of the hot wire can be precisely controlled by adjusting the current. It was found that depositing temperature for the different oxide films from different hot-wires varied significantly. When the temperature of the molybdenum wire exceeded 750 °C, a thin film of molybdenum oxide was deposited on the surface of the polished silicon substrate. However, if a tungsten wire is used, higher temperature exceed 1000 °C was required to obtain a tungsten oxide film, and even higher temperature of about 1200 °C was an obligation for obtaining a vanadium oxide film. The above experimental phenomena can be related to the melting/boiling

point of TMOs (see Table 3.1), from which it can be found out that the evaporation temperature of MoO_x and WO_x is lower than their melting point, suggesting sublimating. The evaporation temperature of VO_x is much higher than its melting point, so it should be a process of melting first and then evaporation.

Table 3.1 Comparison of melting and boiling points of various transition metals and their corresponding oxides.

	Mo	MoO_x	W	WO_x	V	VO_x
T_m (°C)	2620	795	3410	1473	1890	600
T_b (°C)	5560	1155	5927	1837	3000	1750

Note: T_m and T_b stands for melting Point and boiling point, respectively.

The thickness of the film was measured by using a stylus profiler, and the TMO deposition rate at different hot-wire temperatures was given according to the deposition time, as shown in Table 3.2.

Table 3.2 Correspondence relations between hot wire temperature and deposition rate of transition metal oxide films.

T(°C)		750	900	1050	1200	1350
Deposition	MoO_x	1.50	4.50	6.64	10.0	14.5
rate ν	WO_x	-	0.98	3.78	5.21	8.75
(nm/min)	VO_x	-	-	-	6.2	-

From Table 3.2, it can be seen that, with the increase of temperature, the deposition rate of both MoO_x and WO_x increased. The elevated temperature of the hot-wires led to their increasing internal energy, weakening the intermolecular forces and accelerating the sublimation rate of the oxides. The deposition of vanadium oxide film was subjected to reaction heat, resulting in their melting. Only when the temperature of the vanadium wire was 1200 °C, the deposition rate of 6.2 nm/min could be obtained.

It was also found that the melting point of these metals has a large gap with gthat of their oxides, which can ensure a complete oxidation of the transition metals and a stable sublimation for forming a high-quality film on the substrate. It is therefore finally concluded that the temperature of 1050 ℃ becoming the optimal temperature for the deposition of MoO_x in the fabrication of semiconductor devices. Similarly, the deposition temperature of WO_x and VO_x we chose were optimized as 1200 °C, being

the fabrication temperature of the thin film material in the subsequent material preparation and solar cell fabrication.

3.1.2 Effect of oxygen pressure on the deposition of MoO_x and WO_x

In the process of fabricating the transition metal oxide film via HWOSD method, oxygen pressure in the chamber was a main parameter that affected deposition of the TMO materials. A series of MoO_x and WO_x films with the same thickness were fabricated under different oxygen pressure. Their growth rate and transmittance in the visible region were systematically studied.

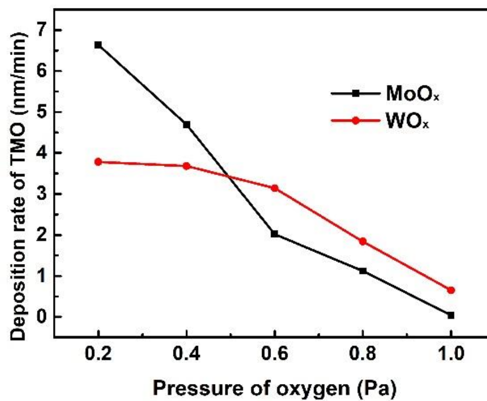

Figure 3.2 Effect of different oxygen pressures on the deposition rate of TMO films.

The deposition rate of MoO_x and WO_x under different oxygen pressures is illustrated in Figure 3.2. It can be seen that, at the optimized temperature of 1050 °C, the deposition rate of transition metal oxides exhibited a falling trend with the increasing oxygen pressure. Mainly the surface area of the hot wire was fixed, so the amount of oxygen needed for reacting with the molybdenum wire was constant per unit time. When oxygen took up the active position on the surface of the hot-wire, the excess oxygen could not participate the reaction anymore, so the rise of oxygen pressure would not accelerate the oxidation rate of molybdenum wires. In other word, due to the collision with oxygen molecules, scattering of the gaseous MoO_x and WO_x molecules was enhanced, showing a gradual decrease in the oxide deposition rate.

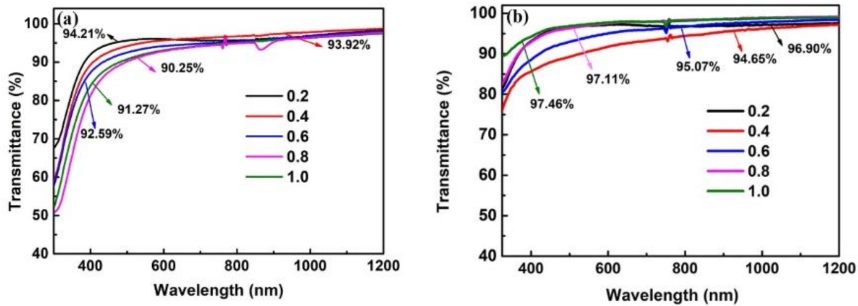

Figure 3.3 The transmittance of films of MoO_x (a) and WO_x (b) under different oxygen pressure.

Figure 3.3 shows the transmittance of MoO_x (a) and WO_x (b) films with the same thickness (15nm) fabricated under different oxygen pressure of 0.2, 0.4, 0.6, 0.8, and 1.0 Pa, respectively, in the visible range (300-1200nm). As can be seen in Figure 3.3(a), in the long wave region of 800-1200 nm, the transmittance of MoO_x under different oxygen pressures showed little changes, while significant difference on their transmittance were found in the medium and short-wave range (300-800 nm) under different oxygen pressure. The lower the oxygen pressure was, the greater the light transmittance became. The possible reason for such differences in the transmittance of the MoO_x film could be that varied chemical composition and structural were formed at different pressure of oxygen. When the it was 0.2, 0.4, 0.6, 0.8, and 1.0 Pa, the average transmittance of the MoO_x film in the visible light (300-1200 nm) region was 94.21%, 93.92%, 92.59%, 90.25%, and 91.27%, respectively. In general, the molybdenum oxide films have high transmittance in the pressure range in which we were interested. When the oxygen pressure was 0.2 Pa, the molybdenum oxide film pronounced its best optical performance.

The transmittance of the WO_x thin films is displayed in Figure 3.3(b). In the long wave (800–1200 nm) region, oxygen pressure had little influences on their transmittance, while in the medium and short wave (300–800 nm) range, relatively larger oxygen impacts on WO_x than MoO_x were pronounced. Unlike the latter ones, as the oxygen pressure got higher, the average transmittance of the WO_x films declined firstly from 96.90% at 0.2 Pa to 94.65% at 0.4 Pa and then increased to 97.46% at 1.0 Pa, exhibiting better transmittance in the visible light section. Due to the particular thermal property of vanadium wire, we directly choose 1.0 Pa as the oxygen pressure for VO_x deposition.

Through the above pressure optimization on deposition of MoO_x and WO_x, 0.2 and 1.0 Pa were concluded for fabricating the subsequent materials and devices by using MoO_x. and WO_x, respectively.

3.2 Material features of films of MoO_x, WO_x, and VO_x

After optimizing the TMO preparation process, the features of MoO_x, WO_x and VO_x thin films via HWOSD were systematically studied.

3.2.1 Morphology of MoO_x, WO_x and VO_x thin films

The microscopic morphology of TMO thin films determines the quality of the interface formed with other materials to a great extent. MoO_x, WO_x, and VO_x films were deposited on polished silicon wafers and random pyramid substrates, respectively, to observe the morphological characteristics of oxide films on different substrates.

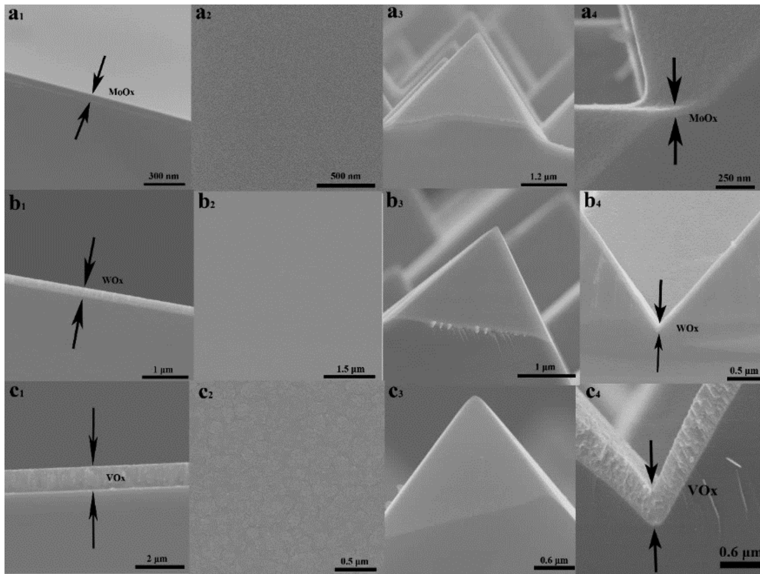

Figure 3.4 SEM images of MoO_x (a), WO_x (b) and VO_x (c) on different substrates: 1 & 2, SEM images on a polished silicon wafer; and 3 & 4 on textured silicon wafers.

Figure 3.4 (a_1-a_4) are SEM images of MoO_x thin film fabricated on different substrates under optimized deposition conditions (hot-wire temperature of 1050 °C and oxygen pressure of 0.2 Pa) by means of HWOSD. For deposition of MoO_x on a polished

silicon wafer, Figure 3.4 (a_1) displays a cross-sectional view of MoO_x film with uniformed thickness. As can be seen from Figure3.4 (a_2), the top view of the MoO_x film deposited on the polished silicon wafer exhibited uniform distribution on the surface of the polished silicon wafer. The MoO_x films on textured silicon wafers can form a good coverage of the random pyramid light trapping structure, as shown in Figures3.4 (a_3) and (a_4).

WO_x (under W wire temperature of 1200 °C and oxygen pressure of 1.0 Pa) and VO_x films (with V wire temperature of 1200 °C and oxygen pressure of 1.0 Pa) were fabricated on different substrates under the optimized preparation process. Figure 3.4 (b_1) and (c_1) proved that HWOSD method can also achieve uniform growth of WO_x and VO_x thin films on polished silicon wafers. On the surface of the silicon wafer with random pyramid texture, WO_x and VO_x can also achieve the "conformal" deposition of the light trapping structure, thereby creating the necessary conditions for the subsequent formation of an ideal device interface.

The atomic force microscopy (AFM) were used to characterize the roughness and phase of each film under optimal processing conditions, as shown in Figure 3.5.

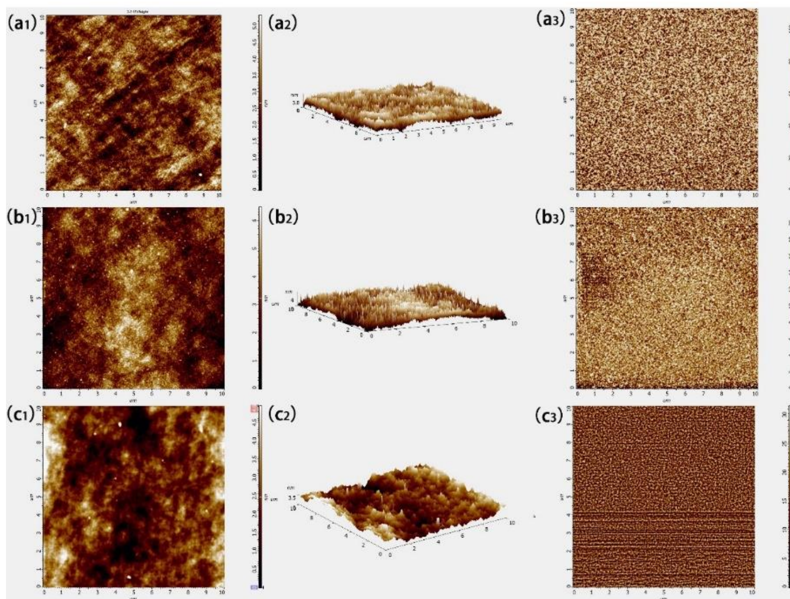

Figure 3.5 AFM height images (1 & 2 series) and phase diagrams (3 series) of TMO films (for MoO_x, WO_x, and VO_x)

Figure 3.5 (a_1) and (a_2) are the 2D and 3D height graphs of the MoO_x films deposited on the surface of the polished silicon wafer, respectively. The root mean square roughness (RMS, Sq) in the scanning range of the MoO_x film was 1.10 nm, and the average roughness was 0.88 nm. The phase diagram of MoO_x is shown in Figure 3.6 (a_3), and the scale on the right is the phase difference between the reflected laser signal of the needle tip and the excitation signal of the needle tip caused by the sample, which represents the sensitivity of different elements in the sample to the tip. The light and dark distributions in the phase diagram in this study respectively represent the distribution of Mo and O element in the sample, which are evenly distributed in the MoO_x film fabricated by HWOSD.

The height diagram of WO_x film on the surface of the polished silicon wafer is shown in Figure 3.5 (b_1) and (b_2). The RMS roughness Sq of the WO_x films was 1.32 nm, and the average roughness was 1.06 nm. The phase diagram of WO_x film (b_3) also showed that the WO_x film prepared in this study had a uniform phase in figure 3.5 (b_3). The RMS roughness Sq of VO_x films (Figure 3.6 c_1 and c_2) fabricated by HWOSD method was 1.44 nm, and the average roughness was 1.14 nm. Figure 3.5 (c_3) is the VO_x phase diagram, with similar results obtained as MoO_x and WO_x films.

By analyzing the morphological characteristics of transition metal oxides via SEM and AFM, MoO_x, WO_x, and VO_x thin films deposited by HWOSD possessed uniform thickness and smooth surface. They could achieve "conformal" deposition on the textured surface which was important to the subsequent application of MoO_x, WO_x, and VO_x in solar cells.

3.2.2 Structural characteristics of MoO_x, WO_x, and VO_x

The structural characteristics of MoO_x, WO_x and VO_x were characterized by X-ray diffraction (XRD), and the effects of different annealing temperatures on the structure of MoO_x and WO_x thin films were studied.

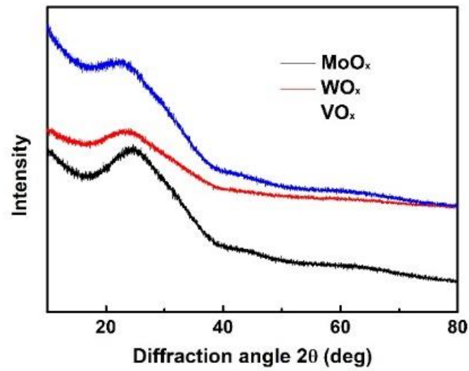

Figure 3.6 X-ray diffractogramof transition metal oxides (MoO_x, WO_x, and VO_x).

The X-ray diffractograms of MoO_x, WO_x, and VO_x films on the glass substrate are shown in Figure 3.6. It can be seen that the XRD diffractogram of the three oxide films appeared similar, and no characteristic peaks were presented, indicating an amorphous film, which was related to the relatively low substrate temperature (<200 °C).

3.2.3 The electronic structure of MoO_x, WO_x, and VO_x

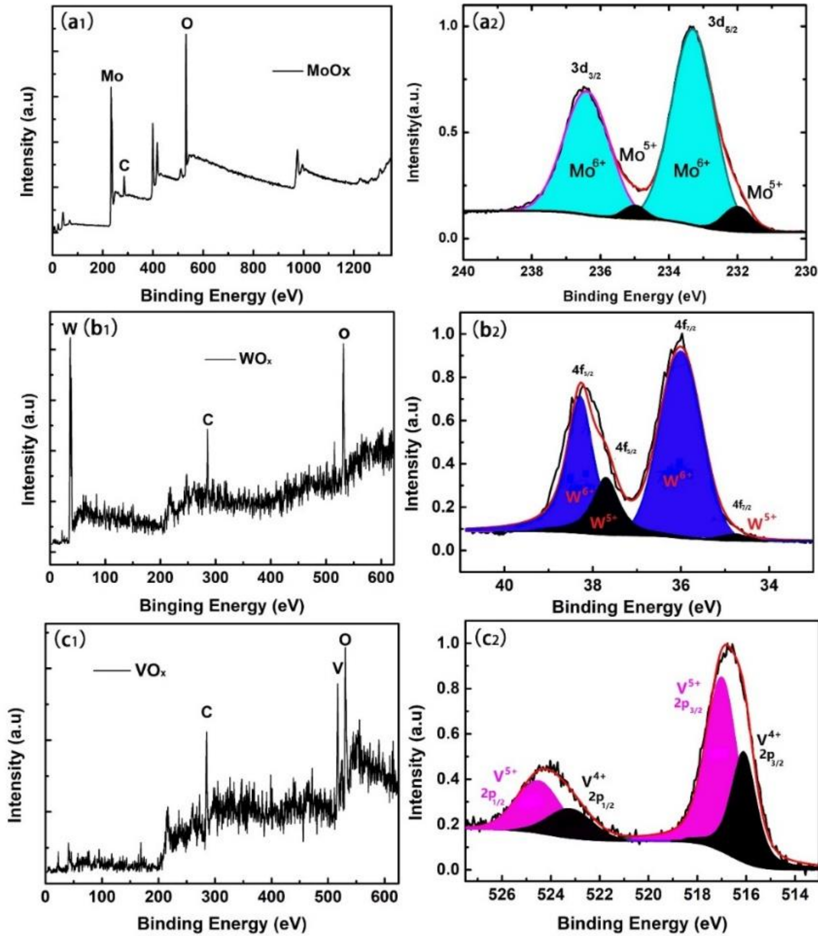

Figure 3.7 X-ray photoelectron spectroscopy (XPS) of MoO_x (a_1), WO_x(b_1), and VO_x (c_1) andspectra for: Mo 3d core level in MoO_x films (a_2), W 4f core level for WO_x films (b_2), and V 2p core level VO_x films (c_2).

X-ray photoelectron spectroscopy (XPS) was used to analyze the electronic structure characteristics of oxide films. Figure 3.7 (a_1, b_1, c_1) present the XPS spectra of MoO_x, WO_x, and VO_x within the entire scanning range, respectively. According to the XPS standards, the approximate position of the element contained in the oxide are found, providing a specific energy interval for the second accurate scan.

The XPS spectrum of the 3d electron of Mo element in the range of binding energy (BE) of 230 to 240 eV， the MoO_x sample was subjected to a second fine sweep, and the XPS peaking software was used for the obtained data (XPSPEAK) can be processed to obtain Figure 3.7 (a_2). The positions of the BE at 233.3 and 236.4 eV correspond to the $3d_{5/2}$ and $3d_{3/2}$ orbital electrons of Mo^{6+}, respectively, and the characteristic peaks at 232eV and 235eV originate from the 3d orbital electrons of Mo^{5+}[95]. By fitting and normalizing the characteristic peaks, the content ratio between Mo^{6+} and Mo^{5+}(shaded area ratio) in MoO_x can be obtained, and the stoichiometric number x in MoO_x is estimated to be 2.94. This value is higher than the result of 2.79-2.86 in MoO_x reported in the previous literature[43], which shows that the higher oxidation state of molybdenum element in MoO_x fabricated by HWOSD method, implying that the thin film material could have a larger work function.

In the same way, the second fine sweep of the characteristic peak of the W element in WO_x thin film material can obtained as shown Figure 3.7 (b_2). The BE at the positions of 36.0 eV and 38.2 eV corresponds to +6 valence of W ions occupying $4f_{7/2}$ and $4f_{5/2}$ electron orbitals, respectively. At the positions where the BE are 34.8 eV and 37.0 eV, the +5 valent W ions occupying $4f_{7/2}$ and $4f_{5/2}$ electron orbitals are presented[45]. Similarly, fitting and normalizing the characteristic peaks resulted in the ratio of 5.33: 1 between W element of +6 and +5 valence in tungsten oxide prepared by this HWOSD method. It is inferred that the value of x in WO_x is roughly 2.91, which also shows a higher degree of oxidation of tungsten element in the tungsten oxide prepared by HWOSD method.

The characteristic peak of vanadium element of the VO_x thin film was presented in Figure 3.7 (c_2). The positions where the BE are 515.9 and 523.1 eV correspond to +4 valence V ions in the electronic states of $2p_{3/2}$ and $2p_{1/2}$, respectively, while 517.1 and 524.2 eV correspond to their electronic states of $2p_{3/2}$ and $2p_{1/2}$ for V ions of +5 valence[96]. After fitting and normalizing the characteristic peaks, it can be seen that the content ratio of vanadium elements at +4 and +5 in VO_x is 1:1.79, and the value of X in VO_x was estimated to be about 2.32. The reason for the reduced oxidation of vanadium V in VO_x could be related to the instability of V_2O_5 being easily decomposed into O_2 and V_2O_4.

3.2.4 Optical properties of MoO_x, WO_x, and VO_x

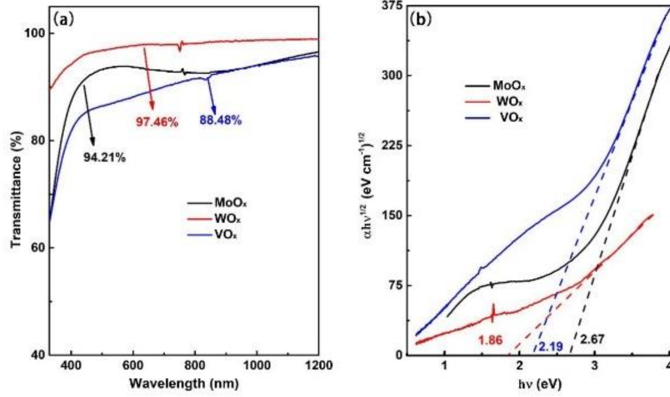

Fig. 3.8 The transmittance (a) and optical band gap (b) of TMOs.

Figure. 3.8 (a) is a comparison diagram of the transmittance of films of MoO_x, WO_x, and VO_x with the same thickness (15nm) fabricated under optimal conditions. It can be seen that TMOs with the same thickness have different light transmittance. The average transmittance of WO_x film in the wavelength range of 300–1200 nm is as high as 97.46%, indicating that it has excellent optical performance. MoO_x also has good transmittance, with an average light transmittance of 94.21%. Compared to WO_x and MoO_x, VO_x films have a bit worse light transmittance, with an average transmittance of 88.48%. In general, these three TMOs all have high optical transparency. Their absorption coefficient and optical band gap of each material were analyzed [97]. The absorption coefficient of thin film material α can be expressed as:

$$\alpha = \frac{1}{d}\ln\left(\frac{1-R}{T}\right) \qquad (3.1)$$

Where T is the transmittance of the film, d is the thickness of the film, and R is the reflectance of the film material.

The relationship between the light absorption coefficient of the material and the photon energy $h\nu$ follows the Tauc law near the absorption edge:

$$\alpha\hbar v = \beta\,(\hbar v - Eg)^{r} \qquad (3.2)$$

Where β is a constant; r is an optional parameter, the indirect band gap material is 2, and the direct one is 1/2; Eg is the optical band gap of the material; $h\nu$ is the photon energy.

Assuming that the film reflectivity R is 0, and the MoO_x, WO_x, and VO_x films are amorphous silicon materials, referring to the studies of M. Anwar, SH Mohamed, and S. Sindhu, and S. Sanghi *et al.* [98-100], and knowing the indirect band gap for the three oxides, our calculate resulted in a Tauc curve, as shown in Figure 3.8 (b). Extrapolating the linear portion of the curve to the abscissa, the value corresponding to the intersection point leads to the optical band gap of the material. From Figure 3.8 (b), the optical band gaps of MoO_x, WO_x, and VO_x were 2.61 eV, 1.76 eV, and 2.10 eV, respectively. M. Anwar and other researchers[98-100] found that the optical band gap of the MoO_x film was affected by the thickness of the film itself, the deposition temperature and the annealing varing between 2.3 and 2.9, which was similar to that of the MoO_x film measured in this work. According to studies by Corsin Battaglia *et al.[40]*, The forbidden band width of the amorphous molybdenum oxide film was 3.0-3.3 eV, but the optical band gap of the MoO_x film fabricated in this experiment was 2.61 eV. SH Mohamed and other studies[99] have shown that the optical band gap of WO_x films prepared by sputtering increased with the increase of oxygen pressure. When the oxygen pressure increased from 0.01 Pa to 0.52 Pa, the optical band gap of the WO_x prepared also increased from 1.56 eV to 3.18 eV. The fabrication of WO_x in this work had an oxygen pressure of 1.0 Pa, being different from those reported in the literature, which also belonged to a comparable thin film deposition technology under low oxygen pressure. The optical band gap of 2.10 eV for VO_x obtained from the same method is basically similar to that of 2.17 eV for VO_x thin film obtained by sputtering by Zhenfei Luo *et al.*[101] It could be seen from these results that the optical band gap of the oxide was affected by the structural characteristics of the film, the preparation conditions, and the content of elements inside the film.

3.2.5 Electrical characteristics of MoO_x and WO_x

As seen in Figure 3.10, the HWOSD method was used to fabricate a TMO film with a certain thickness on a glass substrate, and a grid electrode was prepared by thermal evaporation on the surface of such films, for testing electrical conductivity. Their conductivity σ (with the unit of S/cm) was obtained by equation (3), with the corresponding current value when applying the electrical potential between the two electrodes:.

$$\sigma = \frac{I*L_1}{U*d*L_2} \quad (3.3)$$

Where d (cm) is the thickness of the film material; U is the voltage (V),; I is the current (A),; L_1 and L_2 (cm) are the electrode spacing width and electrode length, as show in Figure 3.9.The conductivity obtained for MoO_x and WO_x film were 2.58×10^{-6} and 5.14×10^{-7} S/cm, respectively.

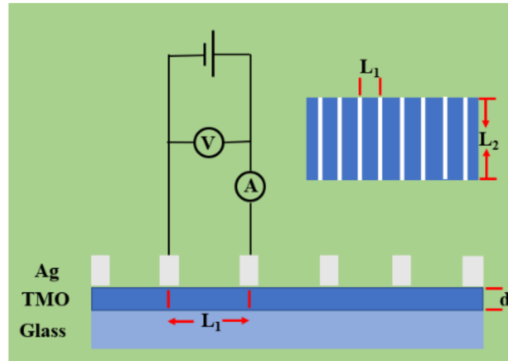

Figure. 3.9 Schematic diagram of transition metal oxide conductivity measurement.

The surface potential of MoO_x and WO_x on polished silicon wafers was measured by Kelvin Probe Microscopy (KPM), and the energy band relationship at the interface between the transition oxides and the silicon wafer was qualitatively analyzed. The measurement results are shown in Figure 3.10.

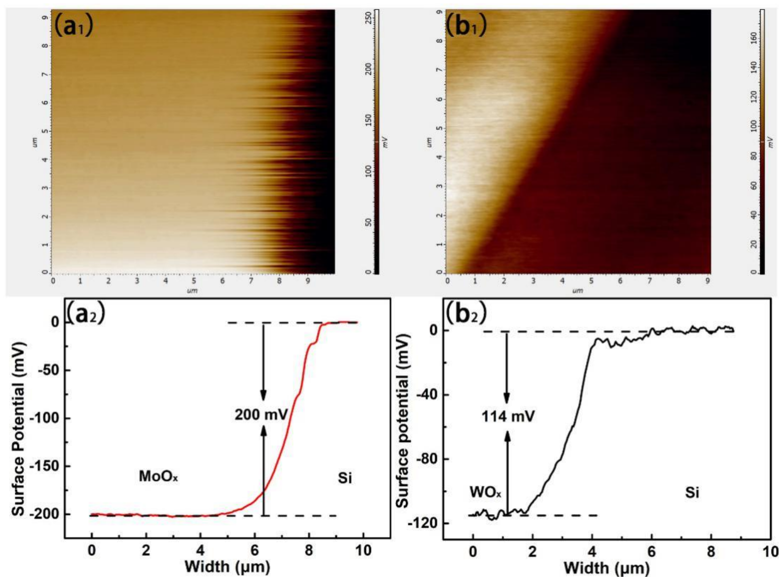

Figure 3.10 (a_1) Potential distribution of MoO_x film on silicon wafer surface. (a_2) The surface potential difference between MoO_x and silicon in the z-axis direction. (b_1) The potential distribution of WO_x film on silicon wafer surface. (b_2) The surface potential difference between WO_x and silicon in the z-axis direction.

The working principle of the Kelvin probe microscope is: when two different samples are in contact, the Fermi level will be in the same position at the contact interface. But due to the different work functions of the materials, the energy bands are bended at the interface, leading to the redistribution of different charges that generates forces with the probes of the device. It was such tested forces that provided us the surface potential and the work function of the materials.

Different potential distributions between MoO_x and n-Si are illustrated in Figure 3.10 (a_1), according to the brightness and darkness of the colors. Figure 3.10 (a_2) stands for the potential value on the Z axis obtained from Figure 3.10 (a_1). It can be seen that the potential on the MoO_x side is about 200 mV lower than those on the Si plate side. It showed that higher work function and lower Fermi level of MoO_x than those of n-Si resulted in redistribution of surface charges and therefore the bending of their energy bands at interfaces, building up potential barrier for electron transport, while benefiting the selective hole transport when they moved towards MoO_x side based on the attraction from MoO_x's work functions.

The potential distribution of the WO_x film in contact with the Si wafer is shown in Figure 3.10 (b_1), which followed similar mechanisms to the interactions between MoO_x and Si wafers. While Figure 3.10 (b_2) similarly presents the contact potential difference between WO_x and Si in the Z-axis direction. Comparing Figure 3.10 (a_2) and (b_2), the contact potential difference of MoO_x (200 mV) was found significantly higher than that of WO_x (114 mV), which could be inferred that the MoO_x film might cause a greater band bending. The different work functions of 6.9 eV for MoO_x and 6.5 eV for WO_x, respectively, could be the right reason for causing the difference in the bending of crystalline silicon band.

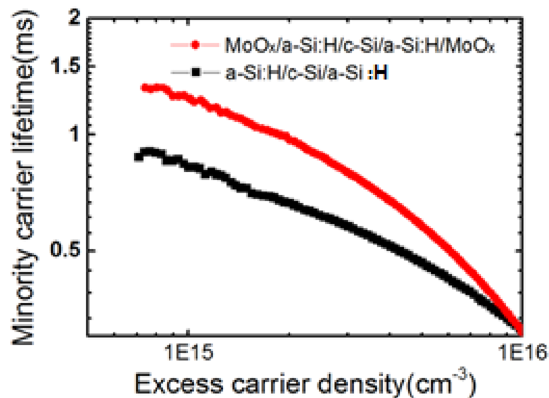

Figure 3.11 Measured effective lifetimes for samples with the structures of i a-Si:H/c-Si/i a-Si:H and MoO_x/i a-Si:H/c-Si/i a-Si:H/MoO_x as a function of excess carrier density in the range of 7×10^{14} cm^{-3} ~ 1×10^{16} cm^{-3}.

Figure3.11 shows the curve of minority carrier's lifetime with carrier concentration in n-type CZ silicon wafers with i a-Si:H or MoO_x/i a-Si:H composite layers deposited on both sides. Compared with the passivation of amorphous silicon, the symmetric structure of i: a-Si/MoO_x(14 nm) covered on both sides of the silicon wafer causes a longer minority lifetime in their injection concentration range of 7×10^{14} cm^{-3}~1×10^{16} cm^{-3}, with 1.3 ms as the highest for MoO_x/i a-Si:H/c-Si/i a-Si:H/MoO_x can reach. This indicated that MoO_x had a strong field passivation effect on silicon wafers, that is, a larger work function of the MoO_x film could cause a larger band bending at the contact interface with the Si wafer, thereby reducing the recombination of carriers near the contact. Such results could be also corroborated with the test result of the contact potential of the front surface.

3.3 Effect of Annealing on optical and structural properties of TMO thin films

Considering that the TMO films may suffer the temperature changes when being applied into devices and future possible optimizations on their film properties, the effect of annealing temperature on MoO_x and WO_x films were studied. The two thin film materials deposited on the glass substrate were rapidly annealed at different temperatures using a fast annealing apparatus. The morphology, transmittance, and structure of the thin films were performed by means of optical microscope, UV-VIS absorption and XRD methods.

First, under the protection of argon, the molybdenum oxide film was rapidly annealed at 200, 400, 450, 500, 600, 650, 700, and 800 °C, respectively for 60 seconds. The morphology, transmittance and XRD pattern of the films are shown in Figure 3.13.

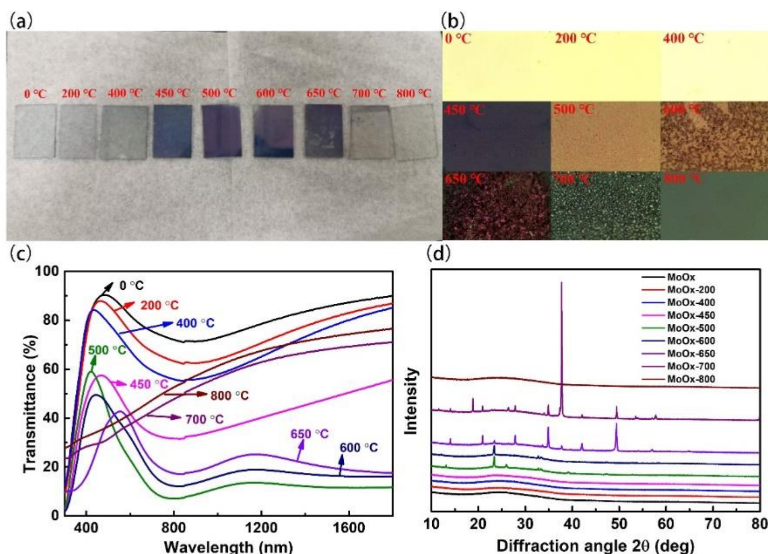

Figure 3.12 Photos (a), optical images (b), transmittance (c), and XRD diffractograms of MoO_x films at different rapid-annealing temperatures.

As can be seen from Figure 3.12 (a) and (b), when the annealing temperature was less than 400 °C, the appearance of the MoO_x film had no obvious changes. As the annealing temperature increased from 450 to 600 °C, films' color gradually deepened, and the metallographic microscope showed that the MoO_x films gradually appeared granular, implying some structural changes. Further increased the annealing temperature led to disappearance of the MoO_x film from the substrates. When the annealing temperature reaches 800 °C, the granular MoO_x was completely disappeared.

Figure 3.12 (c) shows the transmittance of MoO_x at different rapid annealing temperatures. With the annealing temperature increased, the transmittance of the MoO_x film as a whole decreased firstly and then increased. When the annealing temperature was raised from 200 to 500 °C, the transmittance of the film drops to a minimum, a possible reason was that the structure change of the MoO_x film affected its transmittance to some extent. When the rapid-annealing temperature continued to rise, the film's transmission rate rose continuously because the higher annealing temperature might cause the decomposition or sublimation of MoO_x film exposing the glass substrate, thereby increasing the transmission rate.

From the XRD pattern of Figure 3.12 (d), it can be seen that when the annealing temperature was < 450 °C, the structure of the MoO_x film remained unchanged, still being amorphous. When the rapid-annealing temperature rose to 500 °C, the XRD pattern of MoO_x presented diffraction peaks at 13.04°, 23.38°, 25.94° , 39.13°, 47.35°, 52.77°, 39.13°, 47.23°, 52.76°, respectively, corresponding to crystal planes of (0 0 1), (1 0 0), (0 0 2), (0 0 3), (2 0 0), (1 0 -4), and (2 1 0) for MoO_3 monoclinic phase[74]. When the annealing temperature was 600 °C, the disappearance of characteristic diffraction peaks at 13.04°, 25.94°, 39.13° revealed the vanish of (0 0 1), (0 0 2), and (0 0 3) crystal planes. When increasing the annealing temperature to 650 °C, the characteristic peak at 23.38° was found much less pronounced, and the one characteristic peak at 32.65° disappeared, meanwhile generation of new diffraction peaks at 13.88°, 20.88°, 27.88° suggested newly formed (6 4 0), (10 4 0), and (6 6 1) crystal planes of $MoO_{2.8}$. And the ones at 34.89°, 37.69° proved the presence of (1 -2 7) (3 -2 4) crystal planes of Mo_9O_{26}. while the one at 57.01° stood for the (14 1 1) crystal plane of Mo_4O_{11}[102, 103]. Continued to increase the temperature to 700 °C, the crystal plane of (3 -2 4) for Mo_9O_{26} claimed the preferred crystal orientation, corresponding to peak at 37.66°, accompanied by a peak at 18.74° exhibiting (-4 0 1) crystal plane of Mo_4O_{11}[104]. In summary, as the annealing temperature was risen, the amorphous MoO_x film generated monoclinic MoO_3 crystals at 500 and 600 °C, as the temperature continues to rise to 650 and 700 ° C, $MoO_{2.8}$, Mo_9O_{26}, and Mo_4O_{11} appeared, it could be seen that the oxygen element in the MoO_x film had a tendency to detach from the film. Literature showed that the reduction of x in MoO_x might cause the decrease of work function of the MoO_x film. When it continues to increase to 800 °C, the MoO_x thin film in the glass had completely decomposed and escaped the glass substrate, as shown in Figure 3.12 (a).

Using the same method and process, the rapid annealing performance of WO_x film was studied, as shown in Figure 3.13. It was seen from Figure 3.13 (a) that rapid annealing gradually changed the color of the WO_x film from light to dark. Figure 3.13 (b) confirmed agglomeration phenomenon at some positions of the WO_x film as the annealing temperature gradually raised up to 600 °C. When the annealing temperature was further increased to 800 °C, the WO_x film had partially peeled off. The position of the film was seen as "wrinkle", suggesting that a stress change inside the film。

Figure 3.13 (c) shows the effect of different annealing temperatures on the transmittance of the WO_x films. With the rapid-annealing temperature increased, the transmittance of the WO_x film gradually decreased, implying that it might cause the structural changes of the WO_x film. As can be seen from Figure 3.13 (d)， when the temperature lied in between 200 and 400 °C, the WO_x film still maintained an amorphous state. When the rapid- annealing temperature was rose to 600 °C, peaks of diffraction at 23.96°, 34.08°, 42.11°, 49.04°, 55.25°, and 61.07°, respectively,

corresponding to (1 0 0), (1 1 0), (1 1 1), (2 1 0), (2 1 0), and (2 1 1) crystal planes[105]. Continued to raise the annealing temperature to 800 °C, the characteristic peaks at 23.72° , 33.60° , 41.32° , 44.68° , 48.03° , 54.15° , 59.75° , and 70.04° , were recognized as crystal planes of (1 1 0), (2 0 0), (2 0 1), (2 1 1), (2 2 0), (3 1 0), (3 1 1), and (4 0 0) for $WO_{2.9}$[106]. When the annealing temperature reached 800 °C, the phenomenon of X reduction in WO_x was also found.

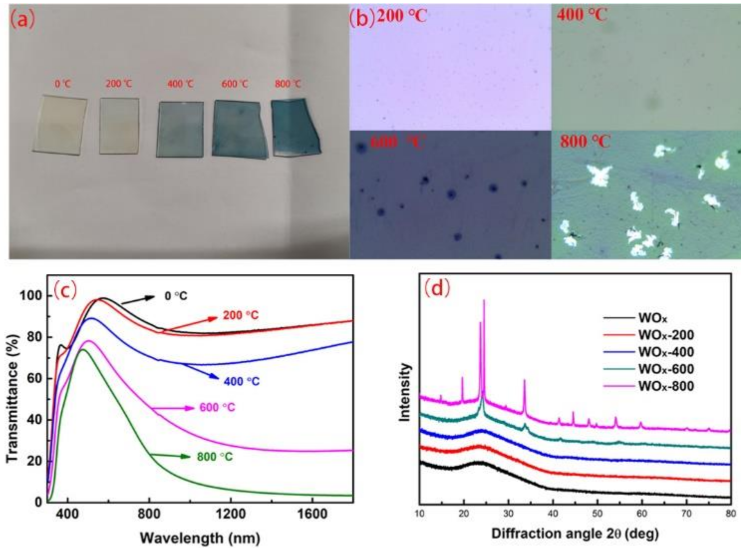

Figure 3.13 Photos (a), morphology under optical microscope (b), transmittance(c), and XRD pattern (d) of WO_x films at different rapid annealing temperature.

3.4 Summary

This chapter introduced the working principle of the HWOSD method, the optimization of the transition metal oxide process, and the material characteristics of the transition metal oxide. The following conclusions are obtained:

(1) In the fabrication process of MoO_x, WO_x, and VO_x, the hot-wire temperature and oxygen pressure were important process parameters: the optimal working temperature of molybdenum wire was about 1050 °C, tungsten wire was 1200 ℃, vanadium wire and tungsten wire similar. The optimal oxygen pressure was 0.2 Pa for molybdenum oxide and 1.0 Pa for Tungsten oxide was.

(2) After analyzing the characteristic of MoO_x, WO_x, and VO_x films fabricated under optimal conditions, HWOSD method for fabricating amorphous TMO film materials

with smooth surface, same thickness realizing a "conformal" deposition. The XPS was used to characterize the transition metal oxide (TMO): x in MoO_x was 2.94. Similarly, x for WO_x was 2.91, and x in VO_x was 2.32. The optical band gaps of MoO_x, WO_x, and VO_x were 2.67, 1.86, and 2.19 eV, respectively. The electrical conductivity of MoO_x was 2.58×10^{-6} S/cm, and that of WO_x film was 5.14×10^{-7} S/cm. Using KPM to measure the contact potential of both MoO_x and WO_x with silicon, contact potential of 200 mV for MoO_x and 114mV for WO_x was obtained. MoO_x had a field passivation effect for silicon wafers with i:a-Si/c-Si/i:a-Si structure, which could further increase the minority carrier lifetime of this structure to 1.3 ms.

Annealing of MoO_x and WO_x realized their phase transition from amorphous state to a polycrystalline state, with changes on their optical transmittance in the visible light region.

Above all, the TMOs fabricated by HWOSD method proved good material properties and showed their excellent potential in the preparation of photovoltaic devices. Taking all these into consideration, we would focus on the application of MoO_x as a carrier selection layer in new silicon heterojunction solar cells in the subsequent work.

Chapter 4. Optimization of henterojunction solar cell with MoO_x, WO_x, and VO_x

Based on the optimization of the material properties of MoO_x, WO_x, and VO_x fabricated by HWOSD, they were used as HTLs for preparation of the novel silicon heterojunction solar cells. MoO_x thin films as HTL were investigated from five aspects, including (1) the effect of passivation layer on the performance of new heterojunction solar cells; (2) the influence of MoO_x film thickness on device performance; (3) the effect of different annealing processes on the device performance; (4) performance comparison of heterojunction solar cells with MoO_x, WO_x, and VO_x as HTLs; (5) The application of MoO_x and WO_x in a new lithography-free and dopant-free back-contact silicon heterojunction solar cell.

In this chapter, by optimizing the device parameters, the 21.10% power conversion efficiency of a novel heterojunction solar cell was obtained with the structure of Ag/ITO/n+ a-Si:H/ i a-Si:H/c-Si/i a-Si:H/MoO_x/Ag. The power conversion efficiency of lithography-free and dopant-free back-contact heterojunction solar cells reached 20.24% with MoO_x as HTL and TiO_2 as ETL.

4.1 Optimization of novel silicon heterojunction solar cells with MoO_x as HTL

The performance of the novel silicon heterojunction solar cells (SHJs) with MoO_x as HTL were optimized based on three aspects: interface passivation layer, MoO_x thickness, and annealing process. The influence of process conditions on the device performance was analyzed in detail.

For SHJs, passivation layer at their interface can effectively improve the interface quality and their performance. However, the current use of high-quality passivation layer technology also often means further complexity of the device manufacturing process. Therefore, the development of passivation layer technology with simple process, low cost, and excellent performance has always been the focus of researchers.

In order to determine the role of interface passivation layer on the performance of SHJs with MoO_x as HTL, planar SHJs on polished silicon wafer were studied firstly, prior to those on the textured one, which can be integrated into industrialization.

As a start, a planar silicon heterojunction solar cell without passivation layer was prepared, whose structure and fabrication process are shown in Figure 4.1. The substrate of the planar silicon heterojunction solar cell was n-type polished silicon wafer. On the hole transport side, MoO_x prepared by HWOSD directly contacted with the crystalline silicon substrate, and followed with ITO and Ag gate lines; On the electron transport side, Al electrodes were prepared by thermal evaporation contacts with the substrate.

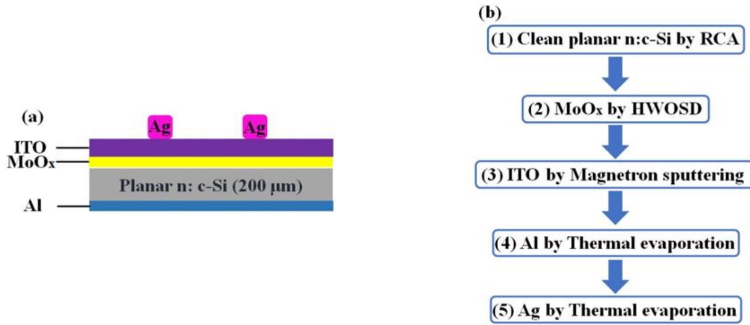

Figure 4.1 *(a)Cross-sectional of the novel planar heterojunction solar cell with MoO_x as HTL. (b) Process flow chart for the fabrication of the novel planar heterojunction solar cell with MoO_x as HTL.*

No matter what measures were taken to optimize the wafer cleaning process and MoO_x thickness, the V_{OC} of silicon heterojunction solar cells without passivation layer could not exceed 385 mV (the optimized MoO_x thickness was 20 nm). Although the performance of the device was affected by the use of Al only in the electron transport layer, the main affecting factor was from the contact interface between MoO_x and Si with lots of defect states, resulting in strong carrier recombination loss. Therefore, a good interface passivation layer is important to improve the device performance.

According to the literature reports, i a-Si:H and SiO_x were the high-performance passivation layers at the interface between MoO_x and Si. SiO_x could be obtained by thermal oxidation and UV-O_3 oxidation, which had a low-cost characteristic. Corsin Battaglia *et al*.[63] reported that adding i a-Si:H between MoO_x and Si could effectively improve the V_{OC} and PCE of the device. Dongyun Chen *et al.*[82] studied the effect of SiO_x passivation layer on the contact interface between MoO_x and Si. As a passivation layer, i a-Si:H fabricated by PECVD technology had been widely used in conventional SHJ cells with excellent passivation effect. At present, the highest efficiency SHJ cells are based on the high-efficiency passivation of intrinsic amorphous silicon. Therefore, we will directly apply it in the following textured substrate solar cells. Here, we mainly focus on the passivation effect of SiO_x thin films, and hope to realize the fabrication of SiO_x thin films by simple and rapid process. By

studying the passivation effect of SiO_x thin films prepared by UV-O_3 technology, we could guide the optimization direction of subsequent textured substrate cells. UV-O_3 treatment could quickly form SiO_x passivation layer on the surface of Si wafer, which was fast, low cost, and easy operation. Previous works in our group showed that the effective passivation of the contact interface could be achieved by adding SiO_x (treated by UV-O_3) between Si and ETLs (like SnO_2, TiO_2, etc.). Therefore, we have been very interested in the passivation effect inserting such UV-O_3 treated SiO_x between MoO_x and Si, via systematically studying the time dependency of different UV-O_3 treatment on the performance of those novel SHJ solar cells. The structural diagram and preparation flow chart of the device are shown in Figure 4.2.

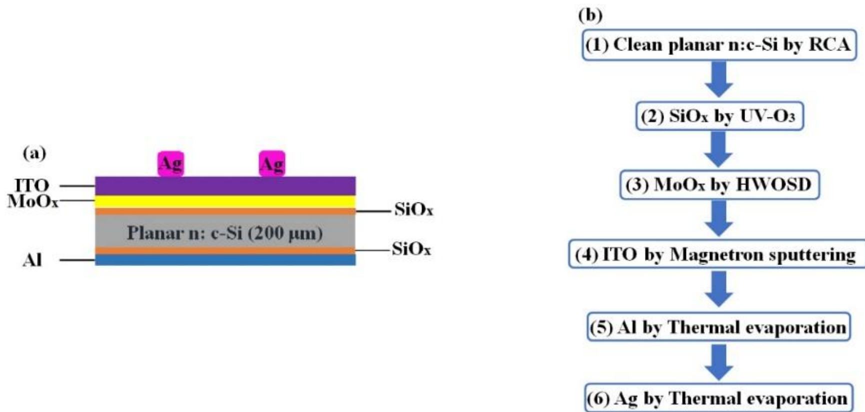

Figure 4.2 (a) Cross-sectional of the novel planar heterojunction solar cell with SiO_x as passivation layer. (b) Process flow chart for the fabrication of the novel planar heterojunction solar cell with SiO_x as passivation layer.

In the process of device fabrication, the thickness of SiO_x on the surface of Si wafer was controlled by the treatment time of UV-O_3, then the passivation layers of front surface (at the interface between MoO_x and Si) and rear surface (at the interface between Si and back electrode) were optimized. The effect of UV-O_3 treatment time on V_{OC} was investigated. While optimizing the front SiO_x, the thickness of MoO_x was kept at 20 nm, and the treatment time of UV-O_3 on the rear surface was fixed for 2 min. The treatment time of UV-O_3 on the front surface was therefore the sole variable, which were 0, 2, 4, 6, and 8 min, respectively. The results of devices are shown in Figure 4.3 (a). On the basis of the optimal parameters for passivation of the front surface, a similar method was used in parallel to optimize the passivation layer (SiO_x) of the rear surface. The treatment time of the rear surface are 2, 5, 8, 11, and 14 min, respectively. The results are shown in Figure 4.3 (b). Compared with the solar cell without passivation layer, the V_{OC} of the solar cells with SiO_x passivation layer were

significantly increased, which indicated that the SiO_x thin film fabricated by UV-O_3 technology could play a passivation role. For the optimization of SiO_x (between MoO_x and Si), as the UV-O_3 treatment time went on, the V_{OC} of the solar cells increased and then fell, and the best/optimized passivation effect time was 2 min., which could be widely applied for the subsequent textured solar cells optimization. However, for the rear surface of the devices (between Al and Si), the change of UV-O_3 treatment time had shown little effects on the solar cell's V_{OC}.

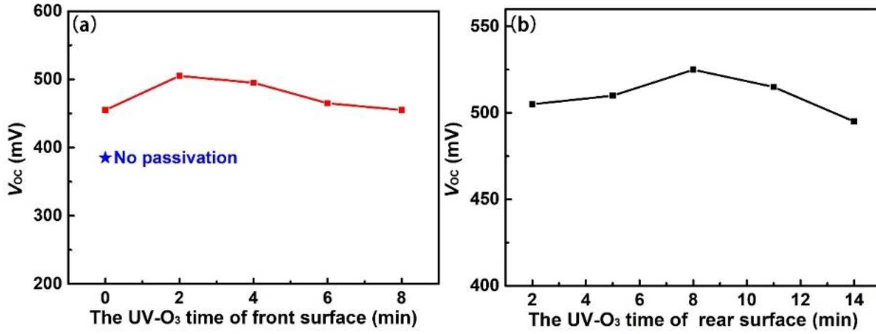

Figure 4.3 (a) The Effect of UV-O_3 treatment time of front surface on V_{OC}. (b) The effect of UV-O_3 treatment time of rear surface on V_{OC}.

Obviously, the performances of solar cells were limited because of the simple structure of the above planar cells. Moreover, the research work of J. Geissbuhler and D. Sacchetto showed that the sputtering process of ITO thin films might cause the decrease of the work function of MoO_x thin films, which would have adverse effects on the performance of devices[42,67]. Based on the above situation, in order to study the role of MoO_x thin film as HTL, the structure of the solar cells were designed as Ag/ITO/n+ a-Si/i a-Si:H/textured n-type Si/passivation layer/MoO_x/Ag, which were compatible with SHJ solar cells from industrial production lines. The structural diagram of the device is displayed in Figure 4.4 (a). The advantages of such structure are as follows: (1) it can effectively avoid the "bombardment" of the plasma on MoO_x during the process of ITO sputtering, and can avoid the work function attenuation of MoO_x films caused by direct contact with ITO; (2) the role of MoO_x thin film as HTL in the novel SHJ solar cells can be discussed more pertinently; (3) because the cell structure can achieve good compatibility with the current industrial heterojunction solar cell production line, it can greatly reduce the difficulty of industrialization promotion of this kind of novel SHJ solar cell.

The fabrication process of novel SHJ solar cells based on textured substrates was as follows: n-type <100> CZ silicon wafers (thickness 200 μ m, resistivity 1-5 Ω· cm)

were used as substrates, the random pyramid surface texture was obtained by alkaline etching, and the pyramid tip was slowed down by isotropic corrosion. After RCA cleaning, the silicon wafers were immersed in 2% hydrofluoric acid for 1 min to remove the surface oxide layer.

All SHJ solar cells (the electron selective transport side was Ag/ITO/n+ a-Si/i a-Si:H) were fabricated by the same process. Firstly, 7 nm intrinsic amorphous silicon passivation layer and 10 nm n-type heavily doped amorphous silicon electron transport layer were fabricated by plasma enhanced chemical vapor deposition (PECVD), then ITO films with thickness of about 80 nm were fabricated by magnetron sputtering, and silver gate wire electrodes were prepared by thermal evaporation.

The back-light structure of SHJ solar cells was the Ag/MoO_x/passivation layer. Three kinds of passivation layers were compared, including intrinsic amorphous silicon fabricated by PECVD, SiO_x fabricated by UV-O_3 treatment, and i a-Si:H/SiO_x bilayers fabricated by PECVD and then treated by UV-O_3. After the passivation layer was made, MoO_x thin films were fabricated by HWOSD. MoO_x films with different thickness were deposited by adjusting the deposition time. Finally, the silver film was prepared by thermal evaporation as the electrode. The preparation flow chart of the device is illustrated in Figure 4.4 (b).

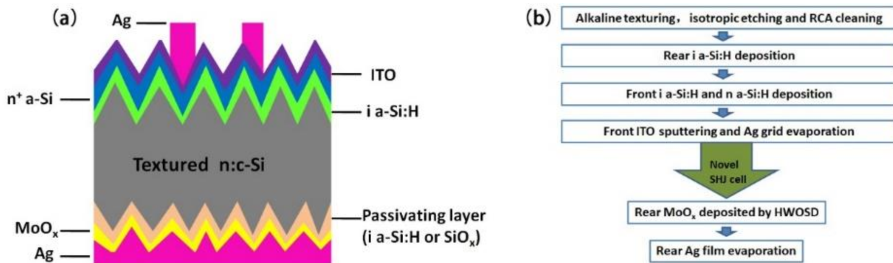

Figure 4.4 (a) The cross-section schematic of the novel heterojunction silicon solar cell with MoO_x. (b) Process flow chart for the fabrication of the novel heterojunction silicon solar cell.

Figure 4.5 shows the *J-V* curves of SHJ solar cells with MoO_x, SiO_x/MoO_x, i a-Si:H/MoO_x, and i a Si:H/SiO_x/MoO_x as the passivation layer. Their device parameters are shown in table 4.1. At this time, the thickness of MoO_x was 20nm (being optimized in planar heterojunction cell). For the SHJ cells with their rear structure having direct contact between MoO_x and Si (without passivation layer), when their front surface adopted the optimized structure from conventional crystalline SHJ cells, their performance did have been improved (with a V_{OC} of 549.7 mV and an PCE of 14.09%),

in comparison with those planar heterojunction solar cell with simplified structure shown in Figure 4.1 (V_{OC} was 385mV). However, such performance is still far lower than that of conventional SHJ solar cells, due to a serious recombination loss of photo-generated carriers at the interface between MoO_x and Si.

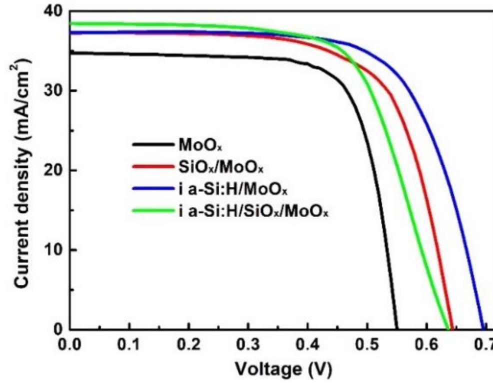

Figure 4.5 Current density-voltage (J-V) characteristics of silicon heterojunction solar cells having MoO_x (20nm) hole selective transport layer with different passivation layers.

Table 4.1 *The characteristic parameters of MoO_x-based SHJ solar cells with the different passivation layers*

Passivation layer	V_{oc} (mV)	J_{sc} (mA/cm^2)	FF (%)	PCE (%)	Rs (Ω)
--	549.7	34.18	74.96	14.09	2.3
SiO_x	643.5	36.88	70.54	16.74	3.1
a-Si	690.2	36.72	70.35	17.83	4.5
a-Si/SiO_x	625.0	38.50	67.23	16.17	7.6

Note: the thickness of MoO_x in this series of solar cells was 20 nm.

The *J-V* curve of silicon heterojunction solar cell with SiO_x/MoO_x as rear structure obtained by UV-O_3 treatment for 2 min (the optimized time of UV-O_3 treatment determined by planar solar cells) is the red curve in Figure 4.5. It can be seen from table 4.1 that the V_{OC} of the solar cell was greatly increased from 549.7 mV without interface passivation layer to 643.5 mV when passivated by SiO_x, and the PCE of the solar cell reached 16.74%. Because UV-O_3 treatment was carried out at room temperature, only a thin SiO_x passivation layer was formed on the surface of crystalline silicon. The device performance showed that the passivation layer had a

good passivation effect on the "dangling bond" on the surface of textured crystalline silicon with pyramid structure. In addition, the passivation of the interface would also change the electrostatic potential of the interface, enhancing the carriers-collection ability of solar cells. The performance of J_{SC} increased from 34.18 to 36.88 mA/cm^2. This pronounces a certain potential for developing such rapid passivation technology using SiO_x via UV-O_3 treatment.

The V_{OC} of solar cells with amorphous silicon as passivation layer (blue curve in Figure 4.5) reached 690.2 mV, revealing better passivation effect compared with SiO_x passivation layer by UV-O_3 treatment, while the J_{SC} and FF were close to those of SiO_x passivated solar cells, and the power conversion efficiency reached 17.83%.

The above analyses show that i a-Si:H and SiO_x have good passivation effect on MoO_x/Si interface. In previous research on electron transport layer from our team, the i a-Si:H/SiO_x bilayer passivation layer had excellent passivation effect on ETL/Si interface[107]. Therefore, the i a-Si:H/SiO_x bilayer passivation layer was fabricated by UV-O_3 after passivation of i a-Si:H. However, the results showed that the V_{OC} (625 mV), FF (67.23%), and Eff (16.17%) of the solar cell were all lower than those of cells using passivation layer alone, while only J_{SC} (38.50 mA/cm^2) was slightly increased (see green curve in Figure 4.5 and table 4.1). One of the reasons may be the loose structure of i a-Si:H passivation layer. In the process of UV-O_3 treatment, O atoms diffused into i a-Si:H and formed a thick SiO_x layer which may destroy the passivation effect of i a-Si:H, and cause larger series resistance (R_s) (table 4.1) which was not conducive to carrier collection. However, the i a-Si:H/SiO_x played a role in improving the performance of solar cell's interface passivation with SnO_x and other ETL[107], which implied that the destroyed passivation effect from oxygen diffusion might not be the main factor. On the other hand, a dipole may be formed due to the diffusion of O atoms at the SiO_x/MoO_x interface, which was directed from MoO_x to SiO_x[108]. This would hinder the hole transport and reduce the selection of MoO_x as HTL for holes, thus the performance of the device decreased. However, in the solar cell with SnO_x as ETL, the direction of the dipole field is also from TMO to SiO_x, which is different from the blocking effect on the hole. This direction is beneficial to the electron transport, so it is conducive to the improvement of device performance. This may be the reason why the i a-Si: H/SiO_x bilayer passivation layer exhibited different effects in the different kinds of solar cells. For exploring the specific role of dipole in HTL and ETL, further research is needed.

In conclusion, i a-Si:H presented the best passivation effect on MoO_x/Si interface. As a low-cost rapid passivation technology, the UV-O_3 treatment of crystalline silicon surface for SiO_x formation has a great potential, but the passivation effect of i a-Si/SiO_x bilayer passivation layer is not as good as that of a-Si or SiO_x passivation layer alone. Therefore, when using i a-Si:H as passivation layer, the formation of SiO_x layer

on the surface of i a-Si:H should be avoided as far as possible, which provides a guidance for the subsequent optimization of device performance.

After the optimization of the passivation layer, the thickness of MoO_x was further optimized by using i a Si:H as passivation layer. Although we have preliminarily optimized the thickness of MoO_x thin film on planar structured solar cells, due to the simplicity device structure and some other factors, the optimization results may not be suitable for the textured-substrate structure, requiring systematic optimization. Under the optimal fabrication conditions of MoO_x thin films, a series of silicon heterojunction solar cells with MoO_x hole selection layer thickness of 10, 14, 29, 55, and 71 nm were fabricated by changing the deposition time of MoO_x. The variation of *J-V* parameters of this series of devices is shown in Figure 4.6., showing a fluctuated performance of the devices with the increase of MoO_x thickness from 10 to 71 nm.

When the thickness of MoO_x was increased from 10 to 14 nm, the V_{OC} of solar cells rose up from 683.6 to 697.1 mV. With further increase of MoO_x thickness, V_{OC} declined gradually to 675.8 mV when the thickness reached 71 nm. When the MoO_x thickness is as low as10nm, the V_{OC} became lower which might be due to the space charge region near the surface of silicon had not been formed well. However, when the MoO_x film was too thick, the V_{OC} still decreased probably due to the decrease of collection efficiency caused by the enhanced recombination of carriers in thicker films, which was also reflected in the rapid decrease of J_{SC}. Meanwhile, the change of FF was affected by band structure and series resistance. When the thickness of MoO_x was 10 nm, the poorly established space charge region was not conducive to the effective separation and collection of carriers, so the filling factor was as low as 67.02%. When the thickness of MoO_x lied in between 14 and 55 nm, the space charge region was well established with little changes on series resistance. Therefore, FF remained relatively unchanged. When MoO_x film was thick (71nm), Rs increased greatly and FF decreased dramatically. Based on the results above, the optimal thickness of 14 nm for MoO_x film has been concluded, where MoO_x with high work function could not only promote the establishment of effective space charge area on the surface of crystalline silicon, but also avoided the additional recombination effect caused by too thick layer of MoO_x, resulting the power conversion efficiency of 18.11% for such type SHJ solar cells.

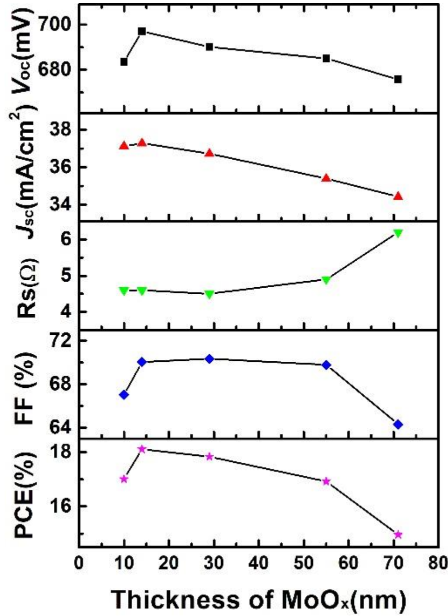

Figure 4.6 Effect of MoO_x thickness on performance of novel heterojunction solar cells.

As a post-treatment on SHJ cells, annealing is a common technology for which can improve the contact resistance between the metal electrode and its adjacent layers, reduce the square resistance of ITO, and promote the collection and transportation of carriers. Especially in the traditional heterojunction solar cells, it can repair the sputtering damage of a-Si film from the process of ITO fabrication to a certain extent, reduce the density of defect states in a-Si thin film, and then improve their performance. However, for the silicon heterojunction solar cells with MoO_x as HTL, Jonas Geissbuhler *et al.*[42] have shown that the annealing process could result in an *S*-shape for the *J-V* curve from the formation of a barrier at the MoO_x/TCO interface to hinder the passage of holes during annealing. Davide Sacchetto *et al.*[67] studied the annealing behavior of SHJ solar cells with MoO_x as HTLs, and concluded that the degradation and the decrease of work function induced by annealing were the main reasons for their declined performance.

In order to further improve the performance of silicon heterojunction solar cells, the different annealing process of heterojunction solar cells with MoO_x as HTL were carried out. Considering that annealing process may affect MoO_x film, electrode contact, and interface, four kinds of annealing process were performed and compared.

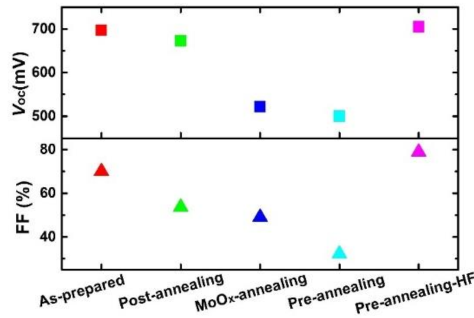

Figure 4.7 Influence of annealing process on V_{OC} and FF of the SHJ solar cells with MoO_x as HTL.

Figure 4.7 compares the effects of different annealing processes on V_{OC} and FF of SHJ solar cells with MoO_x as HTL. As a reference, the performance of as-prepared heterojunction solar cells are also presented here. Post-annealing refers to annealing at 190 °C for 5 min after the device fabrication. Similar to the results reported in the literature, the performance (V_{OC} and FF) of the solar cells was significantly lower than those of as-prepared ones, which could be mainly attributed into element diffusion caused by annealing.

In order to further explore the effect of annealing on device performance, the MoO_x-annealing process was designed and carried out prior to preparation of the silver electrode on the back of the solar cell (when the devices had not been completed). The annealing temperature was still 190 °C and the time was 5 min. MoO_x-annealing process eliminated the effect of annealing on the Ag/MoO_x interface, while the MoO_x film was completely exposed. If their declined performance was due to the changes of either the MoO_x layer itself or their interface layer between MoO_x layer and silicon, the annealing must have aggravated the decline of device performance. It was found that the V_{OC} and FF of the solar cells were further reduced compared with that of the post-annealed samples, which indicated that the annealing process did have a destructive effect on the exposed MoO_x layer or the interface between it and crystalline silicon.

To avoid the influence of annealing process on the MoO_x film itself, the pre-annealing was performed prior to the fabrication of MoO_x film. However, the performance of solar cells was still not improved and FF had been significantly reduced. This phenomenon indicated that the damage to the device performance by annealing may not be mainly due to the changes of MoO_x film itself. The passivation layer of a-Si film was exposed to the annealing atmosphere under the condition of pre-annealing. Combined with the previous research on the passivation layer, we speculate that the

reason for the further deterioration of the device performance might be due to the formation of a-Si/SiO_x bilayer by oxidation of the intrinsic amorphous silicon passivation layer in air, which leads to poor interface passivation effect. It could be both the large series resistance caused by SiO_x layer and the dipole at MoO_x/SiO_x interface that affect the selective transportation of MoO_x to holes.

In order to verify our conjecture, we further improved the annealing process and designed the pre-annealing-HF process. In other words, the annealing was still carried out before the fabrication of MoO_x film, but the MoO_x film was not deposited immediately after annealing. Instead, the amorphous silicon surface on the back of the solar cell was rinsed with HF to remove the SiO_x that may be formed during the annealing process, and then the MoO_x layer and Ag electrode were fabricated. It can be seen from Figure 4.7 that the performance of the device has been significantly improved by the pre-annealing-HF process, which indicates that SiO_x generated on the surface of i a-Si:H after annealing was indeed the main reason affecting the device performance. Therefore, it is necessary to avoid the formation of SiO_x layer at i a Si:H/MoO_x interface due to annealing during the fabrication of novel heterojunction solar cells with MoO_x as HTL.

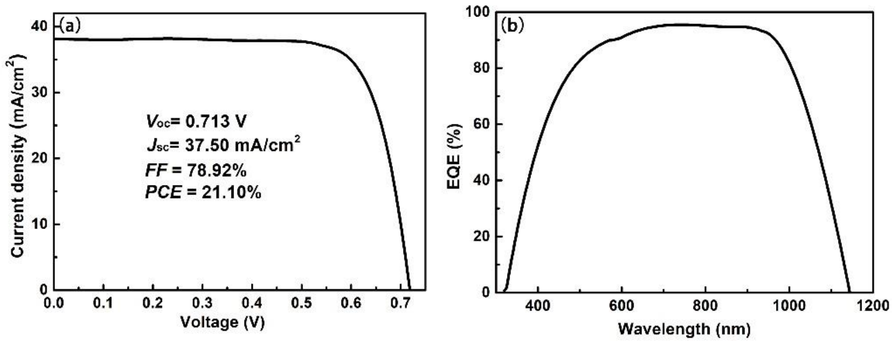

Figure 4.8 The J–V (a) and EQE characteristic of a champion SHJ solar cell with MoO_x as HTL.

Figure 4.8 (a) shows the *J-V* curve of the solar cell with MoO_x as HTL with the highest photoelectric conversion efficiency obtained by the pre-annealing-HF process. At this time, the V_{OC} of 713 mV, J_{SC} of 37.50 mA/cm^2, and FF of 78.92%, and therefore final PCE of 21.10% were obtained. Figure 4.8 (b) shows the EQE curve of the solar cell, whose photoelectric current density was obtained by integrating the EQE curve as 37.20 mA/cm^2, being basically consistent with the measured value of 37.50 mA/cm^2 of J_{SC}.

4.2 The performance comparison among the SHJ solar cells with MoO_x, WO_x, and VO_x as HTLs

On the basis of optimizing the structure and processing conditions of a novel SHJ solar cell with MoO_x as HTLs, their performance with WO_x and VO_x as HTLs were investigated, whose passivation layer between TMO and Si had been the *i a-Si:H* film via pre-annealing-HF process.

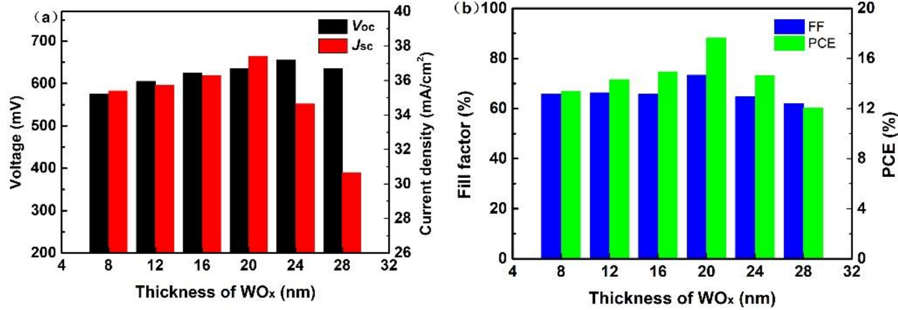

Figure 4.9 Influence of WO_x thickness on V_{OC} and J_{SC} of (a) and FF and PCE (b) the SHJ solar cells with WO_x as HTL.

For the heterojunction cells with WO_x as HTL, WO_x thin films were fabricated by the optimized processing conditions obtained in the previous chapter. By controlling the deposition time of WO_x, the SHJ solar cells with WO_x thickness of 8, 12, 16, 20, 24, and 28 nm were obtained respectively. The performance parameters were shown in Figure 4.9. When the WO_x thickness increased from 8 to 24 nm, the V_{OC} was raised from 575 to 655 mV. This showed that with the increasing thickness of WO_x film, the band bending of crystalline silicon at the interface increased gradually, making the space charge region widened and therefore causing the increase of built-in potential. The ability of separating different carriers of the device would be further enhanced, and the V_{OC} was increased. However, the V_{OC} decreased with increasing the thickness of WO_x, which may be due to the recombination loss of carriers in their films. The J_{SC} of this series of solar cells also showed a trend of increasing at first and then decreasing, which indicated that the carrier collection ability of the device was also affected by the thickness of WO_x. The FF of the device was a comprehensive reflection of the combined effect of multiple factors such as band bending at the interface and R_S. When the thickness of WO_x became relatively small (< 20nm), the series resistance turned to be low. When the thickness of WO_x was increased within this range, the built-in potential increased, which was beneficial to carrier separation. However, when the thickness of WO_x exceeded a certain value, the increase of resistance of WO_x layer was not conducive to carrier collection, which was reflected

in the decrease of FF and J_{SC}. When the thickness of WO_x was 20 nm, the best power conversion efficiency was obtained as 17.64%. The V_{OC}, J_{SC}, and FF of the device were 635 mV, 37.39 mA/cm^2, and 73.35%, respectively.

For the silicon heterojunction solar cells with VO_x as HTL, it was difficult to control the temperature of vanadium wire during the preparation of VO_x thin film, causing the vanadium wire to fuse, so the thickness of VO_x film was not optimized. According to the optimization results of MoO_x and WO_x, the VO_x thickness was set at 18 nm to fabricate the solar cells, whose *J-V* curve is shown in Figure. 4.10. The V_{OC}, J_{SC}, FF and PCE of the solar cell are 545 mV, 36.63 mA/cm^2, 71.80% and 14.33% respectively.

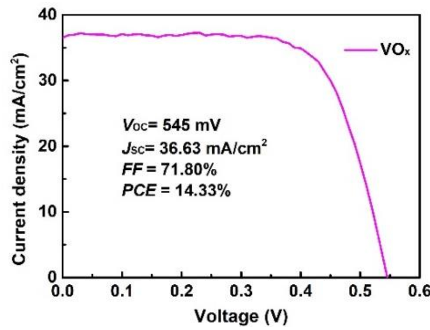

Figure 4.10 The J–V characteristic of SHJ solar cell with VO_x as HTL.

Figure 4.11 shows the conventional (light) and dark *J-V* curves of SHJ solar cells with Ag/ITO/n+ a-Si/i a-Si:H on the front side and MoO_x, WO_x, and VO_x on the rear side. The light *J-V* curve of the sample with MoO_x and WO_x as HTLs are the curves of the sample with the highest power conversion efficiency, and the solar cell with VO_x as HTL is the light *J-V* curve in Fig. 4.10.

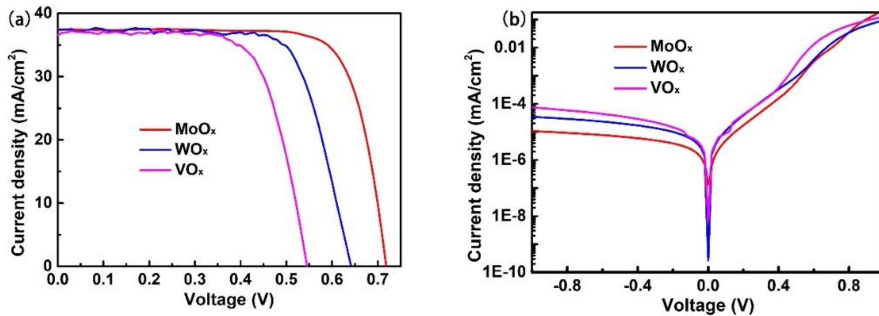

Figure 4.11 The light (a) and dark (b) J-V curves of the novel SHJ solar cell with MoO_x, WO_x, and VO_x as HTLs.

Table 4.2 The performance parameters of three heterojunction cells with MoO_x, WO_x, and VO_x as HTLs, and the SHJ solar cell as a reference cell.

	V_{OC} (mV)	J_{SC} (mA/cm^2)	FF (%)	PCE (%)	Rs (Ω)
SHJ	731	38.20	80.0	22.34	1.6
MoO_x	713	37.50	78.9	21.10	2.41
WO_x	635	37.39	73.4	17.64	4.42
VO_x	535	36.63	71.8	14.33	3.66

The photovoltaic parameters of three heterojunction cells with MoO_x, WO_x, and VO_x as HTLs are given in table 4.2. The performance of conventional SHJ cells are also given as reference. It can be seen from table 4.2 that the performance of the SHJ solar cell with MoO_x as HTL is similar to that of the conventional one as a reference (see Figure 5.1 in Chapter 5 for the light *J-V* curve of SHJ), indicating that MoO_x had good hole selective transport effect and could replace p-type doped amorphous silicon.

For the heterojunction solar cells with WO_x and VO_x as HTLs, the performance may be improved by further optimizing the device. However, according to observation and experimental results, it could be concluded that the performance of the SHJ solar cell with MoO_x as HTLs was better than those with WO_x and VO_x as HTLs.

The V_{OC} of heterojunction solar cells with WO_x and VO_x as HTLs was lower than that of MoO_x solar cells. The factors that affected V_{OC} mainly included the work function of TMO and interface characteristics. It is generally believed that the higher the TMO work function, the greater the bending degree of the energy band. For the measurement of TMO work function, different research groups, different material fabrication methods and test conditions have great differences in the work function of materials. We have also tried to measure the work functions of three kinds of TMO thin films, but it is difficult to obtain accurate and reasonable values of the work functions of TMO films because they are easily affected by the testing environment. Kirill Zilberberg *et al.* reported the work function of MoO_x, WO_x, and VO_x fabricated by thermal evaporation as 6.7, 6.5, and 6.7 eV, respectively[109-111]. According to the relationship of the work function of the three TMOs given by them, we can roughly judge that the V_{OC} of heterojunction solar cells with MoO_x as HTL was higher than

that of WO_x cells. However, the V_{OC} of VO_x solar cell does not show the performance corresponding with its work function, which might because the work function of VO_x was more easily affected by the environment. In addition, the V_{OC} of SHJ devices may also be related to the defect density of the interface. It can be seen from Figure 4.11 (b) that the reverse saturation current density was $MoO_x < WO_x < VO_x$, which could exhibit the density of interface defect states to a certain extent. In addition, by fitting the dark *J-V* curve, the saturation current density J_{01} (refer to the fitting data in table 5.3 in Chapter 5) of the ideal region (about 0.4 V~0.65 V) was 5.59×10^{-13} A/cm^2 for MoO_x, 1.31×10^{-12} A/cm^2 for WO_x and 4.81×10^{-11} A/cm^2 for VO_x, respectively. According to the relationship between J_{01} and V_{OC}, the relative value of V_{OC} can be understood. The above analysis of saturation current density shows that the interface between WO_x and VO_x had a higher density of defect states. On one hand, it may be related to the higher hot-wire temperature used in the fabrication of the two films; on the other hand, it may also be related to the difference of the environment during the device fabrication. The specific mechanism needs further study. In conclusion, for obtaining high PCE of SHJ solar cells, it is necessary to maintain the high work function characteristics of TMO materials and reduce the density of defect states at the interface, which requires to avoid the contact between TMO film and water vapor or oxygen in the surroundings, and to avoid the oxidation of the intrinsic amorphous silicon passivation layer and the damage to the TMO/crystalline silicon interface.

The FF of the device is mainly affected by the series resistance. The R_S of MoO_x solar cell was the smallest, which was 2.41 Ω, followed by 3.66 and 4.42 Ω for VO_x and WO_x solar cells, respectively. Due to the same front structure of the three types of solar cells, the difference on R_S mainly exhibited the contact condition of Ag/TMO/i a-Si:H. at the same time, the conductivity of TMO material also had a great influence on the Rs of these solar cells. According to the third chapter, the conductivity of MoO_x (2.58×10^{-6} S/cm) was higher than that of WO_x film (5.14×10^{-7} S/cm), which was consistent with the results that the R_S of MoO_x solar cell was lower than that of WO_x solar cell. In addition, we also notice that the R_S of VO_x solar cell was smaller than that of WO_x solar cell, too. But FF of VO_x solar cell was smaller than that of WO_x cell, which may be related to that VO_x thickness was not an optimal one. It is concluded that TMO thin films could be doped with appropriate methods to improve their conductivity, reduce the series resistance, enhance the transport and collection capacity of carriers, and improve the FF of devices.

The J_{SC} of solar cell shows the collection capacity of the device for carriers, which is mainly affected by the structure of the front surface of the solar cell. Because the front surface structure of the devices was Ag/ITO/n+ a-Si/i a-Si:H, the J_{SC} difference of the devices was relatively small. The J_{SC} may also be affected by the thickness of TMO layer and R_S. The optimal thickness of WO_x (20 nm) was slightly larger than that of MoO_x (14 nm). Thick TMO films would increase the recombination of carriers, which

was not conducive to carrier collection. The thickness of VO_x was not an optimal one, which was also the reason the J_{SC} of VO_x solar cell turned to be small.

4.3 Application of MoO_x and WO_x in lithography-free and dopant-free back contact heterojunction cells

The interdigitated back contact (IBC) solar cells with back contact structure showed high performance, due to that all the electrodes of the solar cells were on the rear side, which could reduce the blocking effect of front electrode on sunlight improving the solar cell's absorption of sunlight, and then rose the short-circuit current density of solar cells. In order to avoid the back-contact short circuit between the positive and negative electrodes of the interdigital back contact solar cells, photolithography has been usually applied to realize the graphical distribution of the interdigital back electrodes. Therefore, the development of lithographic-free back contact solar cells has become an important direction to promote the industrialization of the IBC solar cell.

Our above results show that MoO_x thin films deposited by HWOSD can be used as HTL to replace p-type doped amorphous silicon in SHJ solar cells. In Chapter 3, WO_x thin films fabricated by hot HWOSD had high transmittance in the sunlight range (the average transmittance is 97.46% between 300 nm and 1200 nm), and the refractive index of WO_x was about 2.3, so it is suitable to be used as antireflection coating on the surface of crystalline silicon cells. Herein, MoO_x and WO_x are used as HTL and antireflection layer, respectively, in the fabrication of IBC-SHJ without photolithography and doping. The IBC electrode of the solar cell was realized by metal mask, avoiding complicated lithography process.

The fabrication process of the IBC solar cell is shown in Figure 4.12. First of all, PECVD was used to deposit amorphous silicon with thickness of 6 nm on both sides of textured n-type silicon wafer to achieve efficient passivation. Then, WO_x with a thickness of 120 nm was deposited on the front surface of silicon wafer by HWOSD as the antireflection layer. MoO_x (HTL) and Ag/Al electrodes with 15 nm were deposited on the back surface of silicon wafer covered by metal mask A by HWOSD and thermal evaporation. The mask A was removed and the silicon wafer back-light was treated with ultraviolet ozone for 8 min to form SiO_x passivation layer. Then, the ETL of TiO_2 were obtained on the whole back-light surface by solution method and annealing process. Finally, the Mg/Al/Ag electrode was obtained by thermal evaporation under mask B at a suitable position on the back-light surface. There was a gap of about 50 μm between the electrode and the HTL electrode structure to avoid short circuit. The left corner of Figure 4.12 shows the morphology of the back-light electrode of the back contact solar cell fabricated in this study.

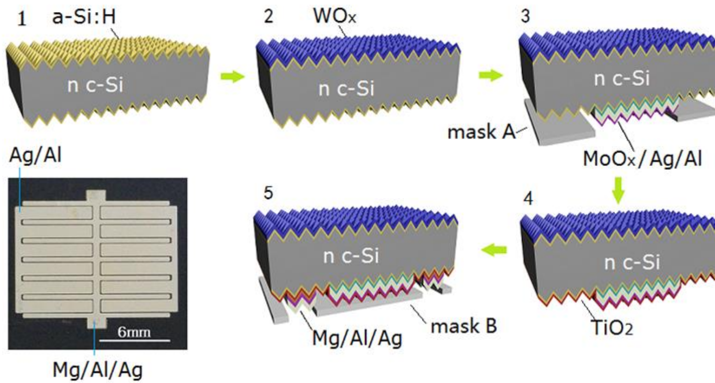

Figure 4.12 Scheme of the fabrication process of the lithography-free and dopant-free IBC-SHJ solar cells.

As the ETL of IBC-SHJ solar cells, TiO_2 thin films would selectively transport photo-generated electrons. The preparation process was as follows: the TiO_2 sol was diluted and dissolved for obtaining its 0.15% (wt/wt%) butanol solution. Then, it was spun on the back of the solar cell at 7000 rpm and annealed at 140 °C for 5min to form TiO_2 film.

In this solar cell, the high transmittance and low reflectivity optical properties of WO_x thin films prepared by HWOSD were fully utilized (see Figure 4.13). MoO_x and TiO_2 were used as HTL and ETL to replace the doped amorphous silicon in conventional IBC solar cells, which could avoid the use of toxic precursors. Moreover, WO_x could directly contact with Ag avoiding the deposition of TCO layer, which simplified the structure and preparation process of IBC solar cells, and reduces the fabrication cost of IBC solar cells.

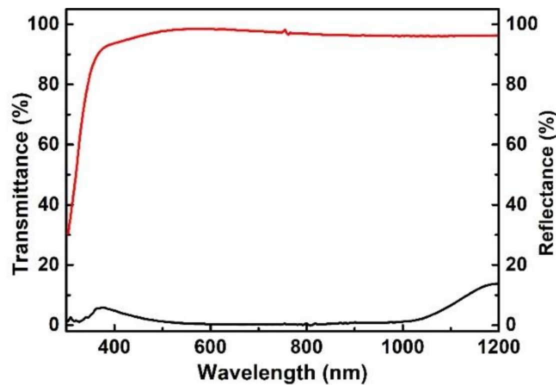

Figure 4.13 Transmittance of the WO_x films on glass substrates and reflectance of the WO_x films on textured silicon wafers.

After optimizing the parameters of the device, the best performance of the device was achieved as: V_{OC} of 696 mV, J_{SC} of 38.61 mA/cm^2, FF of 75.31%, and power conversion efficiency of 20.24%, and its *J-V* curve is shown in Figure 4.14 (a). The EQE and 1-R spectra of the device are shown in Figure 4.14 (b). The integral for current density was 38.12 mA/cm^2 by integrating the curves in EQE spectrum, which is basically consistent with J_{SC} obtained by *J-V* test. The 1-R spectrum of the device also shows that the device has good absorption performance for sunlight.

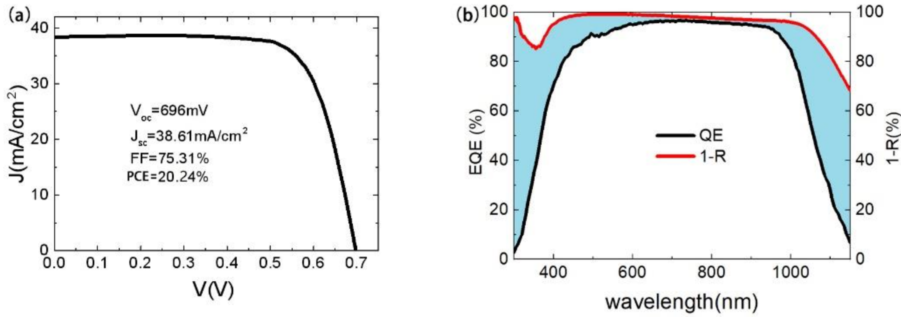

Figure 4.14 (a) J-V curve of the champion lithography-free IBC-SHJ solar cell. (b) The EQE and 1-R spectra of the champion IBC-SHJ solar cell.

4.4 Conclusion

In this chapter, novel silicon heterojunction solar cells with TMO as HTLs were studied.

The optimal passivation layer, MoO_x thickness and annealing process were concluded as: i a-Si:H, 14 nm, and pre-annealing-HF treatment, respectively. The highest performance solar cells were obtained: V_{OC} of 713 mV, J_{SC} of 37.50 mA/cm^2, FF of 78.92%, and PCE of 21.10%.

The photovoltaic characteristics of solar cells with MoO_x, WO_x, and VO_x as HTLs were investigated. The best performance obtained from solar cells with MoO_x as HTLbased on the high V_{OC} of MoO_x solar cells. By comparing the performance of solar cells with WO_x and VO_x as HTL, it was recognized that the main factor affecting heterojunction devices performance was the larger work function of MoOx, causing large band bending at the interface with Si. In addition, the density of defect states at the interface of MoO_x and Si was relatively small, leading MoO_x solar cells acquiring

higher V_{OC}. Therefore, in order to improve the performance of heterojunction solar cells with TMO as HTLs, we should try our best to improve the work function of TMOs and the density of defect states at the heterojunction interface, and to avoid the contact with water and oxygen during the device fabrication.

WO_x thin film with high transmittance was used as antireflection layer and MoO_x thin film with high work function was used as HTL in lithography-free and dopant-free back contact solar cell. The following device performances were obtained: V_{OC} of 696 mV, J_{SC} of 38.61 mA/cm^2, FF of 75.31%, and power conversion efficiency of 20.24%.

Chapter 5. Transport mechanism of silicon heterojunction solar cells

In Chapter 4, the performance of SHJ solar cells with MoO_x, WO_x, and VO_x as HTLs were systematically optimized, with gradually increased the PCE of 21.10% obtained. For these type SHJs, the formation energy band bending or space charge region formation at the interface was due to the large work function difference between TMO and n-type crystalline silicon, which was different from traditional crystalline silicon solar cell PN junction based on doping type and concentration variation. Moreover, the material properties of these undoped metal oxides are also different from those of conventional amorphous silicon/crystalline SHJ. Therefore, the transport mechanism of such SHJs may be different from both that of conventional PN junction solar cells and that of conventional amorphous silicon/crystalline SHJ cells. The research on the junction characteristics and carrier transport behavior of these solar cells is not only helpful to further understand the transport mechanism of the solar cells, but also provide guidance for further improving the performance of such solar cells.

This chapter explores the junction characteristics and carrier transport of SHJ solar cells with MoO_x, WO_x, and VO_x as HTLs from three aspects: Firstly, through the research of high frequency capacitance-voltage (*C-V*) characteristics of solar cells, the differences of interface characteristics and built-in potential of solar cells were analyzed. Secondly, the effects of MoO_x, WO_x, and VO_x on the reverse saturation current, interface recombination current, and the quality factor of diodes were discussed by testing and analyzing the dark *J-V* of solar cells at room temperature. Finally, by analyzing the variable temperature dark *J-V* curve of solar cells, the carrier transport mechanism in different voltage regions was explored. which provided a theoretical basis for the further research of this kind of devices.

5.1 High frequency capacitance-voltage (*C-V*) characteristics of SHJ solar cells

The SHJ solar cells with MoO_x, WO_x, and VO_x as hole selective transport layers and commercial SHJ cells were selected (with an active area of 1 cm^2). Firstly, the light *J-V* of each solar cell was tested. The structure diagram and *J-V* curves of the solar cells are shown in Figure 5.1, and the corresponding performance parameters of the solar cell are shown in table 5.1. For comparison, the performance of commercial SHJ solar cells was measured as well. It can be seen that the performance of each type of solar cellwas SHJ > MoO_x > WO_x > VO_x. The J_{SC} of heterojunction solar cells with MoO_x, WO_x, and VO_x as HTLs had little difference due to their same front surface structure. The J_{SC} of commercial SHJ solar cells was higher than that of the SHJ cells

with TMOs, which could be attributed to the differences in the surface texture of crystalline silicon, TCO, and a-Si:H between SHJs with TMO and the commercial SHJ solar cell. The V_{OC} of SHJ solar cells with MoO_x, WO_x, and VO_x as HTLs presented significant differences, which would be further analyzed through *C-V* tests.

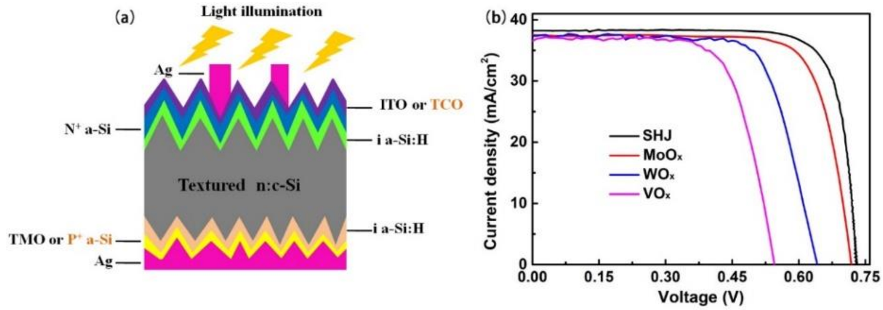

Figure 5.1 (a） Cross-section of the different solar cell structure with different HTLs. (b) The J-V curves of the different solar cells.

The essence of energy conversion of solar cells is based on the photovoltaic effect produced by the heterojunction barrier or space charge region of PN junction. According to the introduction in Chapter 2, through the study of *C-V* characteristics at high frequency, we could understand the junction characteristics to a certain extent. Because commercial SHJ solar cells and silicon heterojunction solar cells with MoO_x, WO_x and VO_x as HTL present little difference on side of the n-type silicon, the *C-V* characteristics of theirs can be analyzed to understand their performance differences caused by different TMOs as HTLs.

Table 5.1 The parameters of the different solar cells

	V_{OC} (mV)	J_{SC} (mA/cm^2)	FF (%)	PCE (%)	Rs (Ω)	Rsh (Ω)
SHJ	732	38.14	75.9	21.20	1.60	34.50
MoO_x	713	37.50	78.9	21.10	2.41	64.90
WO_x	643	37.39	73.4	17.64	4.42	354.86
VO_x	545	36.63	71.8	14.33	3.66	66.60

The *C-V* study for four kinds of solar cells was performed and the $1/C^2 \sim V$ relationship in the bias voltage range of -1 to 0.2 V was obtained, as shown in Figure 5.2. It is not difficult to find that the slope and intercept on the X-axis of the $1/C^2 \sim V$ curve of every solar cell are different from each other. The slope K of the $1/C^2 \sim V$ curve of the four kind of solar cells obtained by fitting is given in table 5.2, and it's relationship is $K_{MoOx}<K_{SHJ}<K_{WOx}< K_{VOx}$. The intercept V_D (built-in potential) of the extension line of the $1/C^2 \sim V$ curve in the X-axis is also given in table 5.2, and their relative size is $V_{D\ MoOx} > V_{D\ SHJ} > V_{D\ WOx} > V_{D\ VOx}$.

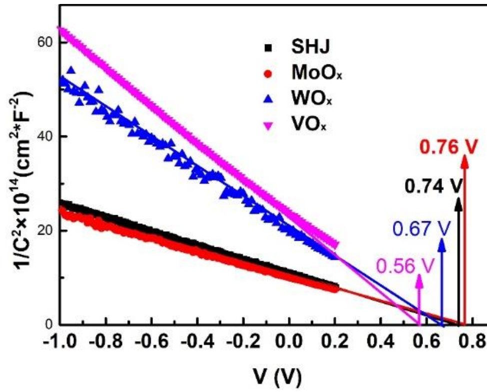

Figure 5.2 The $1/C^2$-V curves of the four different solar cells.

Table 5.2 The interface parameters of four solar cells

	V_D（V）	K	X_D（μm）
SHJ	0.74	-14.88	0.348
MoOx	0.76	-13.64	0.368
WOx	0.67	-31.63	0.277
VOx	0.56	-38.41	0.188

The four kinds of solar cells possessed the same doping concentration on the silicon wafer (8×10^{15} cm^{-3}), while differing in their HTL materials. Therefore, the different slope of $1/C^2$~V was not caused by the doping concentration on silicon substrate. According to the research on heterojunction solar cells by Song *et al.*[92] and results from our group[52], the interface characteristics of heterojunction could also result in the slope changes of *C-V* curve. The larger the slope of *C-V* curve was, the greater the density of defect states at the interface would be. Therefore, it can conclude that the

relationship between the density of states of the hole transport layer and the interface of TMO/crystalline silicon is MoO_x<SHJ<WO_x<VO_x. The relationship between the density of defect states of the new heterojunction solar cells with TMOs as HTLs is just opposite to the relative value of V_{OC}, which indicates that it is reasonable to characterize the interface state by the slope of $1/C^2$~V curve.

Because the thickness of TMO thin film was relatively thin, the space charge region of silicon heterojunction solar cells with TMO as HTLs was mainly located on the side of crystalline silicon (similar to one-side abrupt junction). When the applied bias voltage varied, the changes of depletion zone width mainly reflected the change of space charge area width on the silicon side. Therefore, the intercept changes of *C*-*V* curve and X-axis mainly exhibited the change of built-in electric field in crystalline silicon. Moreover, TMO film had a high density of defect states, which could realize Fermi level pinning. It could be considered that the TMO/Si interface formed a metal-like/semiconductor contact junction. Therefore, we can estimate the depletion layer width in crystalline silicon according to the one-side abrupt junction (or metal/semiconductor junction). The estimated depletion layer widths of the heterojunction with MoO_x, WO_x, and VO_x as HTLs are 368, 277, and 188 nm respectively. According to Schottky model[112], the barrier height of ideal metal semiconductor contact was affected by the work function of metal (here corresponding to HTLs), but the built-in potential and the width of depletion region obtained here are not directly related to the work functions of three TMO materials. The defect states in the TMO film and at the TMO/Si interface could affect the charge distribution in the junction region. Therefore, it could be considered that the defect states in the TMO and at the TMO/Si interface were the main factors affecting the band bending and the width of the depletion zone.

To obtain higher performance of heterojunction solar cells with TMO as HTLs, it is necessary to control the density and distribution of defect states (related to the Fermi level and work function of TMO) in the TMO thin film and reduce the density of states at the interface between TMO and crystalline silicon, obtaining higher built-in potential and improve the V_{OC} of solar cells Device.

5.2 Dark *J-V* characteristics of SHJ solar cells at room temperature

The *J*-*V* or dark *J*-*V* curve of solar cells at room temperature is an important analysis method to understand the junction characteristics of solar cells[113]. For conventional a-Si: H/c-Si heterojunction, the dark *J*-*V* and transport model have been studied. R. Hussein *et al*[93]. measured the dark *I*-*V* of heterojunction solar cells with Al/(p) c-Si/(n) a-Si: H/ITO/metal grid, and analyzed the transport mechanism in different voltage regions using a two-diode model. When the voltage $V < 0.15$ V, the parallel

resistance was the main factor affecting the dark current; When the voltage fell in 0.15 V < V < 0.45 V, the dark current of the solar cell was affected by the recombination current in the space charge region; When the voltage was 0.45 V < V < 0.6 V, the diffusion current in the diffusion region became the dominant dark current of the device; when V > 0.6 V, the series resistance of the device turned to be the main factor affecting the dark current of the device.

Song *et al.*[92] studied the dark *J-V* characteristics of a-Si:H/p-type c-Si heterojunction and inserted μ c-Si buffer between them, It was found that at low forward bias (V < 0.3 V), the recombination process caused by the interface defect state at a-Si:H/μ c-Si interface was the dominant factor affecting the dark current of the device. In the high bias region (0.3 V<V<0.55 V), the dark *J-V* behavior of the device was affected by the multi-step tunnel capture emission (MTCE) mechanism. In the higher voltage region (V>0.55 V), the carrier transport of the device was affected by the space charge limited current.

Our research group also studied the *I-V* characteristics of n-type nano-silicon/p-type crystalline silicon heterojunction solar cells[114]. Similar to the work reported by Hussein *et al.[93]* and Song *et al*.[92], the dark *I-V* characteristics of the heterojunction solar cells could also be analyzed by the two-diode model. The *I-V* curve in the forward bias range was also able to be divided into four regions, including the non-ideal diode zone 2 (0.15 V<V<0.3 V) which showed a large ideal factor (n >3), which might be related to the tunneling transport associated with interface defects. The above research provided a very important base for this study. In this section, we will compare the dark *J-V* behavior of heterojunction solar cells with MoO_x, WO_x, and VO_x as HTLs and conventional SHJ cells, and study the influence of different TMO on the *J-V* characteristics of heterojunction.

The dark *J-V* characteristic curves of Ag/ITO/n+ a-Si/i a-Si:H/n-type c-Si/i a-Si:H/TMO/Ag and commercial SHJ solar cells at 300 K are shown in Figure 5.3. The voltage range is - 1 V <V< 1 V.

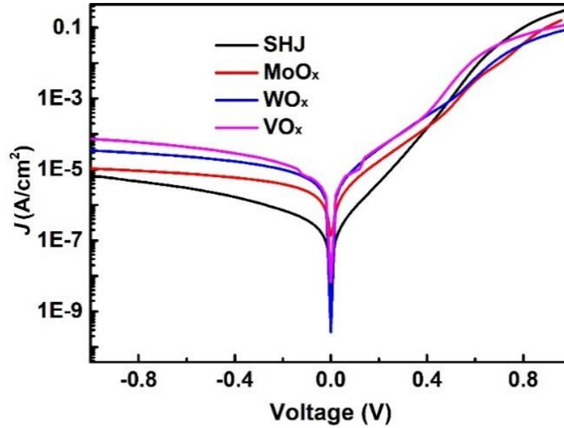

Figure 5.3 Dark J-V curve of the different solar cells.

It can be seen from Figure 5.3 that the forward and reverse dark *J-V* curves of SHJ cells and new heterojunction solar cells with MoO_x, WO_x, and VO_x as HTLs are different, indicating that the carrier transport behavior of the new heterojunction solar cells is different from that of the commercial SHJ cells.

According to the shape of the *J-V* curves, the dark *J-V* curves of the four solar cells in the forward bias range are roughly divided into four regions: the region 1 is V<0.15V, and the *J-V* relationship in this region is affected by the parallel resistance; the region 2 is the low voltage region, which is mainly affected by the heterojunction interface, corresponding to the non-ideal diode 2 in the two-diode model; the region 3 is relatively high voltage region, which exhibits the transport characteristics of ideal junction such as the diffusion current of PN junction or the thermal emission current of metal semiconductor contact junction, which corresponds to the ideal diode 1 in the two-diode model; the region 4 is the influencing region on series resistance with higher voltage. In Figure 5.4 (a-d), the regions are classified according to the trend of *J-V* curves of the four types of solar cells to be discussed.

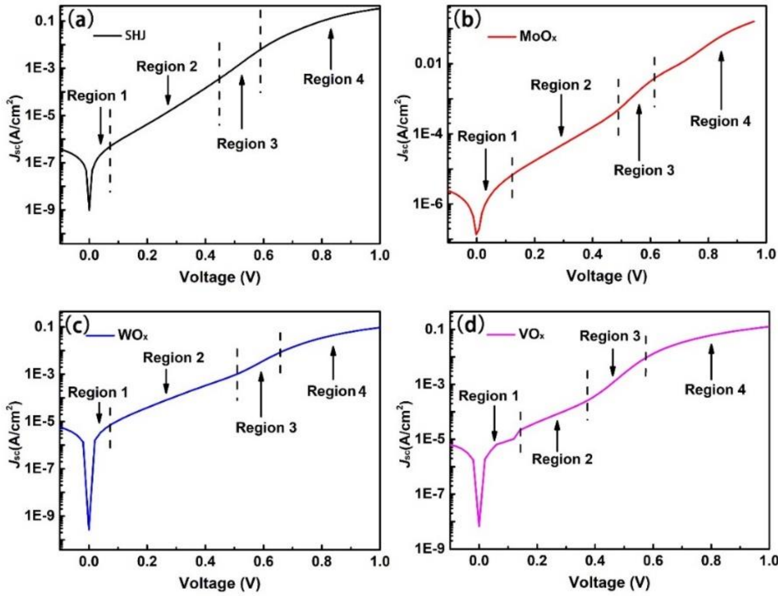

Figure 5.4 (a) Dark J-V curve of SHJ solar cells with no TMOs (a), with MoO_x as HTL (b), with WO_x as HTL(c), and with VO_x as HTL (d) under forward bias voltage.

Based on the two-diode model, the dark *J-V* curves of four kind of solar cells are simulated in four regions. The simulation parameters of different regions are shown in table 5.3. The first region and the fourth region in the *J-V* curve are related to the parallel resistance and series resistance of the device respectively. As a start, we make a brief analysis of these two regions. Firstly, in this higher voltage region 4, the current of solar cells is mainly affected by the series resistance (Rs) of the devices. According to Ohm's law, the series resistance of four kinds of solar cells can be calculated as: Rs =1.79, 2.35, 3.99, and 3.51 $\Omega \cdot cm^2$, respectively, for SHJ solar cells. The relative values of series resistance of the four kind of devices with different structures were: SHJ $<$ MoO_x $<$ VO_x $<$ WO_x. The difference of series resistance reflected the influence of different hole selective transport layer on carrier transport capability, which was mainly related to the conductivity of hole transport layer material. The conductivity of MoO_x and WO_x measured in Chapter 3 could well support the conclusion. It was seen that the conductivity of hole selective transport layer material was an important factor affecting the device performance. For the parallel resistance control region 1 with voltage (V<0.15 V), the parallel resistance Rsh in table 5.3 was obtained by fitting the *J-V* behavior of this region, and the size relationship was SHJ>MoO_x>WO_x>VO_x. The results showed that the leakage loss of four kinds of

solar cells was SHJ < MoO_x < WO_x < VO_x. The parallel resistance of three heterojunction solar cells with TMO as hole transport layer was significantly lower than that of commercial SHJ cells, which may be related to the device cutting process.

Next, the second and third regions of the *J-V* curve were analyzed. The analysis of the carrier transport behavior in these two regions could give a good understanding of the junction characteristics. Firstly, the dark *J-V* curve of low voltage region (0.15 V～0.5 V) was studied. In this region, due to the low current based on ideal diode, the contribution of recombination process or tunneling process related to interface defect state (non-ideal diode) to electrical transport will be shown. According to the second term of the two-diode electric transport equation (2.12) in Chapter 2, the relationship between current and voltage in this region can be expressed as follows:

$$I(V) = I_{02}\left[exp\frac{q(V-IR_S)}{n_2kT}\right] \quad (5.1)$$

Where n_2 is the ideal factor of non-ideal diode 2, I_{02} is the reverse saturation current and R_S is the series resistance.

Taking logarithm of formula (5.1), the following formula can be obtained:

$$lnI = lnI_{02} + k_2 * V' \quad (5.2)$$

Where V'= V-IRs, k_2 =q/ (n_2kT), kT/q= 0.026 V at room temperature.

According to formula 5.2, the ideal factor n_2 of diode can be obtained from the slope of the straight line. The intersection point between the line and the Y axis would be the saturation current, specific parameters are found in region 2 in table 5.3. It can be seen that the n_2 of SHJ solar cell was close to the ideal factor (n_2=2) of non-ideal diode based on the recombination process of depletion region. However, the n_2 of silicon heterojunction solar cells with MoO_x, WO_x, and VO_x as HTLs were far away from 2, ranging from 3 to 4, which indicated that the novel heterojunction might have different transport mechanism from the recombination current in the depletion region, such as the tunneling current related to the interface defect state, which would be analyzed in detail by the *J-V-T* curve.

Next, the third region, i.e., the ideal diode region was analyzed. Since the current in the third region may be affected by the series resistance of region 4 and the non-ideal transport process of region 2, we have deducted their contributions in this voltage region (equation 5.3) in the analysis, and then fitted according to equation 5.4 to obtain the ideal factor n_1 and saturation current I_{01} representing ideal diode 1, as shown in table 5.3, region 3.

$$I_{D1} = I_{01}\left[exp\frac{q(V-IR_S)}{n_1kT}\right] = I(V) - I_{02}\left[exp\frac{q(V-IR_S)}{n_2kT} - 1\right] - \frac{V-IR_S}{R_{sh}} \tag{5.3}$$

Taking logarithm of formula (5.3), the following formula can be obtained:

$$lnI_{D1} = lnI_{01} + k_2 * V' \tag{5.4}$$

Where $V'=V-IR_s$, $k_1=q/(n_1kT)$， at room temperature $kT/q=0.026$ V.

Table 5.3 Simulation parameters of the different solar cells according to the two-diode model

	Region 4	Region 3		Region 2		Region 1
	R_s/ Ω	n_1	J_{01}/Acm^{-2}	n_2	J_{02}/Acm^{-2}	R_{sh}/k Ω
SHJ	***V*>0.6V**	**0.4 V<*V*<0.6 V**		**0.15 V<*V*<0.4 V**		**V<0.15**
	1.79	1.14	3.51×10^{-12}	2.18	1.08×10^{-7}	83
MoO_x	***V*>0.61 V**	**0.5 V<*V*<0.61 V**		**0.15 V<*V*<0.5 V**		**V<0.15**
	2.35	1.04	4.66×10^{-13}	3.68	1.43×10^{-6}	16
WO_x	***V*>0.65 V**	**0.5 V<*V*<0 .65 V**		**0.15 V<*V*<0.5 V**		**V<0.15**
	3.99	1.08	1.09×10^{-12}	3.62	3.83×10^{-6}	7.5
VO_x	***V*>0.57 V**	**0.37 V<*V*<0.57 V**		**0.15 V<*V*<0.37 V**		**V<0.15**
	3.51	1.09	4.01×10^{-11}	3.76	4.18×10^{-6}	6.6

The ideal diode factor n_1 of the four kind of solar cells are close to 1, which is between 1.04 and 1.14 indicating that the carrier transport behavior of the four kind of solar cells basically conforms to the ideal diode characteristics in the voltage region. In this region, the saturation current densities J_{01} of the four batteries are 3.51×10^{-12}, 4.66×10^{-13}, 1.09×10^{-12} and 4.01×10^{-11} A/cm^2, respectively. It is generally considered that in the case of ideal PN junction, J_{01} and V_{OC} meet the following relationship. In order to obtain high open circuit voltage, low J_{01} is required.

$$V_{OC} = \frac{kT}{q} ln\left(\frac{J_{SC}}{J_0} + 1\right) \tag{5.5}$$

The J_{01} values of the three heterojunction cells with TMO as HTLs are consistent with the measured V_{OC} and built-in potential measured by *C-V*. The solar cell with MoO_x as HTL has the lowest J_{01}, which indicates that the device has high open voltage potential.

5.3 Characteristics of dark *J-V-T* in heterojunction solar cells

The measurement of variable temperature dark *J-V* (or *I-V*) curve of solar cells is an important analysis method to study the transport mechanism of the device. It is generally believed that the carrier transport models of heterojunction solar cells

include recombination, tunneling, diffusion, and thermal emission[92, 93]. In order to further study the carrier transport mechanism of heterojunction solar cells with MoO_x, WO_x, and VO_x as HTLs fabricated by HWOSD, the heterojunction solar cells with structure of Ag/ITO/n+ a-Si/I a-Si:H/n-type Si/i a-Si:H/HTL/Ag were measured by variable temperature dark *J-V*. The test temperature is 220K, 240K, 260K, 280K, 300K and 320K. The J-V-T curves are shown in Figure 5.5.

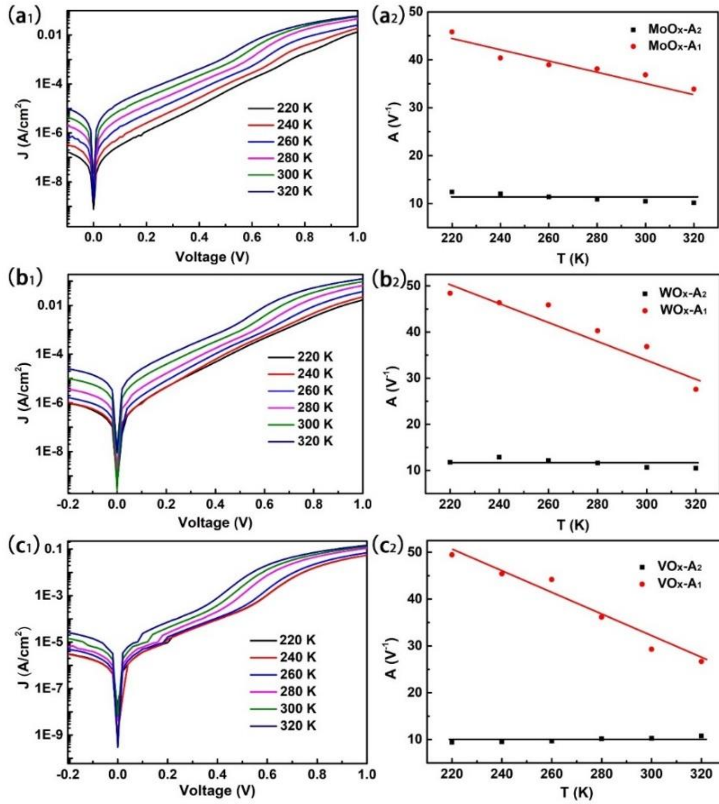

Figure5.5 (a_1) The dark J-V-T curves of the heterojunction solar cell with MoO_x as HTL. (a_2) The relationship between the temperature-dependent coefficient A and T of the heterojunction solar cells with MoO_x as HTL. (b_1) The dark J-V-T curves of the heterojunction solar cell with WO_x as HTL. (b_2) The relationship between the temperature-dependent coefficient A and T of the heterojunction solar cells with WO_x as HTL. (c_1) The dark J-V-T curves of the heterojunction solar cell with VO_x as HTL. (c_2) The relationship between the temperature-dependent coefficient A and T of the heterojunction solar cells with VO_x as HTL.

The two-diode model was used to fit the *J-V-T* curve. Considering the series resistance, parallel resistance, ideal diode, and non-ideal diode, the relationship between the current density and the applied bias voltage of heterojunction solar cells can be expressed as follows:

$$J = J_{01}\left[e^{A_1(V-JR_S)} - 1\right] + J_{02}\left[e^{A_2(V-JR_S)} - 1\right] + \frac{V-JR_S}{R_{sh}} \quad (5.6)$$

Where J_{01} and J_{02} represent the saturation current density of diodes 1 (ideal diode) and 2 (non-ideal diode), respectively, and R_S and Rsh are the series resistance and parallel resistance of the device. Factors A_1 and A_2 are related to the transport mechanism and can be expressed as follows:

$$A_i = \frac{q}{n_i kT} \quad (5.7)$$

Where i represents diode 1 or 2, q is electronic charge, n_i is the ideal factor of the corresponding diode, k is the Boltzmann constant and T is the absolute temperature.

When analyzing the transport mechanism, the voltage regions of series resistance and parallel resistance were excluded, and the second and third voltage regions were focus on, divided on the *J-V* curve in the previous section, e.g., the voltage regions representing non-ideal diode and ideal diode. We can understand the device transport mechanism through *J-V-T* analysis of these two regions. It can be seen from Fig. 5.5 (A_1) that the slope of dark *J-V*-T curve of heterojunction solar cells changes significantly when the applied bias voltage is 0.4 ~ 0.6V, and the changes on slope moves towards the low voltage region with the increase of temperature. According to changes of the slope, the *J-V-T* curve can be divided into two regions, namely the second and third voltage region mentioned in the previous section. The slope of the dark *J-V* curve measured at different temperatures is approximately the same in the lower voltage range, while it changes with the temperature in the higher voltage range. This shows that the heterojunction should have different transport mechanism in the two regions.

According to equation 5.6, the dark *J-V* curves at different temperatures in Figure 5.5 (a_1) are fitted to obtain the variation of factors A_1 and A_2 with temperature, as shown in Figure 5.5 (a_2). Firstly, the factor A_2 of the non-ideal diode represented by the low voltage region was analyzed. It can be seen that the value of A_2 varies in a narrow range from 10.17 to 12.44. Considering the errors in the process of device testing and data fitting, it can be concluded that the transport mechanism of heterojunction solar cells with MoO_x as HTL is mainly temperature independent. Among the four transport mechanisms of recombination, tunneling, diffusion, and thermal emission, only tunneling is not affected by temperature. Therefore, the transport mechanism in this

voltage region is likely to be tunneling. At this time, if we estimate the ideal factor n_2 of diode 2 according to formula (5.7), we can find that in the temperature range, n_2 has no definite value, but varies from 3.56 to 4.23. The average value of n_2 is 3.86, which is far greater than 2, corresponding to the recombination current in the depletion region. Large amount of n_2 has also been found in traditional a-Si/c-Si heterojunction solar cells. It is generally believed that it may be related to the shunt leakage current and interface recombination inside the devices, which often shows poor device performance (V_{OC}, FF, and Eff). However, our heterojunction solar cells have higher n_2 value and better device performance, which shows that the novel silicon heterojunction solar cells have different junction characteristics and transport mechanism to the traditional heterojunction solar cells. Garc í A-Hernansanza *et al.*[84] have simulated the transport mechanism of the novel silicon heterojunction solar cells. They believed that trap assisted tunnel transport played an important role in the carrier transport of MoO_x/n c-Si heterojunction solar cells. The *J-V-T* analysis from us also showed that tunneling played a role in the carrier transport of MoO_x/n-c-Si heterojunction.

Figure 5.5 (a_2) also shows the variation of factor A_1 with temperature obtained from formula (5.6). It can be seen that A_1 changes linearly with temperature T. At this time, according to formula (5.7), the ideal factor n_1 of diode 1 at different temperatures has roughly determined value (between 1.04 and 1.15), which is close to the ideal factor of ideal diode. The transport current in this voltage region may be in the form of diffusion current of ideal PN junction or thermal emission current of ideal Schottky junction, both of which are thermally activated and affected by temperature. The specific transport mechanism will be analyzed with the energy band diagram.

The dark *J-V-T* of heterojunction solar cells with WO_x as HTL was measured and analyzed. The results are shown in Figure 5.5 (b_1) and (b_2). The slope of the dark J-V curve of the heterojunction solar cells with WO_x as HTL also changes in the voltage range of 0.4 V～0.6 V in the forward bias, and the voltage cut-off point also moves to the left with the increase of temperature. According to the fitting method of variable temperature dark J-V curve similar to MoO_x solar cell, the factor A_2 of low voltage region (0.15 V$<V<$0.55 V) varies in a narrow range of 10.48 to 12.85, and has no obvious temperature (T) dependency , as shown in Figure 5.5 (b_2). This indicates that the temperature independent tunneling mechanism may also be the dominant transport mechanism in this voltage range. If the ideal factor n_2 is also calculated according to formula (5.7), it can be found that no definite value of n_2 can be obtained at different temperatures. n_2 varies from 3.45 to 4.47 with an average value of 3.78, which is much larger than that of the non-ideal diode based on depletion region recombination, indicating the existence of tunneling mechanism. According to the curve fitting of the device in the high voltage region ($V > 0.55$ V), A_1 decreases monotonically with the increase of temperature, as shown in Figure 5.5 (b_2). Similarly, according to formula

(5.7), the ideal factor n_1 at different temperatures can be roughly determined (between 1.03-1.19), which is close to the ideal factor of ideal diodes. It shows that there are ideal rectifier junction characteristics such as diffusion or thermal emission in this region.

By analyzing the dark *J-V* curves of the heterojunction solar cells with VO_x as HTL at different temperatures, the variation trend of A_1 and A_2 factors is similar with that of MoO_x and WO_x heterojunction, indicating that they have similar transport mechanism in the corresponding voltage region.

In order to further clarify the transport mechanism of the silicon heterojunction in different voltage regions, the specific transport model in formula (5.6) need to consider to simulate the *J-V-T* curve. Because MoO_x, WO_x, and VO_x have larger work functions and higher bulk defect density of states, the heterojunction with TMO/i a-Si:H/n c-Si can be analyzed approximately as Schottky rectifier junction with larger barrier height. In other words, when the TMO thin film with high work function is in contact with Si, the difference of work function can cause the energy band of crystalline silicon to bend upward and form a high barrier. For this reason, we give the energy band diagram of the heterojunction contact structure under forward bias and illumination conditions, as shown in Figure 5.6. Based on the above analysis and the energy band diagram, we consider that there are three possible carrier transport mechanisms in the heterojunction: thermal emission of electrons, thermally assisted tunneling of electrons, and defect assisted tunneling of holes, which correspond to the transport processes of a, b, and c in Figure 5.6 (a).

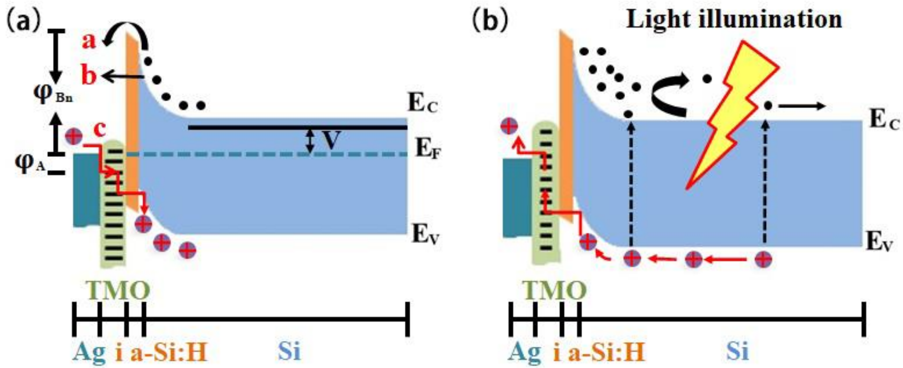

Figure 5.6 (a)Schematic energy band structures of the TMO/i a-Si:H/n-c-Si heterocontact under forward bias. Three transport processes, including thermionic emission of electrons, thermal-assisted tunneling of electrons, and tunneling of holes are denoted by a, b, and c, respectively. (b) Schematic energy band structures of the heterocontact under illumination.

For n-type silicon substrate, electrons are majority carriers and holes are minority carriers. The processes a and b marked in Figure 5.6 (a) both involve the thermal activation of majority carriers (electrons), that is, the electrons should firstly obtain enough energy to reach the top of the barrier (process a) or obtain energy to reach the energy position where they can be tunneled (process b). Therefore, we use a total thermal activation current J_{Te} of electrons to represent the thermal emission and thermal assisted tunneling processes. For the transport process c, a minority carrier holes enter the valence band top of c-Si via the defect states in MoO_x and recombine with electrons. We use J_{Tu} to denote the current density of the defect assisted tunneling of the holes. In this case, the transport equation of this kind of solar cells can be modified from equation (5.6) to:

$$J = J_{Te} + J_{Tu} + J_{shunt} = J_{01}\left[exp\left(\frac{q(V-JR_S)}{n_1kT}\right) - 1\right] + J_{02}\left[exp\left(\frac{q(V-JR_S)}{E_0}\right) - 1\right] + \frac{V-JR_S}{R_{sh}} \quad (5.8)$$

$$J_{01} = C(T)exp\left(-\frac{q\varphi_{Bn}}{kT}\right) \quad (5.9)$$

$$J_{02} = B(T)exp\left(-\frac{q\varphi_A}{kT}\right) \quad (5.10)$$

Where E_0 represents the barrier energy during tunneling and C (T) is the temperature dependent pre-factor. $q\varphi_{Bn}$is the effective barrier height of the electron. $q\varphi_A$ is the activation energy of the hole, which is actually the difference between the top of the valence band of c-Si and the Fermi level of Ag electrode in the band diagram 5.6 (a).

Comparing formula (5.6) with formula (5.8), we can see that J_{Te} and J_{Tu} correspond to diode 1 and diode 2 in formula (5.6), respectively. According to the formula (5.8), the dark *J-V* of MoO_x solar cells at 200, 300, and 360 K is fitted, respectively. The fit results are shown in Figure. 5.7.

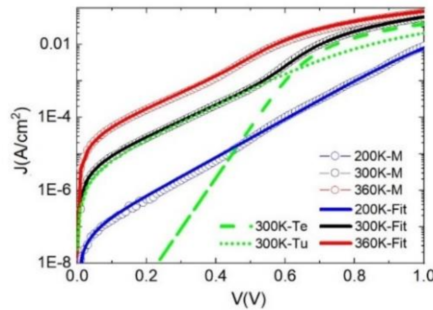

Figure 5.7 Experimental (hollow symbols) and fitting (solid lines) dark J–V curves under forward bias for the novel SHJ solar cell under three temperatures of 200, 300, and 360 K. The green dashed and dotted lines respectively represent the fitted J_{Te} (majority-carrier processes a and b) and J_{Tu} (minority-carrier process c) for the J–V curve measured under 300 K.

It can be seen from the figure that the measurement results of dark *J-V* at three different temperatures are in good agreement with the fitting results. The parameter of the MoO_x solar cell was obtained by fittingE_0， $q\varphi_A$ and $q\varphi_{Bn}$was 0.087, 0.29 and 0.98 eV, respectively. The fitting curve of $q\varphi_A$ and $q\varphi_{Bn}$ is shown in Figure 5.8 (black). It should be noted that the $q\varphi_{Bn}$ is 0.98 eV which is approximately equal to the sum of the built-in potential (0.76 V) obtained from the *C-V* curve and the E_C-E_F (about 0.21 eV can be determined according to the doping concentration of n-type crystalline silicon), which indicates the rationality of the fitting. In order to further understand the contribution of J_{Te} and J_{Tu} in the whole *J-V* curve, we use the green dotted line and dotted line to obtain the *J-V* curve of 300K in Figure 5.7.

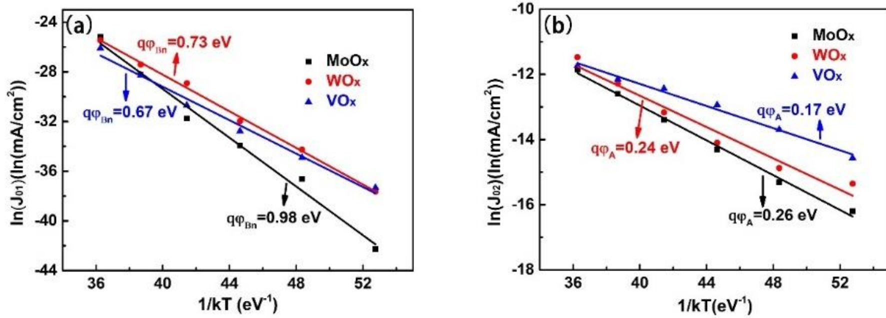

Figure5.8 (a) The fitting relationship between temperature and ln (J_{01}) of the different solar cells. (b) The fitting relationship between temperature and ln (J_{02}) of the different solar cells.

It can be seen from figure 5.7 that, when $V>0.6$ V, J_{Te} becomes the main component of current in the high voltage region. The electrical transport mechanism in this voltage region has an important impact on the performance of solar cells, especially V_{OC}. The effective barrier height of the electron is $q\varphi_{Bn}$, an important parameter in J_{Te}, in other word, the solar cell has higher V_{OC} and larger barrier height $q\varphi_{Bn}$is closely related. Such a high $q\varphi_{Bn}$ shows that in the MoO_x heterojunction solar cells, a strong inversion layer has been formed on the surface of crystalline silicon, which contributes to the efficient separation of photo-generated electrons and holes and the collection of photo-generated electrons (as shown in Figure 5.6 b). We also find that $q\varphi_{Bn}$ obtained by fitting is smaller than the difference of work function between MoO_x and Si, which may be due to the influence of interface defect state charge and dipole on barrier height. If the interface passivation with higher quality can be

achieved in the process of device optimization in the future, higher V_{OC} can be obtained. At the same time, the high conductivity of the inversion layer can enhance the transverse transport ability of the device, which is beneficial to obtain high FF.

In the region of $V<0.6$ V, J_{Tu} is the main component of dark current in MoO_x solar cells. There is a high density of defect states in the band gap of amorphous MoO_x thin films, which can be used as the channel of hole tunneling transport, making the hole tunneling rapidly and efficiently. It is not difficult to find that the tunneling current of these devices is significantly higher than that of conventional SHJ solar cells in this voltage region (Figure 5.3). The tunneling channel plays an important role in the collection of photo-generated carriers. Under light conditions, photogenerated holes can quickly tunnel through MoO_x film through the tunnel channel, which is one of the main reasons for high V_{OC} of these devices. Even in the high voltage region, J_{Tu} is an important part of the total current density J of the device, and J_{Tu} could not be ignored as usual in majority-carrier devices. The device is a Schottky-like one with high barrier or strong inversion.

Then, the dark J-V curves of heterojunction solar cells with WO_x and VO_x as HTLs were fitted by a similar method. The fitting results of $q\varphi_{Bn}$ and $q\varphi_A$ are shown in Figure 5.8. It can be seen from Figure 5.8 that the relationship of effective electrons barrier height $q\varphi_{Bn}$ is $MoO_x>WO_x>VO_x$, which are caused by three different oxides. According to the doping concentration of n-type silicon and $q\varphi_{Bn}$, it can be determined that the heterojunction solar cells with WO_x and VO_x as HTLs do not reach strong inversion. This shows that the high work function of WO_x and VO_x is not working well in these heterostructures, and the interface defect state plays a more important role in determining the barrier height. In other word, there is a high density of defect states at the interface between WO_x/crystalline silicon and VO_x/crystalline silicon, which makes the Fermi level pinned on the surface of crystalline silicon and limits the increase of the potential barrier. The hole tunneling activation energies of MoO_x, WO_x, and VO_x as HTLs heterojunction cells are obtained by fitting, whose relationship is: $MoO_x>WO_x>VO_x$, which reflects the difficulty of hole tunneling through the defect state in oxide, and is affected by the density of defect states in oxide and TMO/silicon interface. According to the relative value of $q\varphi_A$, the defect density of states of VO_x and the interface defect density of VO_x-devices are the largest, and the tunneling is the most likely to occur, followed by WO_x and MoO_x. This is basically consistent with the relative magnitude of the current density in the forward low voltage region and the reverse bias voltage in Figure 5.3. This shows that it is necessary to improve the quality of interface passivation in order to improve the performance of silicon heterojunction cells with WO_x and VO_x as HTLs.

5.4 Summary

In this chapter, the transport performance of heterojunction solar cells was analyzed from three aspects: characteristics of high frequency *C-V*, dark *J-V* characteristics at room temperature, and characteristics of dark *J-V-T*.

（1）The *C-V* relationship between conventional SHJ and solar cells with MoO_x, WO_x, and VO_x as HTLs was measured at 1MHz. It was found that the slope and intercept on the X-axis of the $1/C^2$-V curve of every solar cell were different, which was related to the density of defect states and the built-in potential in interface of device. According to the Schottky-like model, the built-in potential is 0.76, 0.67, and 0.56 V for MoO_x, WO_x, and VO_x based heterojunction solar cell, respectively. Their corresponding contact barrier width is 0.368, 0.277, and 0.188 μm, respectively. It is considered that the density of defect states at the interface of TMO and TMO/Si is the most important factor affecting the bending degree and built-in potential at the interface.

（2）The dark *J-V* curves of conventional SHJ and solar cells with MoO_x, WO_x, and VO_x as HTLs at room temperature were compared. The *J-V* curves were analyzed in four voltage regions using a two-diode model. The relationship between the reverse saturation current density and the ideal diode saturation current density of the four kinds of solar cells is SHJ < MoO_x < WO_x < VO_x, which indicates that the density of defect states at the device interface is SHJ<MoO_x<WO_x<VO_x. This is consistent with the change rule of V_{OC} test results. In the region of 0.15 V＜V＜0.5 V, the ideal factor n_2 of TMO/Si heterostructure is between 3 and 4, which indicates that the novel heterojunction may have a transport mechanism different from the recombination current in the depletion region. In the voltage region of 0.5 V＜V＜0.65 V, the diode factor n_1 is close to 1, which indicates that the carrier transport behavior of the four devices is basically in line with the ideal diode characteristics in this voltage region.

（3）The *J-V-T* of solar cells with MoO_x, WO_x, and VO_x as HTLs was analyzed and simulated. It is found that the current density of the devices has the characteristic of tunneling current in the low voltage region. The factor A_1 does not change with temperature, and the average value of the ideal factor n_1 is large and has no definite value; In the high voltage region, the current density conforms to the ideal diode law, and the ideal factor n_1 is close to 1. Based on the above characteristics, the *J-V-T* curves are simulated by the thermal activation current J_{Te} of electrons (including the representative thermal emission current and thermally assisted tunneling current) and the defect assisted tunneling current (J_{Tu}) of holes. The simulation results are in good agreement with the experimental results. The effective electron barrier height of MoO_x battery is 0.98 eV, which indicates that the surface of crystalline silicon is in strong inversion. The barrier is basically consistent with the built-in potential of *C-V*. The

high barrier makes the device have high V_{OC} potential. The device is a Schottky-like device with high barrier or strong inversion. The low barrier of WO_x and VO_x devices showed that the surface of crystalline silicon was not strong inversion, which may be related to the fermi level pinning caused by the high density of states of interface defects.

Chapter 6. Summary and prospect

6.1 Summary

The novel silicon heterojunction (SHJ) solar cells with MoO_x, WO_x, and VO_x as HTLs have become an important aspect in the future due to their low-cost, simple fabrication process, and higher power conversion efficiency. In this PhD thesis, high-quality MoO_x, WO_x, and VO_x thin films were fabricated by hot-wire oxidation sublimation deposition (HWOSD) method. The fabrication process parameters and material properties were systematically optimized and characterized. The performance of the novel silicon heterojunction solar cell with TMO as HTLs were optimized, and the power conversion efficiency of such cell was increased to 21.10%. The transport mechanism of this kind of solar cell was discussed systematically, which provided guidance on the further development and industrialization of this kind of battery. The main work and results are as follows:

As a method of fabricating high-quality MoO_x, WO_x, and VO_x thin films, hot filament oxidation sublimation deposition has been confirmed with its advantages of low cost, precise control, and easy operation. The optimum technological conditions of TMO film are obtained as follows: the working temperature of molybdenum wire, tungsten wire and vanadium wire are 1050, 1200 and 1200 °C, respectively. The optimal oxygen pressure is 0.2, 1.0 and 1.0 Pa, respectively. Under these conditions, amorphous MoO_x, WO_x, and VO_x thin films with smooth surface and uniform thickness can be deposited on textured substrates by "conformal" deposition. The electronic states of transition metals in TMO films were analyzed by XPS. The x values for MoO_x, WO_x, and VO_x films were 2.94, 2.91 and 2.32, respectively. MoO_x, WO_x, and VO_x films also showed good transmittance, with their average transmittance 97.46% for WO_x films in the range of 300 -1200 nm; the optical band gaps were confirmed as 2.67, 1.86 and 2.19 eV for MoO_x, WO_x, and VO_x, respectively. The conductivity of MoO_x and WO_x films was 2.58×10^{-6} S/cm and 5.14×10^{-7} S/cm, respectively; MoO_x thin films showed good field passivation effect on the i a-Si /c-Si/i a-Si structure, which could increase the minority carrier lifetime to 1.3 ms; KPM result showed that there was obvious contact potential difference between MoO_x and WO_x and n-type silicon. The above results show that TMO thin films fabricated by hot-wire oxidation sublimation deposition have potential as hole selective transport layers for novel SHJ solar cells.

The performance of a novel silicon heterojunction solar cell with MoO_x as HTL was systematically optimized from the aspects of interface passivation layer, film thickness, and annealing process. It was found that i a-Si:H had the best passivation effect on MoO_x/Si heterojunction structure, and the SiO_x layer obtained by UV-O_3

treatment also presented good passivation potential. At the condition pre-annealing-HF process, and MoO_x thickness of 14 nm, the power conversion efficiency of solar cell with MoO_x as HTL reached 21.10% (V_{OC} was 713 mV, J_{SC} was 37.50 mA/cm^2, FF was 78.92%). The performances of a novel SHJ solar cell with MoO_x, WO_x, and VO_x as HTLs was compared. It is found that MoO_x had the best hole selective transport performance. MoO_x and WO_x were used as HTL and antireflection layers in lithographic-free and dopant-free back contact solar cells. The device possessed good photo-electric performance. The parameters are: V_{OC} of 696 mV, J_{SC} of 38.61 mA/cm^2, and FF of 75.31%, and PCE of 20.24%.

The transport mechanism of SHJ solar cells with MoO_x, WO_x, or VO_x as HTLs was studied based on the high frequency *C-V*, dark *J-V* at room temperature, and dark *J-V-T* measurements. By testing the *C-V* relationship of SHJ solar cells with TMO film as HTLs at 1MHz, the contact potential and barrier width of three kinds of solar cells are obtained: 0.76 V and 0.368 μm for MoO_x, 0.67 V and 0.277 μm for WO_x , 0.56 V and 0.277 μm for VO_x solar cell. Comparing the slope of $1/C^2$~V curves of different solar cells, the density of states of interface defects of three solar cells is $MoO_x<WO_x<VO_x$. According to the two-diode model, the dark *J-V* of three solar cells at room temperature was fitted. In the voltage region of $0.4\ V < V < 0.6\ V$, the *J-V* relationship basically conforms to the ideal diode characteristics (ideal factor n~1). In the voltage region of $0.15\ V < V < 0.4\ V$, the three solar cells have larger ideal factors (n = 3.68, 3.62 and 3.76, respectively), which indicates that the transport mechanism of the novel heterojunction may be different from that of the depletion recombination current (n~2). The *J-V-T* of heterojunction solar cells with MoO_x, WO_x, and VO_x as HTLs are analyzed. It was found that in the low voltage region, the current density had the characteristics of tunneling current, that is, the factor A_1 did not change with temperature, and the average value of ideal factor n was large and uncertain; in the high voltage region, the current density conforms to the ideal diode law, and the ideal factor n was close to 1.

The *J-V-T* curves of MoO_x solar cells are simulated by using the thermal activation current J_{Te} to represent the process of electron thermal emission and thermal assisted tunneling, and J_{Tu} to represent the current of hole defect assisted tunneling. The barrier φ_{Bn}= 0.98 eV was obtained at the MoO_x/crystalline silicon heterojunction interface, which indicates that the solar cells would have high V_{OC}. The barrier height obtained by fitting was basically consistent with the built-in potential of MoO_x/Si heterostructure determined by *C-V* measurement ($\varphi_{Bn} \approx V_D+(E_C-E_F)$). Based on the above simulation results, we believe that MoO_x/Si heterojunction is a Schottky-like device with high barrier or strong inversion. The low barrier of WO_x and VO_x devices showed that the surface of crystalline silicon was not strong inversion, which may be related to the fermi level pinning caused by the high density of states of interface defects.

6.2 Problems and future prospects

In this thesis, the fabrication of materials, the performance optimization of solar cells and the transport mechanism of solar cells were studied. At the same time, to further promote the development and application of new heterojunction solar cells, the following aspects are our future efforts:

（2）The development of new high-quality passivation layer materials and structures can be carried out from two aspects: one is to adjust the fabrication parameters and re-design the structure of passivation layer of traditional heterojunction solar cells represented by i a Si:H. For example, by adjusting the fabrication process，a-Si:H/a-Si co-passivation layer structure will be designed, and the defect density of the interface between Si and TMO film will be optimized. The second is to develop a new low-cost passivation layer technology similar to UV-O_3 to achieve high-quality passivation of the device interface, and then improve the performance parameters of the device.

（2）By studying the density and distribution of defect states in TMO films, the Fermi level and work function of TMO films would be adjusted, in order to improve the interface characteristics and inverse barrier height of devices, and further improve the performance parameters of heterojunction solar cells with TMO thin films as HTLs.

Bibliography

[1] Shuzhong W，Donghai W. Energy and the development of human civilization [M], Xi'an Jiaotong University Press, 2018.

[2] Shaozhen X, Meifang Z. Foundation and application of solar cell[M], Beijing: Science Press,2009.

[3] Enke L. Semiconductor physics[M], Electronic Industry Press,2011.

[4] Becquerel A E. Recherches sur les effets de la radiation chimique de la lumiere solaire au moyen des courants electriques[J]. CR Acad. Sci, 1839, 9(145): 1.

[5] Green M A. Photovoltaics: coming of age[C]. IEEE Conference on Photovoltaic Specialists. IEEE, 1990: 1-8.

[6] Chapin D M, Fuller C S, Pearson G L. A new silicon p-n junction photocell for converting solar radiation into electrical power[J]. Journal of Applied Physics, 1954, 25(5): 676-677.

[7] Green M A. Photovoltaic principles[J]. Physica E: Low-dimensional Systems and Nanostructures, 2002, 14(1-2): 11-17.

[8] Best Research-Cell Efficiency Chart, https://www.nrel.gov/pv/cell-efficiency.html

[9] Green M A. Potential for low dimensional structures in photovoltaics[J]. Materials Science and Engineering: B, 2000, 74(1-3): 118-124.

[10] Third generation photovoltaics[M]. BoD–Books on Demand, 2012.

[11] Yoshikawa K, Kawasaki H, Yoshida W, *et al.* Silicon heterojunction solar cell with interdigitated back contacts for a photoconversion efficiency over 26%[J]. Nature energy, 2017, 2(5): 17032.

[12] Yoshikawa K, Yoshida W, Irie T, *et al*. Exceeding conversion efficiency of 26% by heterojunction interdigitated back contact solar cell with thin film Si technology[J]. Solar Energy Materials and Solar Cells, 2017, 173: 37-42.

[13] Shockley W, Queisser H J. Detailed balance limit of efficiency of p-n junction solar cells[J]. Journal of applied physics, 1961, 32(3): 510-519.

[14] Simon M·Sze, Mingkui L, Mingxiang W, Heming Z. Semiconductor device physics and technology[M], Soochow University Press, 2014.

[15] Wald F. Light sensitive electronic devices[P], Google Patents, 1976.

[16] Kingsbury E F, Ohl R S. Photoelectric properties of ionically bombarded silicon[J]. The Bell System Technical Journal, 1952, 31(4): 802-815.

[17] King D L, Buck M E. Experimental optimization of an anisotropic etching process for random texturization of silicon solar cells[R]. Sandia National Labs., Albuquerque, NM (United States), 1991.

[18] Arndt R A, Allison J F, Meulenberg Jr A, et al. Optical properties of the COMSAT non-reflective cell[J]. pvs, 1975: 40-43.

[19] Philipp H R. Optical properties of non-crystalline Si, SiO, SiO_x and SiO_2[J]. Journal of Physics and Chemistry of Solids, 1971, 32(8): 1935-1945.

[20] Aberle A G. Surface passivation of crystalline silicon solar cells: a review[J]. Progress in Photovoltaics: Research and Applications, 2000, 8(5): 473-487.

[21] Schmidt J, Kerr M. Highest-quality surface passivation of low-resistivity p-type silicon using stoichiometric PECVD silicon nitride[J]. Solar Energy Materials and Solar Cells, 2001, 65(1-4): 585-591.

[22] Wang T H, Iwaniczko E, Page M R, *et al*. High-efficiency silicon heterojunction solar cells by HWCVD[C], 2006 IEEE 4th World Conference on Photovoltaic Energy Conference. IEEE, 2006, 2: 1439-1442.

[23] Franklin E, Fong K, McIntosh K, *et al*. Design, fabrication and characterization of a 24.4% efficient interdigitated back contact solar cell[J]. Progress in Photovoltaics: research and applications, 2016, 24(4): 411-427.

[24] Gatz S, Hannebauer H, Hesse R, *et al*. 19.4%-efficient large-area fully screen-printed silicon solar cells[J]. Physica status solidi (RRL) – Rapid Research Letters, 2011, 5(4): 147-149.

[25] Kaminski A, Vandelle B, Fave A, et al. Aluminium BSF in silicon solar cells[J]. Solar energy materials and solar cells, 2002, 72(1-4): 373-379.

[26] Narasinha S, Rohatgi A. Optimized aluminum back surface field techniques for silicon solar cells[C], Conference Record of the Twenty Sixth IEEE Photovoltaic Specialists Conference-1997. IEEE, 1997: 63-66.

[27] Narasimha S, Rohatgi A, Weeber A W. An optimized rapid aluminum back surface field technique for silicon solar cells[J]. IEEE Transactions on Electron Devices, 1999, 46(7): 1363-1370.

[28] Pujari N S, Cellere G, Falcon T. International Technology Roadmap for Photovoltaic (ITRPV) Results 2017 including maturity report 2018 Ninth Edition September 2018[C], ITRPV. 2018.

[29] Green M A. The passivated emitter and rear cell (PERC): From conception to mass production[J]. Solar Energy Materials and Solar Cells, 2015, 143: 190-197.

[30] Blakers A. Development of the PERC solar cell[J]. IEEE Journal of Photovoltaics, 2019, 9(3): 629-635.

[31] Dullweber T, Schmidt J. Industrial silicon solar cells applying the passivated emitter and rear cell (PERC) concept—A review[J]. IEEE journal of photovoltaics, 2016, 6(5): 1366-1381.

[32] Min B, Müller M, Wagner H, et al. A roadmap toward 24% efficient PERC solar cells in industrial mass production[J]. IEEE Journal of Photovoltaics, 2017, 7(6): 1541-1550.

[33] Allen T G, Bullock J, Yang X, et al. Passivating contacts for crystalline silicon solar cells[J]. Nature Energy, 2019: 1-15.

[34] Lammert M D, Schwartz R J. The interdigitated back contact solar cell: A silicon solar cell for use in concentrated sunlight[J]. IEEE Transactions on Electron Devices, 1977, 24(4): 337-342.

[35] McIntosh K R, Cudzinovic M J, Smith D D, et al. The choice of silicon wafer for the production of low-cost rear-contact solar cells[C]. 3rd World Conference on Photovoltaic Energy Conversion, 2003. Proceedings of. IEEE, 2003, 1: 971-974.

[36] Masuko K, Shigematsu M, Hashiguchi T, *et al.* Achievement of more than 25% conversion efficiency with crystalline silicon heterojunction solar cell[J]. IEEE Journal of Photovoltaics, 2014, 4(6): 1433-1435.

[37] Jensen N, Hausner R M, Bergmann R B, *et al*. Optimization and characterization of amorphous/crystalline silicon heterojunction solar cells[J]. Progress in Photovoltaics: Research and Applications, 2002, 10(1): 1-13.

[38] Kobayashi T, Kawagishi T, Fukumuro N. 26th European Photovoltaic Solar Energy Conference and Exhibition Hamburg[J]. Germany, September, 2011: 5-8.

[39] Goldbach H D, Bink A, Schropp R E I. Bifacial Silicon Heterojunction Solar Cell with Deposited Back Surface Field[J]. MRS Online Proceedings Library Archive, 2005, 862.

[40] Battaglia C, Yin X, Zheng M, et al. Hole selective MoO_x contact for silicon solar cells[J]. Nano letters, 2014, 14(2): 967-971.

[41] Dréon J, Jeangros Q, Cattin J, *et al*. 23.5%-efficient silicon heterojunction silicon solar cell using molybdenum oxide as hole-selective contact[J]. Nano Energy, 2020, 70: 104495.

[42] Geissbühler J, Werner J, Martin de Nicolas S, *et al*. 22.5% efficient silicon heterojunction solar cell with molybdenum oxide hole collector[J]. Applied Physics Letters, 2015, 107(8): 081601.

[43] Bullock J, Hettick M, Geissbühler J, *et al*. Efficient silicon solar cells with dopant-free asymmetric heterocontacts[J]. Nature Energy, 2016, 1(3): 1-7.

[44] Mews M, Lemaire A, Korte L. Sputtered tungsten oxide as hole contact for silicon heterojunction solar cells[J]. IEEE Journal of photovoltaics, 2017, 7(5): 1209-1215.

[45] Qiu K, Xie Q, Qiu D, *et al*. Power-loss analysis of a dopant-free ZnS/p-Si heterojunction solar cell with WO_3 as hole-selective contact[J]. Solar Energy, 2018, 165: 35-42.

[46] Bivour M, Temmler J, Steinkemper H, et al. Molybdenum and tungsten oxide: High work function wide band gap contact materials for hole selective contacts of silicon solar cells[J]. Solar Energy Materials and Solar Cells, 2015, 142: 34-41.

[47] Almora O, Gerling L G, Voz C, et al. Superior performance of V_2O_5 as hole selective contact over other transition metal oxides in silicon heterojunction solar cells[J]. Solar Energy Materials and Solar Cells, 2017, 168: 221-226.

[48] Zilberberg K, Trost S, Schmidt H, et al. Solution processed vanadium pentoxide as charge extraction layer for organic solar cells[J]. Advanced Energy Materials, 2011, 1(3): 377-381.

[49] Raiford J A, Belisle R A, Bush K A, *et al.* Atomic layer deposition of vanadium oxide to reduce parasitic absorption and improve stability in n–i–p perovskite solar cells for tandems[J]. Sustainable Energy & Fuels, 2019, 3(6): 1517-1525.

[50] Yang X, Guo J, Zhang Y, *et al.* Hole-selective NiO:Cu contact for NiO/Si heterojunction solar cells[J]. Journal of Alloys and Compounds, 2018, 747: 563-570.

[51] Hsu F H, Wang N F, Tsai Y Z, *et al*. Enhanced carrier collection in p-$Ni_{1-x}O$:Li/n-Si heterojunction solar cells using LiF_x/Al electrodes[J]. Thin Solid Films, 2014, 573: 159-163.

[52] Shen R, Liu M, Zhou Y, *et al.* PEDOT: PSS/SiNWs hybrid solar cells with an effective nanocrystalline silicon back surface field layer by low temperature catalytic diffusion[J]. Solar RRL, 2017, 1(11): 1700133.

[53] Jäckle S, Mattiza M, Liebhaber M, *et al.* Junction formation and current transport mechanisms in hybrid n-Si/PEDOT: PSS solar cells[J]. Scientific reports, 2015, 5: 13008.

[54] Li X, Zhu H, Wang K, *et al*. Graphene-on-silicon Schottky junction solar cells[J]. Advanced materials, 2010, 22(25): 2743-2748.

[55] Li X, Lv Z, Zhu H. Carbon/silicon heterojunction solar cells: state of the art and prospects[J]. Advanced Materials, 2015, 27(42): 6549-6574.

[56] Wang Z, Yang Y, Zhang L, *et al*. Modulation-doped ZnO as high performance electron-selective layer for efficient silicon heterojunction solar cells[J]. Nano Energy, 2018, 54: 99-105.

[57] Zhong S, Morales-Masis M, Mews M, *et al*. Exploring co-sputtering of ZnO:Al and SiO_2 for efficient electron-selective contacts on silicon solar cells[J]. Solar Energy Materials and Solar Cells, 2019, 194: 67-73.

[58] Ding J, Zhou Y, Dong G, *et al*. Solution - processed ZnO as the efficient passivation and electron selective layer of silicon solar cells[J]. Progress in Photovoltaics: Research and Applications, 2018, 26(12): 974-980.

[59] Wan Y, Samundsett C, Bullock J, *et al*. Conductive and stable magnesium oxide electron-selective contacts for efficient silicon solar cells[J]. Advanced Energy Materials, 2017, 7(5): 1601863.

[60] Bullock J, Wan Y, Hettick M, *et al*. Dopant-Free Partial Rear Contacts Enabling 23% Silicon Solar Cells[J]. Advanced Energy Materials, 2019, 9(9): 1803367.

[61] Liu Y, Zhang J, Wu H, *et al*. Low-temperature synthesis TiO_x passivation layer for organic-silicon heterojunction solar cell with a high open-circuit voltage[J]. Nano Energy, 2017, 34: 257-263.

[62] Yang X, Zheng P, Bi Q, *et al*. Silicon heterojunction solar cells with electron selective TiO_x contact[J]. Solar Energy Materials and Solar Cells, 2016, 150: 32-38.

[63] Battaglia C, De Nicolas S M, De Wolf S, *et al*. Silicon heterojunction solar cell with passivated hole selective MoO_x contact[J]. Applied Physics Letters, 2014, 104(11): 113902.

[64] Noce M D, Bobeico E, Lancellotti L, *et al*. MoO_x as hole-selective collector in p-type Si heterojunction solar cells[C]. AIP Conference Proceedings. AIP Publishing LLC, 2018, 1999(1): 040006.

[65] Shi J, Shen L, Liu Y, *et al*. MoO_x modified ITO/a-Si:H(p) contact for silicon heterojunction solar cell application[J]. Materials Research Bulletin, 2018, 97: 176-181.

[66] Kamioka T, Hayashi Y, Isogai Y, *et al*. Effect of ITO Capping Layer on Interface Workfunction of MoO x in ITO/MoO_x/SiO_2/Si Contacts[C]. 2018 IEEE 7th World Conference on Photovoltaic Energy Conversion (WCPEC). IEEE, 2018: 2024-2026.

[67] Sacchetto D, Jeangros Q, Christmann G, *et al*. ITO/MoO_x/a-Si: H(i) hole-selective contacts for silicon heterojunction solar cells: degradation mechanisms and cell integration[J]. IEEE Journal of Photovoltaics, 2017, 7(6): 1584-1590.

[68] Gao M, Chen D, Han B, *et al*. Bifunctional Hybrid a-SiO_x(Mo) Layer for Hole-Selective and Interface Passivation of Highly Efficient MoO_x/a-SiO_x(Mo)/n-Si Heterojunction Photovoltaic Device[J]. ACS applied materials & interfaces, 2018, 10(32): 27454-27464.

[69] Bivour M, Macco B, Temmler J, *et al*. Atomic layer deposited molybdenum oxide for the hole-selective contact of silicon solar cells[J]. Energy Procedia, 2016, 92: 443-449.

[70] Ziegler J, Mews M, Kaufmann K, *et al.* Plasma-enhanced atomic-layer-deposited MoO_x emitters for silicon heterojunction solar cells[J]. Applied Physics A, 2015, 120(3): 811-816.

[71] Mohamed S H, Venkataraj S. Thermal stability of amorphous molybdenum trioxide films prepared at different oxygen partial pressures by reactive DC magnetron sputtering[J]. Vacuum, 2007, 81(5): 636-643.

[72] Pachlhofer J M, Jachs C, Franz R, *et al.* Structure evolution in reactively sputtered molybdenum oxide thin films[J]. Vacuum, 2016, 131: 246-251.

[73] Pachlhofer J M, Martin-Luengo A T, Franz R, *et al.* Non-reactive dc magnetron sputter deposition of Mo-O thin films from ceramic MoO_x targets[J]. Surface and Coatings Technology, 2017, 332: 80-85..

[74] Parashar P K, Komarala V K. Sputter deposited sub-stochiometric MoO_x thin film as hole-selective contact layer for silicon-based heterojunction devices[J]. Thin Solid Films, 2019, 682: 76-81.

[75] Sivakumar R, Gopalakrishnan R, Jayachandran M, *et al.* Characterization on electron beam evaporated α-MoO_3 thin films by the influence of substrate temperature[J]. Current Applied Physics, 2007, 7(1): 51-59.

[76] Hammond S R, Meyer J, Widjonarko N E, *et al.* Low-temperature, solution-processed molybdenum oxide hole-collection layer for organic photovoltaics[J]. Journal of Materials Chemistry, 2012, 22(7): 3249-3254.

[77] Tong J, Wan Y, Cui J, *et al.* Solution-processed molybdenum oxide for hole-selective contacts on crystalline silicon solar cells[J]. Applied surface science, 2017, 423: 139-146.

[78] Lu C, Prakoso A B, Li Z. Investigation of solution processed molybdenum oxide as selective contacts for silicon solar cells application[J]. Materials Chemistry and Physics, 2019, 236: 121779.

[79] Mews M, Korte L, Rech B. Oxygen vacancies in tungsten oxide and their influence on tungsten oxide/silicon heterojunction solar cells[J]. Solar Energy Materials and Solar Cells, 2016, 158: 77-83.

[80] Lee C Y, Zhang T, Khoo K, *et al.* Thermal stability of novel hole-selective contacts for silicon wafer solar cells[J].

[81] Sun T, Wang R, Liu R, *et al*. Investigation of MoO_x/n-Si strong inversion layer interfaces via dopant-free heterocontact[J]. Physica status solidi (RRL)-Rapid Research Letters, 2017, 11(7): 1700107.

[82] Chen D, Gao M, Wan Y, *et al*. Electronic structure of molybdenum-involved amorphous silica buffer layer in MoO_x/n-Si heterojunction[J]. Applied Surface Science, 2019, 473: 20-24.

[83] Messmer C, Bivour M, Schön J, *et al*. Requirements for efficient hole extraction in transition metal oxide-based silicon heterojunction solar cells[J]. Journal of Applied Physics, 2018, 124(8): 085702.

[84] García-Hernansanz R, García-Hemme E, Montero D, *et al*. Transport mechanisms in silicon heterojunction solar cells with molybdenum oxide as a hole transport layer[J]. Solar energy materials and solar cells, 2018, 185: 61-65.

[85] Song W, Fan X, Xu B, *et al*. All-Solution-Processed Metal-Oxide-Free Flexible Organic Solar Cells with Over 10% Efficiency[J]. Advanced Materials, 2018, 30(26): 1800075.

[86] Liu M, Johnston M B, Snaith H J. Efficient planar heterojunction perovskite solar cells by vapour deposition[J]. Nature, 2013, 501(7467): 395-398.

[87] Ye Q, Zhao Y, Mu S, *et al*. Cesium lead inorganic solar cell with efficiency beyond 18% via reduced charge recombination[J]. Advanced Materials, 2019, 31(49): 1905143.

[88] Zhang W, Li Y, Liu X, *et al*. Ethyl acetate green antisolvent process for high-performance planar low-temperature SnO_2-based perovskite solar cells made in ambient air[J]. Chemical Engineering Journal, 2020, 379: 122298.

[89]Bardwell,J.,The Evolution of Silicon Wafer Cleaning Technology[J]. Electrochemical Society Interface, 2017. 26(2): p. 14-14.

[90] Kern W. The evolution of silicon wafer cleaning technology[J]. Journal of the Electrochemical Society, 1990, 137(6): 1887.

[91] Chavali R V K, De Wolf S, Alam M A. Device physics underlying silicon heterojunction and passivating-contact solar cells: A topical review[J]. Progress in Photovoltaics: Research and Applications, 2018, 26(4): 241-260..

[92] Song Y J, Park M R, Guliants E, *et al*. Influence of defects and band offsets on carrier transport mechanisms in amorphous silicon/crystalline silicon heterojunction solar cells[J]. Solar energy materials and solar cells, 2000, 64(3): 225-240.

[93] Hussein R, Borchert D, Grabosch G, *et al*. Dark I-V-T measurements and characteristics of (n) a-Si/(p) c-Si heterojunction solar cells[J]. Solar energy materials and solar cells, 2001, 69(2): 123-129.

[94] Li F, Zhou Y, Yang Y, et al. Silicon Heterojunction Solar Cells with MoO_x Hole-Selective Layer by Hot-Wire Oxidation Sublimation Deposition[J]. Solar RRL, 2020, 4(3): 1900514.

[95] Zeng R, Liu H, Shen W. A facile and controllable electrochemically fabricated nonstoichiometric MoO_x film for novel opto-electronic devices[J]. Journal of Micromechanics and Microengineering, 2019, 29(6): 065012.

[96] Demeter M, Neumann M, Reichelt W. Mixed-valence vanadium oxides studied by XPS[J]. Surface Science, 2000, 454: 41-44.

[97] Swanepoel R. Determination of the thickness and optical constants of amorphous silicon[J]. Journal of Physics E: Scientific Instruments, 1983, 16(12): 1214.

[98] Sindhu S, Sanghi S, Agarwal A, *et al.* Structural, optical, physical and electrical properties of $V_2O_5{\cdot}SrO{\cdot}B_2O_3$ glasses[J]. Spectrochimica Acta Part A: Molecular and Biomolecular Spectroscopy, 2006, 64(1): 196-204.

[99] Mohamed S H, Anders A. Structural, optical, and electrical properties of WO_x (Ny) films deposited by reactive dual magnetron sputtering[J]. Surface and Coatings Technology, 2006, 201(6): 2977-2983.

[100] Anwar M, Hogarth C A. Optical properties of amorphous thin films of MoO_3 deposited by vacuum evaporation[J]. Physica status solidi (a), 1988, 109(2): 469-478.

[101] Luo Z, Wu Z, Wang T, et al. Comparison of the optical responses of O-poor and O-rich thermochromic VO_x films during semiconductor-to-metal transition[J]. Journal of Physics and Chemistry of Solids, 2012, 73(9): 1122-1126.

[102] Rajagopal S, Nataraj D, Khyzhun O Y, *et al*. Systematic synthesis and analysis of change in morphology, electronic structure and photoluminescence properties of pyrazine intercalated MoO_3 hybrid nanostructures[J]. CrystEngComm, 2011, 13(7): 2358-2368.

[103] Chelvanathan P, Rahman K S, Hossain M I, *et al*. Growth of MoO_x nanobelts from molybdenum bi-layer thin films for thin film solar cell application[J]. Thin Solid Films, 2017, 621: 240-246.

[104] Dieterle M, Weinberg G, Mestl G. Raman spectroscopy of molybdenum oxides Part I. Structural characterization of oxygen defects in MoO_{3-x} by UV/VIS, Raman spectroscopy and X-ray diffraction[J]. Physical Chemistry Chemical Physics, 2002, 4(5): 812-821.

[105] Wang X G, Jang Y S, Yang N H, *et al*. XPS and XRD study of the electrochromic mechanism of WO_x films[J]. Surface and Coatings Technology, 1998, 99(1-2): 82-86.

[106] Horynová E, Romanyuk O, Horák L, *et al*. Optical characterization of low temperature amorphous MoO_x, WO_x, and VO_x prepared by pulsed laser deposition[J]. Thin Solid Films, 2020, 693: 137690.

[107] Liu M, Zhou Y, Dong G, *et al*. SnO_2/Mg combination electron selective transport layer for Si heterojunction solar cells[J]. Solar Energy Materials and Solar Cells, 2019, 200: 109996.

[108] Kita K, Toriumi A. Origin of electric dipoles formed at high-k/SiO_2 interface[J]. Applied Physics Letters, 2009, 94(13): 132902.

[109] Kröger M, Hamwi S, Meyer J, et al. P-type doping of organic wide band gap materials by transition metal oxides: A case-study on Molybdenum trioxide[J]. Organic Electronics, 2009, 10(5): 932-938.

[110] Meyer J, Kröger M, Hamwi S, et al. Charge generation layers comprising transition metal-oxide/organic interfaces: Electronic structure and charge generation mechanism[J]. Applied Physics Letters, 2010, 96(19): 93.

[111] Meyer J, Zilberberg K, Riedl T, et al. Electronic structure of Vanadium pentoxide: An efficient hole injector for organic electronic materials[J]. Journal of Applied Physics, 2011, 110(3): 033710..

[112] Simon M·Sze, Guojue W, Li G, Ruizhi Z. Semiconductor device physics[M]. Xi'an Jiaotong University Press, 2008

[113] Chavali R V K, Wilcox J R, Ray B, et al. Correlated nonideal effects of dark and light IV characteristics in a-Si/c-Si heterojunction solar cells[J]. IEEE Journal of Photovoltaics, 2014, 4(3): 763-771.

[114] Fengzhen L, Jiedong C, Qunfang Z. Dark I-V characteristics and transport mechanism of nanosilicon/crystalline silicon heterojunction cells[J]. Journal of Semiconductors,2008,29(3)

Appendices

Appendix A. Paper Ⅰ

Appendix B. Paper Ⅱ

Appendix A. Paper Ⅰ

Solar RRL
www.solar-rrl.com
Check for updates

Silicon Heterojunction Solar Cells with MoO_x Hole-Selective Layer by Hot Wire Oxidation–Sublimation Deposition

Fengchao Li, Yurong Zhou, Ying Yang, Gangqiang Dong, Yuqin Zhou, Fengzhen Liu,* and Donghong Yu*

In this article, a novel hot wire oxidation–sublimation deposition (HWOSD) technique, as an optional technology, is developed to prepare molybdenum oxide (MoO_x) thin films. Silicon heterojunction (SHJ) solar cells with the HWOSD MoO_x as a hole-selective transport layer (HSL) are fabricated. A power conversion efficiency up to 21.10% is achieved on a champion SHJ solar cell using a 14 nm MoO_x layer as the HSL. Dark current density–voltage–temperature (*J–V–T*) characteristics of the SHJ solar cell are measured at temperatures ranging from 200 to 380 K. Transport processes including thermionic emission of electrons over the potential barrier and quantum-assisted tunneling of holes through the gap states in the MoO_x layer are used to fit the *J–V* curves of the MoO_x/n-c-Si heterojunction. The investigation of the transport mechanisms provides a better understanding of the characteristics of the novel SHJ solar cells and it is helpful to fully demonstrate the potential of such kinds of solar cells in the future.

1. Introduction

More and more attention has been paid to the novel silicon heterojunction (SHJ) solar cells by making use of metal oxides to replace the conventional doped hydrogenated amorphous Si (a-Si:H) thin films as the carrier-selective transport layers.[1–4] Due to the wide-bandgap nature, optional work functions, and relatively simple fabrication techniques related to the metal oxides, the novel SHJ solar cells show great potential to further improve the efficiency and reduce the cost of c-Si-based solar cells.[2,5] Differences between the work functions of the metal oxides and Fermi levels of the c-Si lead to a large energy band bending of the c-Si near the interface, which allows only one type of carrier to pass through and inhibits carrier recombination at the interface.[6] Some metal oxides with high work functions, such as MoO_x,[2,3] VO_x,[7] WO_x,[8] NiO_x,[9,10] and CuO_x,[11,12] can provide good hole-selective transport when they form heterocontacts with c-Si. Similarly, some metal oxides with low work functions, such as TiO_x,[9,13] MgO_x,[14,15] and ZnO,[16] can be used as the electron-selective transport layers instead of n-type a-Si:H in c-Si solar cells.

Based on such a factor that it is more difficult to obtain high-quality p-type a-Si:H than n-type a-Si:H, people are more eager to find a suitable substitute for p-type a-Si:H in SHJ solar cells. In recent years, remarkable achievements have been made on the SHJ solar cells using molybdenum oxide (MoO_x) with wide bandgap (3.0–3.3 eV) and high work function (>6 eV) as the hole-selective transport layer (HSL) to replace the p-type a-Si:H thin film.[4,17–19] Various techniques, such as thermal evaporation,[2–4] electron beam evaporation,[15,20] atomic layer deposition,[21] sputtering,[22] and solution-processed method,[5] are available for the preparation of MoO_x thin films. By using thermal evaporated MoO_x thin films as the HSL, SHJ solar cells with power conversion efficiencies up to 22.5% were fabricated by Geissbuhler et al.[2] Yu et al.[15] prepared the MoO_x films using electron beam evaporation and achieved an efficiency of 14.2% on a plane SHJ solar cell with the structure of MoO_x/n-type c-Si/MgO. A solution-processed method was reported by Tong et al.[5] to form the MoO_x layers by spin coating hydrogen molybdenum bronze solution on crystalline silicon wafer surfaces. The developments of the novel heterojunction solar cells with the MoO_x HSL are very exciting and the efficiency is expected to be further improved in the future.

To promote the commercialization of the novel SHJ solar cells in the future, a simple and scalable production technique capable of fabricating high-quality MoO_x thin films is needed.

Dr. F. Li, Dr. Y. Zhou, Y. Yang, Dr. G. Dong, Prof. Y. Zhou, Prof. F. Liu
Center of Materials Science and Optoelectronics Engineering & College of Materials Science and Opto-Electronic Technology
University of Chinese Academy of Sciences
Beijing 100049, China
E-mail: zhouyurong@ucas.ac.cn; liufz@ucas.ac.cn

Dr. F. Li, Prof. F. Liu
Sino-Danish College
University of Chinese Academy of Sciences
Beijing 100190, China

Dr. F. Li, Prof. D. Yu
Department of Chemistry and Bioscience
Aalborg University
Aalborg DK-9220, Denmark

Prof. D. Yu
Sino-Danish Center for Education and Research
Aarhus DK-8000, Denmark

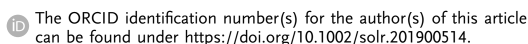

DOI: 10.1002/solr.201900514

© 2020 WILEY-VCH Verlag GmbH & Co. KGaA, Weinheim

Different from the methods mentioned earlier, in this work, we provide a new alternative technique for the fabrication of the MoO_x film. We developed a hot wire oxidation–sublimation deposition (HWOSD) technique to fabricate amorphous molybdenum oxide thin films with good photoelectric properties. The SHJ solar cells were fabricated making use of the HWOSD MoO_x as the HSL. Investigations and optimizations of the device structure, interface passivation, and annealing process were carried out. A power conversion efficiency up to 21.10% was achieved for a champion SHJ solar cell with the structure of Ag/ indium tin oxide (ITO)/n-type a-Si:H/ intrinsic a-Si:H/n-type textured c-Si/intrinsic a-Si:H/MoO_x/Ag. Dark J–V–T characteristics were analyzed to understand the transport mechanisms of the novel heterojunction solar cells.

2. Preparation of MoO_x Thin Films by Novel HWOSD Technique

A schematic diagram of the HWOSD technique is shown in **Figure 1**. In a deposition chamber with oxygen atmosphere, molybdenum wires are electrically heated to a high temperature. MoO_x molecules are generated on the surface of the hot molybdenum wires and are sublimated directly into the chamber. The MoO_x molecules adsorb, diffuse, coalesce, and finally form the MoO_x thin films on the substrate. During the deposition, the substrate temperature was lower than 70 °C. The molybdenum wires with a purity of 99.995% and a diameter of 1 mm were used. The hot wire temperature, oxygen flow rate, and deposition pressure were optimized to be 1095 ± 5 °C, 4 sccm, and 0.2 Pa, respectively. Under the optimal condition, the deposition rate of the MoO_x thin films is about 9 nm min^{-1}.

The novel HWOSD technique is attractive in many ways. It is somewhat similar to the well-known hot wire chemical vapor deposition technology.[23] Some of the advantages of this technique make it very easy to scale up for industrialization. Scaling to large areas merely requires an increase in number and/or length of molybdenum wires along with a proportionally larger supply of oxygen gas. The deposition rate of MoO_x film using HWOSD technique can be well adjusted by varying the oxygen pressure and/or the temperature of the molybdenum wires. Powder spattering, which is easy to occur during thermal evaporation,[2–4] can be avoided. Next, conformal coating on any type of surface shape is possible for the HWOSD technique due to the gas phase and surface diffusion of MoO_x molecules, which is conducive to the formation of good coverage on textured silicon substrates. Furthermore, the HWOSD technique is based on the characteristic of the higher melting point of molybdenum and lower boiling point of molybdenum oxide. Therefore, it is suitable to use to fabricate other metal oxides with similar characteristics, such as WO_x and VO_x.

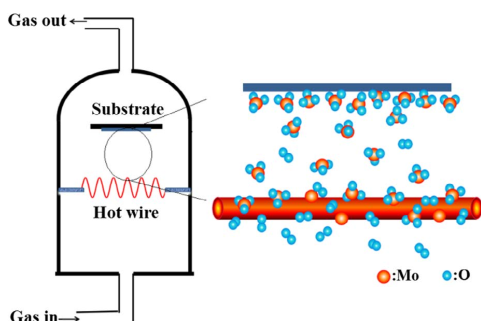

Figure 1. Schematic diagram of HWOSD technique.

3. Results and Discussion

3.1. Characteristics of the MoO_x Thin Films Prepared by HWOSD

During the process of HWOSD, hot wire temperature and oxygen pressure are two important parameters affecting the optoelectronic properties of the deposited MoO_x thin films. Under the optimized hot wire temperature (1095 ± 5 °C) and oxygen pressure (0.2 Pa), an average transmittance of 94.2% in the wavelength range of 400–1100 nm can be obtained on a 15 nm MoO_x thin film. (The effect of the oxygen pressure on the transmittance of the MoO_x thin films is given in Figure S1, Supporting Information.) The dark conductivity of the optimized MoO_x film is 1.6×10^{-6} S cm^{-1}. The XRD spectrum shows that the HWOSD MoO_x thin film is in an amorphous structure (Figure S2, Supporting Information).

Figure 2 shows the XPS spectrum of the Mo 3d core level in MoO_x thin film. The two major peaks, with binding energies of 233.3 and 236.4 eV, correspond to the Mo^{6+} $3d_{5/2}$ and $3d_{3/2}$, respectively.[5,19] And the minor ones centered at 232.0 and 235.0 eV can be attributed to Mo^{5+}. The estimated O/Mo atomic ratio of the MoO_x thin film is about 2.94, which closes to the stoichiometric ratio of 3. The relatively high oxygen content in the MoO_x thin films usually leads to a high work function.[18,19]

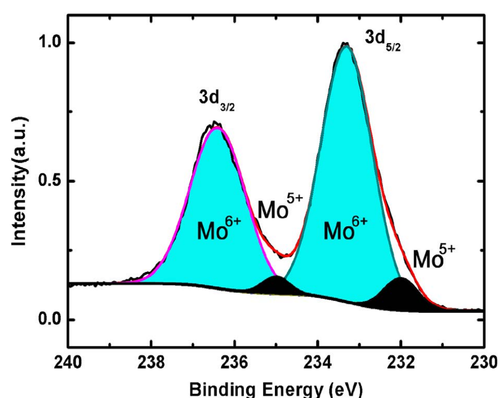

Figure 2. The Mo 3d core level XPS spectrum for a MoO_x film fitted with multiple Voigt peaks (shaded areas) to quantify the contribution of different oxidation states.

© 2020 WILEY-VCH Verlag GmbH & Co. KGaA, Weinheim

3.2. Surface Morphologies and Passivation Effect of MoO_x on Si Substrates

SEM images of the MoO_x thin films deposited on Si wafers are shown in **Figure 3**. Figure 3a,b shows the top-view and cross-sectional SEM images of the MoO_x films on polished Si substrates, respectively. It can seem that compact MoO_x films with high thickness uniformity were formed on the polished Si substrates by using HWOSD. The SEM images of pyramid-shaped silicon surfaces covered with HWOSD MoO_x thin films are shown in Figure 3c,d. Conformal coverage of the MoO_x thin films on the random pyramids is realized. The nice coverage characteristics can be confirmed by the elemental energy dispersive spectrometer (EDS) mappings of O and Mo (Figure S3, Supporting Information).

The effective lifetimes for n-type CZ Si wafers sandwiched between intrinsic a-Si:H (i a-Si:H) thin film or i a-Si:H/MoO_x combination layer as a function of excess carrier density were measured and compared (Figure S4, Supporting Information). The i a-Si:H/MoO_x combination layer passivated sample shows enhanced lifetimes in the whole carrier injection concentration range of 7×10^{14}–1×10^{16} cm^{-3} and a maximum lifetime up to 1.3 ms is achieved. The recombination current density (J_0) and the implied open circuit voltage (iV_{oc}) under 1 sun illumination are 26 fA cm^{-2} and 697 mV, respectively. The results demonstrate the effective field passivation effect of the molybdenum oxide film on the surface of c-Si. The high work function of the MoO_x layer produces a large band bending of the n-type c-Si surface and thus reduces the surface recombination effectively.

3.3. Optimization of the SHJ Solar Cells with MoO_x as HSL

The structure of the heterojunction solar cells with MoO_x HSL is shown in **Figure 4**a. The illuminated side (front side) structure of the devices is set to be Ag grid/ITO/n-type a-Si:H/ i a-Si:H. The rear side structure is Ag/MoO_x/i a-Si:H. The main reason for putting the MoO_x HSL on the back side of the solar cell is to avoid the ITO layer sputtering and make the MoO_x contact directly with the Ag electrode. In this case, the deterioration of the MoO_x thin film related to the ITO sputtering process[2,24] can be avoided and the role of the HWOSD MoO_x HSL in the performance of the SHJ solar cells can be well demonstrated. Of course, without the ITO layer, the SHJ solar cell fabrication process becomes more concise. Another consideration is that, with this configuration, the novel solar cell can be compared with

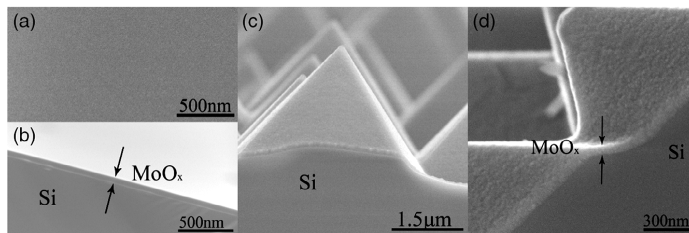

Figure 3. a) Top-view SEM image of MoO_x (25 nm) on polished Si substrate. b) Cross-sectional SEM image of MoO_x (70 nm) on polished Si substrate. c,d) SEM images of MoO_x (70 nm) on textured Si wafers.

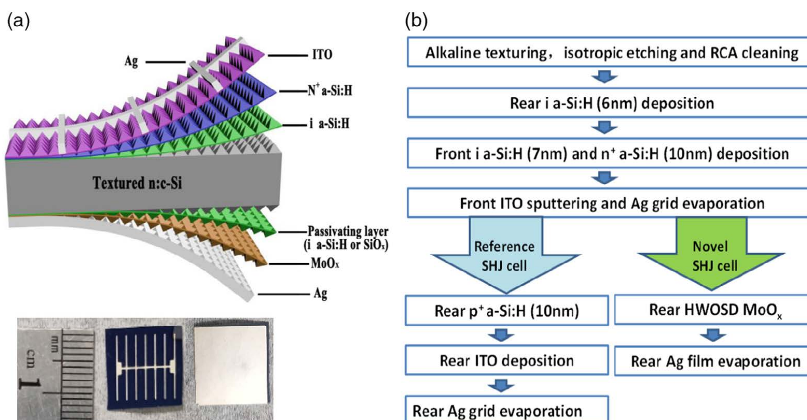

Figure 4. a) Cross-sectional schematic of the heterojunction solar cells with MoO_x HSL and photographs of the front and back of the HSL device. b) Process flow chart for the fabrication of the novel and reference SHJ solar cells.

© 2020 WILEY-VCH Verlag GmbH & Co. KGaA, Weinheim

our reference SHJ devices. Generally, high-quality n-type a-Si:H thin films are easier to realize than p-type a-Si:H. Therefore, using the n-type a-Si:H thin film in the front side of the SHJ solar cells is beneficial to achieve higher efficiency. The process flow chart for the fabrication of the novel and reference SHJ solar cells is shown in Figure 4b.

Effective interface passivation plays a critical role in increasing the performance of the SHJ solar cells. We found that the SHJ solar cells with a MoO_x HSL directly deposited on Si substrates usually show much worse performance than a traditional SHJ solar cell, implying a serious recombination of photogenerated carriers at the MoO_x/c-Si interface. Different passivation layers, including intrinsic a-Si:H thin film, UV/O_3 photo-oxidized SiO_x, and the combination of a-Si:H and SiO_x, were adopted to passivate the c-Si substrates before the deposition of MoO_x (Table S1, Supporting Information). Compared with the solar cell without any passivation layer, all the passivation methods we tried improved the performances of the solar cells to some extent. Among them, the intrinsic a-Si:H layer deposited using plasma enhanced chemical vapor deposition (PECVD) exhibits the best passivation effect. The UV/O_3 treatment is quite simple compared with the a-Si:H deposition technique. However, the passivation effect of the UV/O_3 photo-oxidized SiO_x layer is less than satisfactory. Similar to what is reported in the literature,[2] we also noted that the SiO_x layer may lead to the deterioration of the annealing performance of a SHJ solar cell with a MoO_x HSL, which will be discussed later. Therefore, we used the PECVD a-Si:H as the passivation layer at present stage.

Influence of the MoO_x HSL thickness (10–71 nm) on the photovoltaic parameters of the SHJ solar cells was investigated (Figure S5, Supporting Information). In the case that the thickness of the MoO_x HSL is too small (e.g., 10 nm), the space charge region or the inversion layer near the c-Si surface may not be well formed, which is not favorable for the separation and collection of the photogenerated carriers. However, as for the condition of excessive MoO_x thickness (>14 nm), the consequentially enhanced recombination in the MoO_x layer leads to reduced carrier collection and then decline of the open circuit voltage (V_{oc}) and a rapid drop in the short circuit current density (J_{sc}). Despite the similar behavior as V_{oc} and J_{sc} under very small or very large thickness, the fill factor (FF) was kept at a relatively high value for MoO_x thickness between 14 and 55 nm due to the almost invariable series resistance. Considering all the photovoltaic parameters of the series of SHJ solar cells, we determined an optimal MoO_x thickness of 14 nm. A power conversion efficiency of 18.11% was achieved for the SHJ solar cell with a 14 nm MoO_x as the HSL.

Postannealing as a low-temperature step with temperatures from 150 to 350 °C is a typical process needed for the fabrication of conventional SHJ solar cells, which can improve the overall performance of the devices. However, postannealing tends to show a bad effect on the SHJ solar cells with metal oxides (such as MoO_x, WO_x, VO_x) as the HSL.[2,6] Many researches related to the degradation mechanism have been conducted. It was reported that the work functions of metal oxides and the characteristics of the interface between the metal oxides and the c-Si are changed by postannealing.[25] Essig et al.[26] showed that effusion of hydrogen from the adjacent layers is a likely cause for the degradation of the SHJ solar cells with MoO_x HSL contacts. They suggested a pre-MoO_x-deposition annealing step to reduce the hydrogen content of the a-Si:H layer and allow a high FF to be obtained. More research on the annealing process of SHJ solar cells with MoO_x HSL is still needed.

In this article, an investigation on the annealing process of SHJ solar cells with the MoO_x HSL was conducted and the influences of different annealing processes on the V_{oc} and FF of the SHJ solar cells are shown in **Figure 5**a. As a reference, the V_{oc} and FF of an as-prepared SHJ solar cell without any annealing process are included as shown by red symbols. Similarly the literature, annealing after the fabrication of the whole device (postannealing, 190 °C, 5 min) leads to deterioration in device performance (green symbols). MoO_x annealing (blue symbols) in Figure 5a refers to an annealing process that was conducted just after the preparation of MoO_x and before the deposition of the silver electrode. V_{oc} and FF of the solar cell are further reduced with MoO_x annealing compared with the postannealing process, indicating serious damage to the exposed MoO_x layer was caused by the MoO_x-annealing process. To avoid the annealing damage to the MoO_x layer, an annealing process was carried out before the preparation of the MoO_x layer, namely preannealing. The solar cell performance, disappointingly, is worse instead of getting better. The possible reason is that an

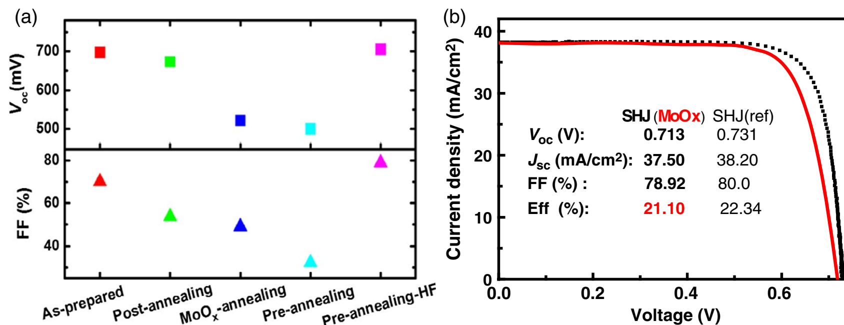

Figure 5. a) Influence of annealing process on V_{oc} and FF of the SHJ solar cells with MoO_x HSL. b) Light J–V characteristics of a champion SHJ solar cell with MoO_x HSL (red line) and a reference SHJ solar cell (black dots).

© 2020 WILEY-VCH Verlag GmbH & Co. KGaA, Weinheim

a-Si:H/SiO_x double layer is formed during the preannealing process in the air atmosphere. Thus, dipoles can be formed at the SiO_x/MoO_x interface,[27] which have a negative effect on the energy band bending and the selective transportation of the carriers. Therefore, we removed the oxidation layer on the amorphous silicon by HF solution (2%) treatment after the preannealing process and immediately prepared the MoO_x HSL and the metal back electrode to finish the device fabrication. Just as expected, the performance of the preannealing-HF sample shows a remarkable improvement as shown in Figure 5a. The light J–V curve and PV parameters of a champion SHJ solar cell fabricated with the preannealing-HF process are shown in Figure 5b. An efficiency of 21.10% with V_{oc} of 713 mV, J_{sc} of 37.50 mA cm^{-2}, and FF of 78.92% was achieved for the SHJ solar cell with a MoO_x HSL. The integrated photocurrent density calculated from the external quantum efficiency is 37.2 mA cm^{-2} (Figure S6, Supporting Information), which is in good agreement with the measured J_{sc}. For comparison, the J–V curve and PV parameters of an optimized reference SHJ solar cell ($15.6 \times 15.6\ cm^2$) are also given in Figure 5b. We found that, at the present stage, the performance of the novel SHJ solar cell was still lower than that of the reference SHJ solar cell. It should be noted that the novel SHJ solar cells are affected by the size effect of the solar cells. The size of the novel SHJ solar cells was about $1 \times 1\ cm^2$. The edges of the device were not well passivated at the present stage. If larger Si substrates are used, or if the edges of the devices are well passivated, higher performance can be expected for the SHJ solar cells.

The performance of the SHJ solar cells with the HWOSD MoO_x HSL is comparable to that of the SHJ solar cells with a MoO_x HSL prepared by thermal evaporation,[2,4] electron-beam evaporation,[15,20] or atomic layer deposition.[21] The simplification and scalability of the MoO_x preparation and the simplified fabrication process of the devices make the HWOSD MoO_x a great potential substitute for the doped Si layer in high-efficiency c-Si solar cells in the future.

3.4. Transport Mechanisms of the SHJ Solar Cells with HWOSD MoO_x HSL

Inspired by the great potential of the SHJ solar cells with a MoO_x HSL, a lot of researches, numerically or experimentally, on the current extraction of charge carriers via the MoO_x HSL were conducted to deeply understand the transport mechanisms and to assist the engineering of the novel SHJ solar cells.[6,28,29] It was shown that, for an effective hole extraction, a sufficiently high MoO_x work function or/and efficient trap-assisted tunneling paths are requirements that have to be fulfilled.[28,29] Based on the analysis of the dark J–V–T characteristics, transport mechanisms including trap-assisted tunnel of holes at low voltage and transport behavior of a Schottky-like junction at higher voltage were proposed by García-Hernansanza et al. for a SHJ solar cell with a thermally evaporated MoO_x HSL and without any passivation layer.[6] For our SHJ devices with a MoO_x HSL fabricated using HWOSD and with an a-Si:H passivation layer prepared by PECVD, a fairly high V_{oc} of above 710 mV was achieved. It is necessary to investigate and understand the mechanisms governing charge carrier transport of the novel heterojunction and to further improve the performance of the devices.

Dark J–V–T measurements were conducted for an SHJ solar cell with the structure Ag/ITO/n^+-a-Si:H /i a-Si:H/n-c-Si/i a-Si:H/ MoO_x/Ag in the temperature range 200–380 K and the dark J–V curves are shown in **Figure 6**a. The corresponding photovoltaic parameters of the device are $V_{oc} = 710$ mV, FF = 77.0%, $J_{sc} = 37.3$ mA cm^{-2}, and Eff = 20.4%.

Considering the change of the slopes of the J–V curves, a two-diode model can be used to fit the experimental results.[30] The current density varied with the applied voltage can be written as

$$J = J_{01}\left[e^{A_1(V-JR_s)} - 1\right] + J_{02}\left[e^{A_2(V-JR_s)} - 1\right] + \frac{V - JR_s}{R_{sh}} \tag{1}$$

where J_{01} and J_{02} are the saturation current densities of diode 1 and 2, R_s and R_{sh} are the series and shunt resistance, A_1 and A_2 depend on the transport mechanisms. The contributions of diodes 1 and 2 to the J–V curves are generally considered to be in the high (>0.5 V) and low (<0.5 V) voltage regions, respectively. The exponential factor A_i ($i = 1, 2$) generally has an empirical expression of $A_i = q/n_ikT$, where q is the electron charge, n_i the diode ideality factor, k the Boltzmann's constant, and T the absolute temperature.

Based on Equation (1), the dark J–V curves were fitted. It was found that A_1 changes linearly with the increasing of $1/kT$ and a constant ideality factor $n_1 = 1.2$ can be determined for diode 1, which is often observed in a rectifier junction. However, A_2 does not change significantly in the whole experimental temperature range and no unified ideality factor n_2 can be determined. For a relatively narrow temperature region of $250 < T < 330$ K ($35.0 < 1/kT < 46.2$), fairly large diode ideality factor values varying between 3.51 and 3.93 can be obtained. In the traditional SHJ solar cells, large n_2 is usually considered to be a signal of serious shunt leakage current[31] or interface recombination,[32] which certainly degrades the FF, V_{oc}, and efficiency. In this work, the contradiction between the large n_2 and quite high V_{oc} and FF of the device implies different transport mechanisms from the traditional ones. Numerical calculation has shown that the trap-assisted tunnel transport plays an important role in the current extraction of the novel SHJ solar cells,[28] which has been proved by García-Hernansanza et al. in a MoO_x/n-c-Si heterojunction device.[6] According to the large value and the temperature-dependence characteristic of n_2, trap-assisted tunnel transport at a lower voltage range is also considered for our novel SHJ solar cell and will be discussed further.

Considering the high work function (>6 eV) and high density of gap states characteristic of amorphous MoO_x,[4] it is appropriate to think of the MoO_x/i a-Si:H/n-c-Si heterocontact as a Schottky-like rectifier junction with large barrier height,[12] whose energy band structures under forward bias and illumination are depicted in Figure 6c,d. Based on the aforementioned analysis, three main transport processes, including thermionic emission of electrons, thermal-assisted tunneling of electrons, and trap-assisted tunneling of holes, denoted by a, b, and c respectively, are considered as the basic transport processes.

In both the a and b processes, thermionic activation of majority carriers is involved. Therefore, we use a total majority-carrier

© 2020 WILEY-VCH Verlag GmbH & Co. KGaA, Weinheim

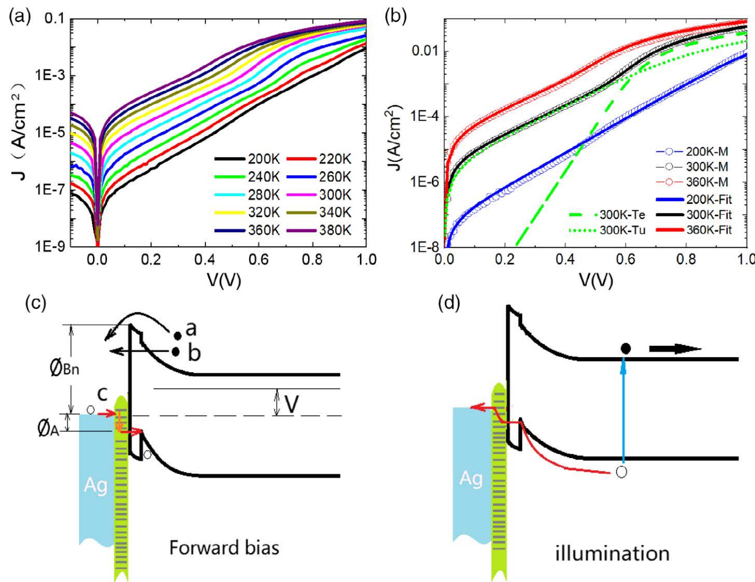

Figure 6. a) Dark J–V curves of a novel SHJ solar cell measured at temperatures from 200 to 380 K. b) Experimental (hollow symbols) and fitting (solid lines) dark J–V curves under forward bias for the novel SHJ solar cell under three temperatures of 200, 300, and 360 K. The green dashed and dotted lines respectively represent the fitted J_{Te} (majority-carrier processes a and b) and J_{Tu} (minority-carrier process c) for the J–V curve measured under 300 K. c) Schematic energy band structures of the MoO_x/i a-Si:H/n-c-Si heterocontact under forward bias. Three transport processes, including thermionic emission of electrons, thermal-assisted tunneling of electrons, and tunneling of holes are denoted by a, b, and c, respectively. d) Schematic energy band structures of the heterocontact under illumination.

(electron) thermionic current density J_{Te} to represent the thermionic emission and thermal-assisted tunneling processes. In the process c, minority carriers (holes) tunnel through the gap states of the MoO_x layer into the top of the valence band (TVB) of the c-Si and then recombine with electrons. J_{Tu} is used to express the current density related to the trap-assisted tunneling of holes. Now, Equation (1) can be expressed as

$$J = J_{Te} + J_{Tu} + J_{shunt} = J_{01}\left[\exp\left(\frac{q(V - JR_s)}{n_1 kT}\right) - 1\right] + J_{02}\left[\exp\left(\frac{q(V - JR_s)}{E_0}\right) - 1\right] + \frac{V - JR_s}{R_{sh}} \tag{2}$$

$$J_{01} = C(T)\exp\left(-\frac{q\phi_{Bn}}{kT}\right) \tag{3}$$

$$J_{02} = B(T)\exp\left(-\frac{q\phi_{A}}{kT}\right) \tag{4}$$

where $q\phi_{Bn}$ is the effective barrier height for electrons, $C(T)$ a temperature-dependent prefactor, E_0 the tunneling barrier energy, and $q\phi_A$ the activation energy of holes. E_0 is related to the almost invariable slopes of the dark J–V curves at low bias as Figure 6a shows and is simplified to be a constant in the following fittings. $q\phi_A$ is actually the difference between the TVB of the c-Si surface and the Fermi level of the Ag electrode, as shown in Figure 6c. Comparing Equation (1) and (2), we can easily find that J_{Te} and J_{Tu} correspond to the contributions of diodes 1 and 2, respectively. In Equation (2), the transport mechanisms corresponding to the two diodes are specified.

Three forward J–V curves measured at temperatures of 200, 300, and 360 K were fitted according to Equation (2), as shown in Figure 6b. Good agreement between the measured and the fitted curves in the whole voltage range can be obtained. The fitting results for E_0, $q\phi_A$, and $q\phi_{Bn}$ are 0.087, 0.29, and 0.98 eV, respectively. To better understand the respective contributions of J_{Tu} and J_{Te} to the total J–V curve, the fitted J_{Te} and J_{Tu} for the J–V curve measured under 300 K, as an example, are shown by dashed and dotted lines in Figure 6b.

It can be seen that J_{Te} starts to play a major role as $V > 0.6$ V. As we know, the dominant transport mechanism at high bias plays an important role in the performance, especially V_{oc}, of the solar cells. Therefore, the high V_{oc} of the novel SHJ solar cells should be related to the large effective barrier height $q\phi_{Bn}$ of the transport processes a and b. In this case, a strong inversion of the energy band near the n-type c-Si surface is formed and effective collection of photogenerated electrons can be achieved, as shown in Figure 6d. The $q\phi_{Bn}$ we obtained was a little bit higher than that reported by García-Hernansanza et al.,[6] which coincides with the fact that the V_{oc} of our device is higher. It is worth noting that the fitted $q\phi_{Bn}$ is much smaller than the work-function difference between the MoO_x and n type c-Si. The electrostatic

© 2020 WILEY-VCH Verlag GmbH & Co. KGaA, Weinheim

potential and the barrier height can be modified by the interface-trapped charges and also the possible dipoles.[33] If the interface was better passivated, larger barrier height could be expected. Furthermore, as a type of inversion layer solar cell,[34] the high conductivity of the inversion layer may lead to good transverse transportation and then high FF can be achieved.

In the case of lower forward bias ($V < 0.5$ V), the tunnel current density J_{Tu} dominates the J–V curve and causes a lower slope of log (J) versus V. The high defect density in the bandgap of amorphous MoO_x makes the tunneling process easier and the minority current density J_{Tu} is larger than that of a typical metal/Si Schottky junction. This tunneling channel is critically important for the carriers collection under illumination. Photogenerated holes can be effectively collected through this tunneling channel, which is beneficial to achieve high open-circuit voltage. In addition, we can also see from Figure 6b that, in the high voltage region, the contribution of the minority current density J_{Tu} should not be ignored like a typical majority-carrier device. The high barrier or the strong inversion characteristic produces a high minority-carrier injection ratio in the Schottky-like junction.

4. Conclusions

The HWOSD method is demonstrated to be a promising technique for preparation of high-quality MoO_x films with uniform thickness, compact structure, nice photoelectric properties, and conformal coverage on textured Si substrates. Novel SHJ solar cells with the HWOSD MoO_x thin films as the HSL were successfully fabricated. An efficiency of 21.10% was achieved for the champion SHJ solar cell with a MoO_x HSL fabricated by the scalable HWOSD technique.

Analysis of the dark J–V–T characteristics shows that tunneling of holes through the gap states of the MoO_x layer causes the low slope of the plot of log (J) versus V at low voltage range ($V < 0.5$ V). This tunneling channel is beneficial for the hole collection under illumination. A high Schottky-like barrier can be obtained from the fitting of the J–V curve in the high voltage range (>0.6), which indicates a strong inversion of the c-Si energy band near the interface. The high effective barrier and the strong inversion layer promote the efficient collection of the photogenerated carriers and lead to good transverse transportation, which are helpful for achieving high V_{oc} and FF. It is this characteristic that makes the novel MoO_x/c-Si heterojunction solar cells inherently possess the potential of high efficiency. More research work is needed to fully reveal the potential of the novel SHJ solar cells.

5. Experimental Section

Fabrication of Silicon Heterojunction Solar Cells: N-type <100> float zone (FZ) silicon wafers with a thickness of 250 μm and a resistivity of 1–5 Ω cm were used as the substrates. Alkaline texturing and isotropic etching were carried out in succession to form random pyramids with less sharp tops on both sides of the c-Si wafers. After texturing, the c-Si substrates were chemically cleaned according to the standard RCA procedure. Before proceeding to the next step, the textured silicon wafers were dipped in 2% hydrofluoric acid for 1 min to remove the surface oxide layer.

The illuminated side (front side) structure of the devices was set to be Ag grid/ITO/n-type a-Si:H/i a-Si:H. Intrinsic (≈7 nm) and n-type (≈10 nm) a-Si:H as the passivation and the electron-selective transport layer were successively deposited on one side of the c-Si substrates by means of PECVD under a substrate temperature of about 200 °C. The front electrode consisted of an ITO layer (80 nm) deposited by magnetron sputtering and a silver grid deposited by thermal evaporation. The rear side structure of the SHJ solar cells was Ag/MoO_x/i a-Si:H. The i a-Si:H thin film (≈6 nm) deposited by PECVD was also used for interface passivation. The MoO_x thin film, as the HSL to replace the traditional p-type a-Si:H, was prepared by HWOSD. Thermal evaporated Ag film was used as the rear electrode. The active area of the devices was 1 cm^2.

Characterization of Thin Films and Devices: Thicknesses of MoO_x and ITO thin films were measured using a surface profilometer (ERUKER-DektakXT). Surface morphologies and elemental analysis of the MoO_x thin films deposited on c-Si wafers were characterized using scanning electron microscope (SEM, Hitachi SU8010) and EDS(Bruker 6-30). Elemental compositions of the MoO_x films were characterized using X-ray photoelectron spectroscopy (XPS, Thermo Scientific ESCALAB250Xi) under ultrahigh vacuum ($<2 \times 10^{-9}$ mbar). Minority carrier lifetimes of the passivated c-Si wafers were evaluated using the quasi-steady-state photo conductance (QSSPC Sinton WCT-120). Light current density–voltage (J–V) curves of the solar cells were obtained under AM 1.5 (100 mW cm^{-2}, 25 °C) illumination. Dark J–V–T characteristics of the SHJ solar cells were measured at temperatures from 200 to 380 K.

Supporting Information

Supporting Information is available from the Wiley Online Library or from the author.

Acknowledgements

This work was supported by the National Key R&D Program of China (2018YFB1500102) and the National Natural Science Foundation of China (No.61604153 and No.61674150). Support from the Sino-Danish Center for Education and Research (SDC) is fully acknowledged.

Conflict of Interest

The authors declare no conflict of interest.

Keywords

hole-selective transport layers, hot wire oxidation–sublimation deposition, molybdenum oxide thin films, silicon heterojunction solar cells, transport mechanisms

Received: November 13, 2019
Revised: January 7, 2020
Published online: February 9, 2020

[1] a) P. Q. Gao, Z. H. Yang, J. He, J. Yu, P. P. Liu, J. Y. Zhu, Z. Y. Ge, J. C. Ye, *Adv. Sci.* **2018**, *5*, 20; b) X. B. Yang, E. Aydin, H. Xu, J. X. Kang, M. Hedhili, W. Z. Liu, Y. M. Wan, J. Peng, C. Samundsett, A. Cuevas, S. De Wolf, *Adv. Energy Mater.* **2018**, *8*, 7; c) Z. Wang, P. Li, Z. Liu, J. Fan, X. Qian, J. He, S. Peng, D. He, M. Li, P. Gao, *APL Mater.* **2019**, *7*, 110701.

[2] J. Geissbuhler, J. Werner, S. M. de Nicolas, L. Barraud, A. Hessler-Wyser, M. Despeisse, S. Nicolay, A. Tomasi, B. Niesen, S. De Wolf, C. Ballif, *Appl. Phys. Lett.* **2015**, *107*, 5.

© 2020 WILEY-VCH Verlag GmbH & Co. KGaA, Weinheim

[3] J. Bullock, M. Hettick, J. Geissbuhler, A. J. Ong, T. Allen, C. M. Sutter-Fella, T. Chen, H. Ota, E. W. Schaler, S. De Wolf, C. Ballif, A. Cuevas, A. Javey, *Nat. Energy* **2016**, *1*, 7.
[4] a) C. Battaglia, X. T. Yin, M. Zheng, I. D. Sharp, T. Chen, S. McDonnell, A. Azcatl, C. Carraro, B. W. Ma, R. Maboudian, R. M. Wallace, A. Javey, *Nano Lett.* **2014**, *14*, 967; b) J. Wang, H. Lin, Z. Wang, W. Shen, J. Ye, P. Gao, *Nano Energy* **2019**, *66*, 104116.
[5] J. N. Tong, Y. M. Wan, J. Cui, S. Lim, N. Song, A. Lennon, *Appl. Surf. Sci.* **2017**, *423*, 139.
[6] R. Garcia-Hernansanz, E. Garcia-Hemme, D. Montero, J. Olea, A. del Prado, I. Martil, C. Voz, L. G. Gerling, J. Puigdollers, R. Alcubilla, *Sol. Energy Mater. Sol. Cells* **2018**, *185*, 61.
[7] a) O. Almora, L. G. Gerling, C. Voz, R. Alcubilla, J. Puigdollers, G. Garcia-Belmonte, *Sol. Energy Mater. Sol. Cells* **2017**, *168*, 221; b) W. L. Wu, J. Bao, X. G. Jia, Z. T. Liu, L. Cai, B. H. Liu, J. W. Song, H. Shen, *Phys. Status Solidi RRL* **2016**, *10*, 662; c) G. Masmitja, L. G. Gerling, P. Ortega, J. Puigdollers, I. Martin, C. Voz, R. Alcubilla, *J. Mater. Chem. A* **2017**, *5*, 9182.
[8] a) M. Mews, L. Korte, B. Rech, *Sol. Energy Mater. Sol. Cells* **2016**, *158*, 77; b) M. Mews, A. Lemaire, L. Korte, *IEEE J. Photovoltaics* **2017**, *7*, 1209.
[9] M. Y. Xue, R. Islam, Y. S. Chen, J. Y. Chen, C. Y. Lu, A. M. Pleus, C. Tae, K. Xu, Y. Liu, T. I. Kamins, K. C. Saraswat, J. S. Harris, *J. Appl. Phys.* **2018**, *123*, 5.
[10] H. Imran, T. M. Abdolkader, N. Z. Butt, *IEEE Trans. Electron Devices* **2016**, *63*, 3584.
[11] P. Ravindra, R. Mukherjee, S. Avasthi, *IEEE J. Photovoltaics* **2017**, *7*, 1278.
[12] L. G. Gerling, S. Mahato, A. Morales-Vilches, G. Masmitja, P. Ortega, C. Voz, R. Alcubilla, J. Puigdollers, *Sol. Energy Mater. Sol. Cells* **2016**, *145*, 109.
[13] a) S. Avasthi, W. E. McClain, G. Man, A. Kahn, J. Schwartz, J. C. Sturm, *Appl. Phys. Lett.* **2013**, *102*, 4; b) M. M. Plakhotnyuk, N. Schuler, E. Shkodin, R. A. Vijayan, S. Masilamani, M. Varadharajaperumal, A. Crovetto, O. Hansen, *Jpn. J. Appl. Phys.* **2017**, *56*, 8.
[14] H. Tong, Z. H. Yang, X. X. Wang, Z. L. Liu, Z. X. Chen, X. X. Ke, M. L. Sui, J. Tang, T. B. Yu, Z. Y. Ge, Y. H. Zeng, P. Q. Gao, J. C. Ye, *Adv. Energy Mater.* **2018**, *8*, 10.
[15] J. Yu, Y. M. Fu, L. Q. Zhu, Z. H. Yang, X. Yang, L. Ding, Y. H. Zeng, B. J. Yan, J. Tang, P. Q. Gao, J. C. Ye, *Sol. Energy* **2018**, *159*, 704.
[16] a) P. P. Boix, J. Ajuria, I. Etxebarria, R. Pacios, G. Garcia-Belmonte, J. Bisquert, *J. Phys. Chem. Lett.* **2011**, *2*, 407; b) W. Y. Zhang, Q. L. Meng, B. X. Lin, Z. X. Fu, *Sol. Energy Mater. Sol. Cells* **2008**, *92*, 949.
[17] a) J. Meyer, S. Hamwi, M. Kroger, W. Kowalsky, T. Riedl, A. Kahn, *Adv. Mater.* **2012**, *24*, 5408; b) Y. Z. Guo, J. Robertson, *Appl. Phys. Lett.* **2014**, *105*, 4; c) C. Battaglia, S. M. de Nicolas, S. De Wolf, X. T. Yin, M. Zheng, C. Ballif, A. Javey, *Appl. Phys. Lett.* **2014**, *104*, 5.
[18] M. T. Greiner, L. Chai, M. G. Helander, W. M. Tang, Z. H. Lu, *Adv. Funct. Mater.* **2012**, *22*, 4557.
[19] B. C. Han, M. Gao, Y. Z. Wan, Y. Li, W. L. Song, Z. Q. Ma, *Mater. Sci. Semicond. Process.* **2018**, *75*, 166.
[20] R. Sivakumar, R. Gopalakrishnan, M. Jayachandran, C. Sanjeeviraja, *Curr. Appl. Phys.* **2007**, *7*, 51.
[21] a) B. Macco, M. F. J. Vos, N. F. W. Thissen, A. A. Bol, W. M. M. Kessels, *Phys. Status Solidi RRL* **2015**, *9*, 393; b) J. Ziegler, M. Mews, K. Kaufmann, T. Schneider, A. N. Sprafke, L. Korte, R. B. Wehrspohn, *Appl. Phys. A: Mater. Sci. Process.* **2015**, *120*, 811.
[22] a) S. H. Mohamed, S. Venkataraj, *Vacuum* **2007**, *81*, 636; b) J. M. Pachlhofer, C. Jachs, R. Franz, E. Franzke, H. Kostenbauer, J. Winkler, C. Mitterer, *Vacuum* **2016**, *131*, 246.
[23] R. E. I. Schropp, *Thin Solid Films* **2015**, *595*, 272.
[24] D. Sacchetto, Q. Jeangros, G. Christmann, L. Barraud, A. Descoeudres, J. Geissbuhler, M. Despeisse, A. Hessler-Wyser, S. Nicolay, C. Ballif, *IEEE J. Photovoltaics* **2017**, *7*, 1584.
[25] T. Zhang, C. Y. Lee, Y. M. Wan, S. Lim, B. Hoex, *J. Appl. Phys.* **2018**, *124*, 7.
[26] S. Essig, J. Dreon, E. Rucavado, M. Mews, T. Koida, M. Boccard, J. Werner, J. Geissbuhler, P. Loper, M. Morales-Masis, L. Korte, S. De Wolf, C. Ballif, *Sol. RRL* **2018**, *2*, 1700227.
[27] K. Kita, A. Toriumi, *Appl. Phys. Lett.* **2009**, *94*, 3.
[28] C. Messmer, M. Bivour, J. Schon, M. Hermle, *J. Appl. Phys.* **2018**, *124*, 8.
[29] R. A. Vijayan, S. Essig, S. De Wolf, B. G. Ramanathan, P. Loper, C. Ballif, M. Varadharajaperumal, *IEEE J. Photovoltaics* **2018**, *8*, 473.
[30] R. Hussein, D. Borchert, G. Grabosch, W. R. Fahrner, *Sol. Energy Mater. Sol. Cells* **2001**, *69*, 123.
[31] S. Dongaonkar, J. D. Servaites, G. M. Ford, S. Loser, J. Moore, R. M. Gelfand, H. Mohseni, H. W. Hillhouse, R. Agrawal, M. A. Ratner, T. J. Marks, M. S. Lundstrom, M. A. Alam, *J. Appl. Phys.* **2010**, *108*, 124509.
[32] R. V. K. Chavali, J. R. Wilcox, B. Ray, J. L. Gray, M. A. Alam, *IEEE J. Photovoltaics* **2014**, *4*, 763.
[33] L. G. Gerling, S. Mahato, A. Morales-Vilches, G. Masmitja, P. Ortega, C. Voz, R. Alcubilla, J. Puigdollers, *Sol. Energy Mater. Sol. Cells* **2016**, *145*, 109.
[34] R. Har-Lavan, D. Cahen, *IEEE J. Photovoltaics* **2013**, *3*, 1443.

© 2020 WILEY-VCH Verlag GmbH & Co. KGaA, Weinheim

Supporting information: Molybdenum oxide hole selective transport layer by hot wire oxidation-sublimation deposition for silicon heterojunction solar cells

Fengchao Li[1,2,3], Yurong Zhou[1]*, Ying Yang[1], Gangqiang Dong[1], Yuqin Zhou[1], Fengzhen Liu[1,2]*, Donghong Yu[3,4]

1 . Center of Materials Science and Optoelectronics Engineering & College of Materials Science and Opto-Electronic Technology, University of Chinese Academy of Sciences, 100049, Beijing, China

2. Sino-Danish College, University of Chinese Academy of Sciences, 100190, Beijing, China

3. Department of Chemistry and Bioscience, Aalborg University, DK-9220, Aalborg, Denmark

4. Sino-Danish Center for Education and Research, Aarhus, DK-8000, Denmark, DK-8000, Denmark

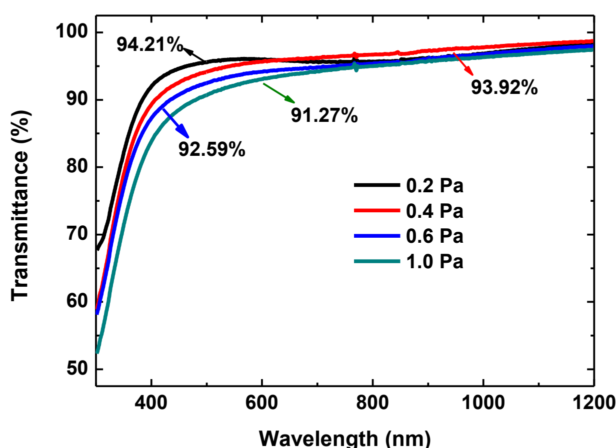

Figure S1 Transmittance spectra of MoOx thin films deposited at different oxygen pressures of 0.2~1.0 Pa.

Oxygen pressure is an important factor affecting the quality of molybdenum oxide thin films prepared using hot filament oxidation-sublimation deposition (HWOSD) technique. Figure S1 compares the transmittance of the MoO_x thin films with the same thickness (15nm) deposited at different oxygen pressures. In the

long-wave region, the transmittance is similar for all of the MoO_x thin films deposited at different oxygen pressures. However, the transmittance of the MoO_x films shows significant increase in the short-wave region as the oxygen pressure decreases from 1.0 Pa to 0.2Pa. The average transmittances are 94.21%, 93.92%, 92.59% and 91.27% for the MoO_x thin films deposited at the oxygen pressures of 0.2 Pa, 0.4 Pa, 0.6 Pa and 1.0 Pa, respectively.

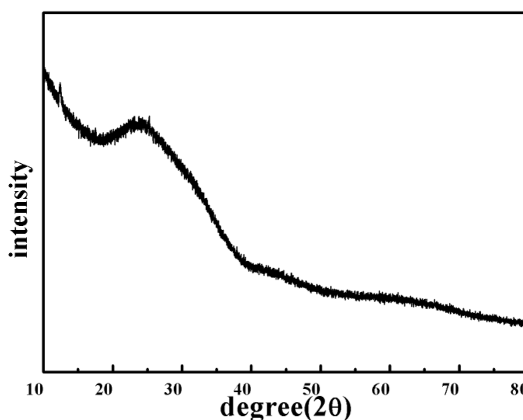

Figure S2 XRD spectrum of a MoO_x thin film prepared by HWOSD.

Figure S2 shows the XRD spectrum of a MoO_x thin film deposited using HWOSD technique. It can be seen that there is a dispersed diffraction peak at about 25.8 degree corresponding to the amorphous phase of MoO_x.

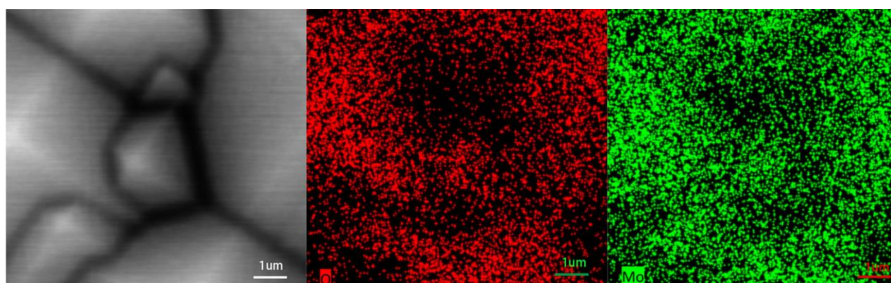

Figure S3 Top view SEM image of a MoO_x covered pyramid-textured Si wafer and the corresponding energy dispersive X-ray spectroscopy (EDS) elemental mappings of O and Mo.

Figure S3 shows the SEM image of a zone of pyramid-textured Si wafer coved

with MoO_x thin film by HWOSD and the corresponding EDS elemental mappings of O and Mo. It can be seen that good coverage of MoO_x on pyramid-textured Si wafer was obtained.

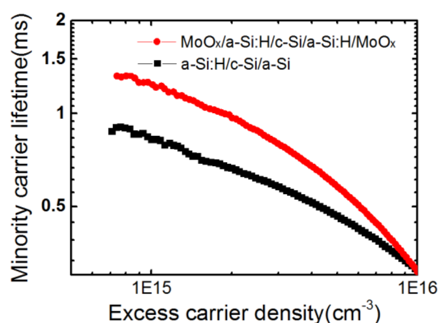

Figure S4 Measured effective lifetimes for samples with the structures of i a-Si:H/c-Si/i a-Si:H and MoO_x/i a-Si:H/c-Si/i a-Si:H/MoO_x as a function of excess carrier density in the range of 7×10^{14} cm^{-3}~$1\times10^{16}cm^{-3}$.

Compared with the i a-Si:H passivated sample, the i a-Si:H/MoO_x combination layer passivated sample shows enhanced lifetimes in the whole carrier injection concentration range of 7×10^{14} cm^{-3}~$1\times10^{16}cm^{-3}$ and a maximum lifetime up to 1.3 ms is achieved, which demonstrate the effective field passivation effect of the molybdenum oxide film on the surface of c-Si. It is worth pointing out that the lifetime values are affected by the size of the samples. The effective lifetime of the i a-Si:H passivated sample with small size (830μs at 1×10^{15} cm^{-3} injection with size of 4cm×4cm) is much lower than that of a large one (2ms at 1×10^{15} cm^{-3} injection with size of 12.5cm ×12.5cm). If a larger silicon wafer is used, or if the edge of the device is well passivated, higher lifetime values can be expected.

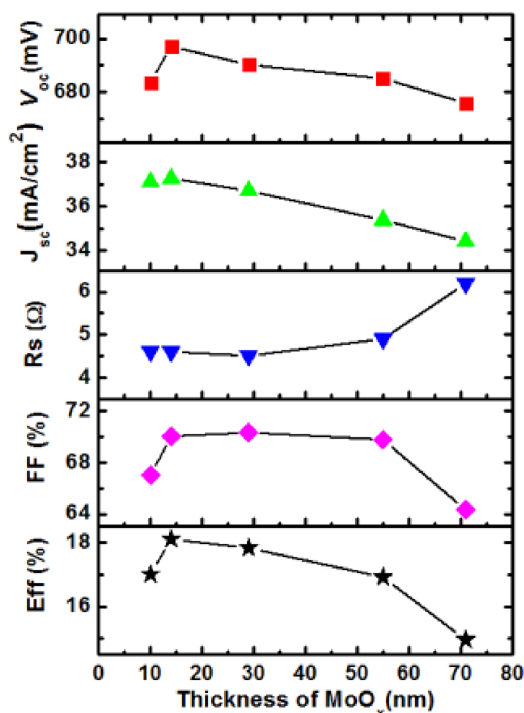

Figure S5 Photovoltaic parameters of the SHJ solar cells varied with thicknesses of MoO_x HSL.

Figure S5 shows the influence of the MoO_x HSL thickness on the photovoltaic parameters of the SHJ solar cells. Increasing the MoO_x HSL thickness from 10 nm to 14 nm raises the V_{oc} of the solar cells by 13.5 mV (from 683.6mV to 697.1mV). However, the V_{oc} goes down instead of rising as we further increased the MoO_x HSL thickness. And, it drops to 675.8mV at a MoO_x thickness of 71 nm. In the case that the thickness of the MoO_x HSL is too small, the space charge region or the inversion layer near the c-Si surface may not be well formed, which is not favorable for the separation and collection of the photo-generated carriers. However, as for the condition of excessive MoO_x thickness, the consequentially enhanced recombination in the MoO_x layer leads to the decline of the open circuit voltage. At the same time, the reduced carrier collection causes a rapid drop in the short circuit current density (J_{sc}). Fill factor (FF) is affected simultaneously by energy band structure and series

resistance. The small FF in the 10 nm MoO_x condition could also be a consequence of the insufficient build-up of the inversion layer. When the thickness of MoO_x is between 14 nm and 55 nm, the relatively large built-in voltage and the almost invariable series resistance keep the FF at a relatively high value. When the thickness of the MoO_x reaches 70nm, the high series resistance results in a significant reduction in FF.

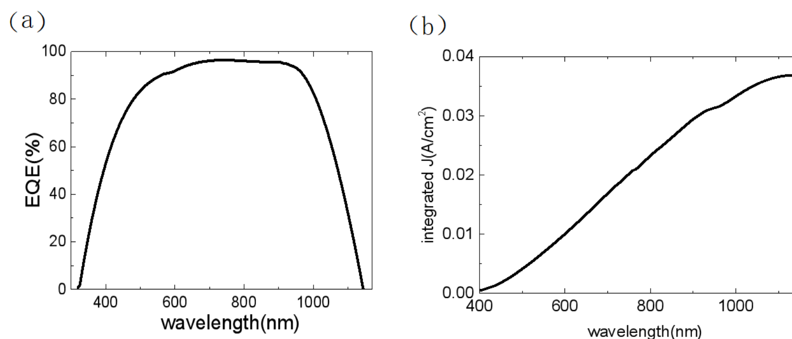

Figure S6 EQE spectrum and integrated current density spectrum of the champion SHJ solar cell fabricated with the pre-annealing-HF process.

Figure S6 shows the EQE spectrum and the integrated current density spectrum of the champion SHJ solar cell fabricated with the pre-annealing-HF process. The integrated photocurrent density 37.2mA/cm^2 is in good agreement with the measured short circuit current density (37.50 mA/cm^2) of the solar cell, which indicates that the light J-V measurement procedure is correct.

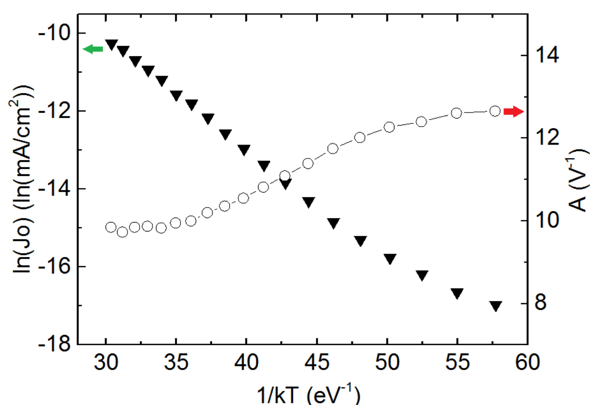

Figure S7 The fitted $ln(J_0)$ and A varied with $1/kT$ according to the dark J-V-T curves of the novel SHJ solar cell.

Figure S7shows the temperature dependences of the fitting parameters J_0 and A varied with $1/kT$. An approximate linear relationship between $ln(J_0)$ and $1/kT$ can be determined, an activation energy of about 0.3eV can be obtained. However, A does not change significantly in the whole temperature range. As the temperature varied from 220K to 380K, the factor A merely changes from about 10 to less than 13. And the relationship between A and $1/kT$ seriously deviates from linearity in both high and low temperature regions. This is significantly different from the typical diffusion or recombination transport processes, in which A is temperature dependent and varies in a more large range.

Table S1 Photovoltic parameters of MoO_x-based SHJ solar cells with different passivation layers.

Passivation layer	V_{oc}(mV)	J_{sc}(mA/cm^2)	FF(%)	Eff(%)	Rs(Ω)
--	549.7	34.18	74.96	14.09	2.3
SiOx	643.5	36.88	70.54	16.74	3.1
a-Si	690.2	36.72	70.35	17.83	4.5
a-Si/SiO_x	625.0	38.50	67.23	16.17	7.6

The photovoltic parameters of MoO_x-based SHJ solar cells with different passivation layers between the MoO_x (27 nm) and the c-Si are given in Table S1. As a reference, the parameters of the SHJ solar cell with MoO_x HSL directly contacting with the Si substrate is included in Table S1. The open circuit voltage (V_{oc}) and power conversion efficiency (Eff) of the reference device are 549.7mV and 14.09%, respectively. The performance of the reference SHJ solar cell is much worse than that of a traditional SHJ solar cell, indicating a serious recombination of photo-generated carriers at the interface between the MoO_x layer and the Si substrate. All the passivation methods we tried, including intrinsic a-Si:H thin film, UV/O3 photo-oxidized SiO_x, and the combination of

a-Si:H and SiO_x, improved the V_{oc} of the solar cells to some extent. Among them, the intrinsic a-Si:H layer deposited using PECVD exhibits the best passivation effect.

Appendix B. Paper Ⅱ

Solar Energy Materials & Solar Cells 203 (2019) 110196

Contents lists available at ScienceDirect

Solar Energy Materials and Solar Cells

journal homepage: http://www.elsevier.com/locate/solmat

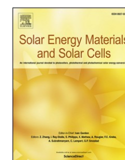

Lithography-free and dopant-free back-contact silicon heterojunction solar cells with solution-processed TiO_2 as the efficient electron selective layer

Fengchao Li [a,c], Zongheng Sun [a], Yurong Zhou [a,*], Qi Wang [a], Qunfang Zhang [b], Gangqiang Dong [a], Fengzhen Liu [a,**], Zhenjun Fan [d], Zhenghao Liu [a], Zhengxiong Cai [a], Yuqin Zhou [a], Donghong Yu [e]

[a] *Center of Materials Science and Optoelectronics Engineering & College of Materials Science and Opto-Electronic Technology, University of Chinese Academy of Sciences, 100049, Beijing, China*
[b] *Hanenergy Mobile Energy Holding Group, 100107, Beijing, China*
[c] *Sino-Danish College, University of Chinese Academy of Sciences, 100190, Beijing, China*
[d] *China University of Geosciences, 100083, Beijing, China*
[e] *Department of Chemistry and Bioscience, Aalborg University, DK-9220, Aalborg, Denmark*

ARTICLE INFO

Keywords:
Lithography-free
Back-contact
Dopant-free
Heterojunction
Passivation

ABSTRACT

Lithography-free interdigitated back-contact silicon heterojunction (IBC-SHJ) solar cells with dopant-free metal oxides (TiO_2 and MoO_x) as the carriers selective transport layers were investigated. Spin-coating and hot-wire reactive-sublimation deposition together with low cost mask technology were used to fabricate the solar cells. Insertion of a SiO_x layer with the thickness of about 2.4 nm between the intrinsic amorphous Si (a-Si:H(i)) passivation layer and the spin-coated TiO_2 layer greatly improves the solar cell performance due to the enhanced field-effect passivation of the a-Si:H(i)/SiO_x/TiO_2 layer stack. Efficiency up to 20.24% was achieved on the lithography-free and dopant-free IBC-SHJ devices with a-Si:H(i)/SiO_x/TiO_2 layer stack as the electron selective transport layer, a-Si:H(i)/MoO_x as the hole selective transport layer, and WO_x as the antireflection layer. The novel IBC-SHJ solar cells show significant advantages in simplification of the technology and process compared with the IBC-SHJ devices whose back surface pattering and carrier selective layers relied on photolithography and plasma enhanced chemical vapor deposition (PECVD).

1. Introduction

Recently, performance of a-Si:H/c-Si heterojunction (SHJ) solar cells with interdigitated back contact (IBC) has been significantly improved [1–5] and a record power conversion efficiency (PCE) of 26.7% [5] has been achieved. The excellent interface passivation provided by the intrinsic hydrogenated amorphous silicon (a-Si:H(i)) leads to a high open circuit voltage and the IBC configuration brings us a large short circuit current at the same time [5]. However, photolithography technology is usually involved in the fabrication process of the high-efficiency IBC solar cells, which significantly boosts the manufacturing cost. In recent years, various lithography-free fabrication techniques have been developed to reduce the fabrication cost of the IBC solar cells [6–10]. Efficiencies have been rapidly updated for the lithography-free back contacted silicon heterojunction solar cells based on an innovative tunnel-IBC approach by combining shadow mask with PECVD [7]. A record efficiency of 25% for these tunnel-IBC devices has been achieved by Lachenal et al. [9] By using ion implantation technique and metal masks, an efficiency of 22.9% for a homojunction solar cell with IBC configuration was reported by Y.S. Kim et al. [10].

Some wide band-gap dopant-free materials were recently used to substitute the doped a-Si:H and serve as the carrier selective transport layers in the SHJ solar cells. Metal oxides or alkali metal salts with high work-function (e.g. MoO_x [11–13], WO_x [14,15], and V_2O_5 [16,17]) and low work-function (e.g. TiO_x [18], MgO_x [19], ZnO_x, and LiF_x [12]) were respectively used as the hole selective transport layer (HSTL) and electron selective transport layer (ESTL) in c-Si solar cells. A PCE up to 22.5% has been achieved on a MoOx/n c-Si heterojunction solar cell [11]. Efficiencies of 21.6% and 20% were respectively achieved on n-type c-Si solar cells using TiO_x and MgO_x as the ESTL [18,19]. It is

* Corresponding author.
** Corresponding author.
E-mail address: zhouyurong@ucas.ac.cn (Y. Zhou).

https://doi.org/10.1016/j.solmat.2019.110196
Received 9 May 2019; Received in revised form 20 September 2019; Accepted 21 September 2019
Available online 24 September 2019
0927-0248/© 2019 Elsevier B.V. All rights reserved.

worth noting that, to make full use of the effect of work-function difference in carrier transportation, effective passivation of c-Si surface is critical needed to avoid pinning of Fermi level. Furthermore, the low work-function characteristic of metal electrodes in contact with the metal oxides or alkali metal salts ESTLs is also important for efficient electron transport, as emphasized by Cho et al. [20,21].

In the case of the bifacial SHJ solar cells, by using the wide band-gap metal oxides as the carrier selective layers, the parasitic absorption of the doped a-Si:H can be well reduced. For the IBC solar cells, the absorption losses related to the doped a-Si:H is no more an issue. But, we know that hazardous precursors are needed for doped a-Si:H prepared by PECVD and it is not an easy task to get p-type a-Si:H thin films with high conductivity. Therefore, finding suitable substitutes for doped a-Si:H thin films in IBC-SHJ solar cells is also a matter of importance. As we know, the fabrication techniques of the wide band-gap materials can be flexible and simple. For example, solution processed SnO_2 and TiO_2 are widely used in perovskite solar cells [22,23] and spin-coated ZnO are successfully applied to the SHJ solar cells to serve as the ESTL [24]. The fairly simple preparation techniques provide a great prospect in reducing the cost of silicon solar cells in the future. Therefore, the c-Si solar cells featuring dopant-free asymmetric heterocontacts (DASH) are very promising and have attracted more and more attention. An efficiency of 19.4% has been achieved on a DASH solar cell with a MoO_x HSTL and a LiF_x ESTL [12]. Adopting the new type ESTL and HSTL is also a promising way to reduce the excessive manufacturing costs of the IBC-SHJ solar cells.

However, performance degradation of the devices associated with high temperature intolerance of the high work-function oxides (MoO_x, WO_x, and V_2O_5) [11,25,26] is an obstacle for the stable and efficient DASH solar cells. It was found that both the transparent conductive oxide (TCO) sputtering process itself and the following annealing step (to recover the passivation quality reduced by the sputtering, about 180 °C) cause the deterioration of the MoO_x thin film [11,27]. In order to avoid the unfavorable processes and simplify the fabrication process at the same time, a novel lithography-free, dopant-free, and TCO omitted IBC-SHJ solar cell structure was demonstrated. The interdigitated back contact was formed by using metal masks rather than photolithography. TiO_2 prepared by sol-gel method and MoO_x prepared by hot-wire reactive-sublimation deposition (HWRSD) [28] were used as the ESTL and HSTL, respectively. By using a HWRSD WO_x as the effective antireflection layer, a champion efficiency up to 20.24% was achieved on the lithography-free and dopant-free IBC-SHJ solar cells.

2. Experimental details

2.1. Preparation of WO_x, MoO_x, and TiO_2 thin films

MoO_x and WO_x thin films were prepared by hot-wire reactive-sublimation deposition. In a deposition chamber with oxygen atmosphere, molybdenum or tungsten wires purchased from Alfa Aesar with purity of 99.99% and diameter of 1 mm were used as the hot wires. During the deposition, MoO_x or WO_x molecules are generated on the surface of the hot molybdenum or tungsten wires and are sublimated directly into the chamber. The MoO_x or WO_x molecules then adsorb, diffuse, coalesce and finally form the MoO_x or WO_x films on the substrate. During the deposition, the substrate temperature was lower than 70°C. The hot wire temperature, oxygen flow rate and deposition pressure were set to be 1095 ± 5°C, 4 sccm, 0.2 Pa for MoO_x, and 1200°C ± 5°C, 4 sccm, 3Pa for WO_x, respectively.

TiO_2 thin films were prepared by sol-gel method. The TiO_2 sol was purchased from Shanghai Mater Win New Materials Co., Ltd and was diluted with butanol to obtain the TiO_2 sol solution with the concentration of 0.15 wt%. The TiO_2 sol solution was spin-coated on the rear side of the solar cells at 7000 rpm to form the TiO_2 thin film as described below.

2.2. Characterization

Surface morphology of the TiO_2, MO_x and WO_x thin films on c-Si wafers were characterized by scanning electron microscope (SEM, Hitachi SU8010). Elemental analysis of the TiO_2 film was characterized by energy-dispersive spectrometer (EDS, Bruker 6–30). Contact interfaces were observed by transmission electron microscopy (TEM, JEOL JEM-2100Plus). Transmittance and reflectance were measured by spectrophotometer (Hitachi UV4100). Film thickness and surface profile were obtained by step profiler (DektakXT). Photocurrent density-voltage (J-V) curves of the solar cells were obtained under AM1.5 (100 mW/cm2, 25 °C) illumination. Effective minority lifetime (τ_{eff}) and recombination current density (J_0) were determined by the quasi-steady-state photoconductance (QSSPC) and transient photoconductance decay (TrPCD) methods in a standard Sinton WCT-120 system.

2.3. Fabrication process of the devices

N-type (100)-oriented CZ silicon wafers with a thickness of 220 μm and a resistivity of 1–5 Ω cm were used as the substrates. After alkaline texturing, they were chemically cleaned according to the standard RCA procedure.

The sketch of the devices fabrication process is shown in Fig. 1. In step1, intrinsic a-Si:H thin films (~6 nm) as the passivation layers were deposited on both sides of the n-type c-Si substrates by PECVD at 200 °C. Then, the WO_x antireflection layer with the thickness of about 120 nm was deposited on the front side of the devices by HWRSD as step 2 shows. In step 3, the MoO_x HSTL with a thickness of about 15 nm and Ag/Al electrode were successively deposited by HWRSD and thermal evaporation on the back side of the devices screened with a metal mask A (Figure S1 a). After removing the metal mask A, the back side of the devices was UV-O_3 processed for 8min, and the TiO_2 sol was spin coated on the whole back side and then annealed at 140°C for 5min to form the ESTL as shown in step 4. Finally, Mg/Al/Ag metal electrode was screen-evaporated on the back side of the devices through the metal mask B (Figure S1 b) to finish the device fabrication. The electrode structure of the back side of the devices is shown in the lower-left corner of Fig. 1. The gap width between the electrodes of Ag/Al and Mg/Al/Ag is about 50 μm. The total area of the back contacts (gray part in the bottom view of the device in Fig. 1) is about 1.5 cm^2. During light J-V measurements, a metal shadow mask with the size of 1 × 1 cm^2 was used to restrict the illumination and make an aperture area of 1 cm^2 for the devices.

3. Results and discussion

The SEM images of the pyramid-textured silicon wafers covered with MoO_x, WO_x, and TiO_2 are shown in Fig. 2a–c. We can see that all of the metal oxide films are compact and show nice coverage on textured Si. For the MoO_x and WO_x thin films deposited using HWRSD, benefiting from the efficient gas-phase and surface diffusion of MoO_x and WO_x molecules, conformal coverages on textured Si substrates were achieved. As for the TiO_2 film fabricated by spin-coating, although the image of the film section is not clear enough to be used to determine the film thickness, it can be seen that the pyramids are completely covered by TiO_2 without bare regions and the shape of the pyramids is well maintained. It is well known that formation of nice covered oxides on textured silicon wafer with sharp pyramids by spin-coating is challenging [24]. Substrate wettability, rotation speed, and solution concentration are all important factors. High rotation speed and low solution concentration are generally required for achieving good film coverage by spin-coating [24]. To confirm the coverage of the spin-coated TiO_2 on the pyramid-textured silicon wafers, top-view SEM image and the corresponding elemental EDS mappings of Ti and Si were obtained as shown in Fig. 2 d-f. The uniform element distribution of Ti confirms the full coverage of the pyramids by the solution-processed TiO_2 film, which

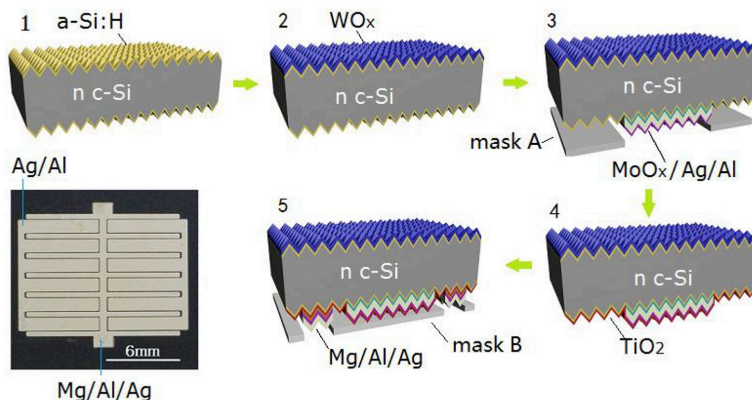

Fig. 1. Schematic of the fabrication process (step1-step5) of the lithography-free and dopant-free IBC-SHJ solar cells. A bottom view of the device is shown in the lower-left corner.

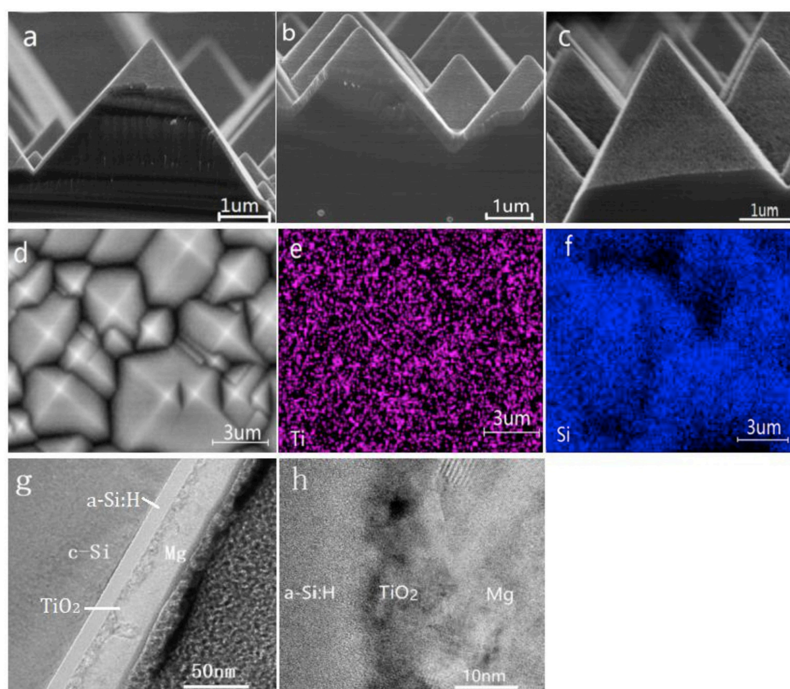

Fig. 2. (a, b, and c) Cross-sectional SEM images of pyramid-shaped Si surfaces covered with MoO_x, WO_x, and TiO_2, respectively. (d) Top-view SEM image of a pyramid-textured silicon wafer covered with TiO_2. (e, f) The corresponding EDS elemental mappings of Ti and Si elements. (g) TEM image of a c-Si/a-Si:H(i)/SiO_x/TiO_2/Mg structure based on a planar silicon substrate. (h) A local high resolution TEM image around the TiO_2 layer. (For interpretation of the references to colour in this figure legend, the reader is referred to the Web version of this article.)

shows the feasibility of using spin-coated TiO_2 film as the ESTL of a textured c-Si solar cell. However, the element distribution of Si seems not uniform. The darker regions in the Si map should be attributed to the thicker TiO_2 films in the deep “valleys” between the pyramids. The thick TiO_2 layer at the bottom of the pyramids is detrimental to the carrier collection. Nevertheless, benefiting from a long diffusion length of the c-Si substrate, electrons can be well collected by the thinner TiO_2 layer at the upper part of the pyramids. The TEM image of a c-Si/a-Si:H (i)/SiO_x/TiO_2/Mg structure based on a planar silicon substrate is shown in Fig. 2g. Fig. 2h shows a local high resolution TEM image around the TiO_2 layer. The thickness of the spin-coated TiO_2 layer can be identified to be about a dozen nanometers. The thickness of the UV-O_3 SiO_x layer is about 2.4 nm according to the Ellipsometric spectrometer measurement (Fig. S2). The thickness of 2.4 nm of the UV-O_3 SiO_x layer would be too thick for a uniform tunneling transport [29]. However, based on the fact that the SiO_x layer was formed by treating the amorphous Si with UV-O_3, pinhole-like transport [29] or defect-assisted tunneling could ensure the transport of the carries through the SiO_x layer [30].

Due to the wide band-gap character, WO_x has been widely investigated as the HSTL [14] of the c-Si heterojunction solar cells. Here,

considering the matching of the refractive indexes between WO_x and c-Si, WO_x was used as an antireflection layer of the IBC-SHJ solar cells. The transmittance of WO_x on glass substrate and the reflectance of WO_x on textured silicon wafer are given in Fig. 3. For each kind of substrate, WO_x thin films with four different thicknesses were prepared. The WO_x thin films show quite good transmission and the average transmission is larger than 97% between 400 and 1100 nm. The transmittance of WO_x is slightly higher than that of SiN_x [31] which is the most widely used antireflection materials in c-Si solar cells. The antireflection effect of WO_x on textured silicon wafer is also significant. With the decrease of the WO_x thickness, the reflection minimum moves toward the short wavelength region. Although the reflectance in long wavelength region increases slightly as the WO_x thickness decreases, the WO_x film with the thickness of 120 nm shows the best antireflection effect (the average reflectivity is 2.98% between 400 and 1100 nm). Considering the reflectance and transmittance at the same time, the thickness of the WO_x antireflection layer of the IBC-SHJ solar cells was controlled to be at about 120 nm.

It is known that both a-Si:H and SiO_x layers play important roles in SHJ solar cells. In most cases, the intrinsic a-Si:H can make an excellent passivation of the SHJ interfaces, which determines the V_{oc} of the IBC-SHJ devices [32,33]. In general, the SiO_x layer also serves as a good passivation layer, which is helpful to improve the solar cell efficiency [34]. Our previous work shows that an a-Si:H(i)/UV-O_3 SiO_x combination passivation layer is beneficial for the SHJ solar cells with SnO_2 as the ESTL [35]. However, we also find that the a-Si:H(i)/SiO_x combination layer does not always work well when it comes into contact with other metal oxides. Therefore, to determine the appropriate passivation processes, three IBC-SHJ solar cells with different passivation layers were fabricated. For the first sample, a-Si:H(i) is the only adopted passivation layer between the c-Si and the MoO_x or TiO_2. The HSTL and ESTL have the structures of a-Si:H(i)/MoO_x and a-Si:H(i)/TiO_2, respectively. For the second sample, before the MoO_x or TiO_2 layer preparation, a thin SiO_x layer was formed by a short time UV-O_3 processing of the a-Si:H(i) passivation layer. So, the HSTL and ESTL have the stacking structures of a-Si:H(i)/SiO_x/MoO_x and a-Si:H(i)/SiO_x/TiO_2, respectively. For the third sample, the UV-O_3 process was only performed before the TiO_2 spin-coating step. The HSTL and ESTL of the third sample are a-Si:H(i)/MoO_x and a-Si:H(i)/SiO_x/TiO_2, respectively.

The light J-V curves of the three samples are shown in Fig. 4 and the corresponding PV parameters are summarized in Table 1. The series resistances were obtained through the analysis of the light J-V curve based on the diode model [36]. First of all, we noticed that fairly good open circuit voltages (V_{oc}) are obtained for all the three samples, which

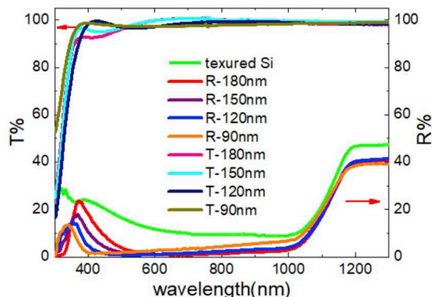

Fig. 3. Transmittance of the WO_x films on glass substrates and reflectance of the WO_x films on textured silicon wafers. Four different thicknesses of the WO_x films were considered. Influence of the glass substrate on the transmittance has been deducted by place a glass substrate in the reference light path. The green line is the reflectivity of a textured silicon wafer. (For interpretation of the references to colour in this figure legend, the reader is referred to the Web version of this article.)

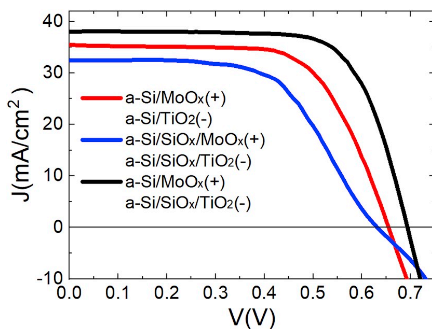

Fig. 4. Light J-V curves of the lithography-free and dopant-free IBC-SHJ solar cells with different ESTL and HSTL. (+) and (−) represent HSTL and ESTL, respectively.

Table 1
Photovoltaic parameters of the lithography-free and dopant-free IBC-SHJ solar cells with different ESTL and HSTL. The light J-V measurements were carried out with an aperture area of 1 cm^2. The series resistances were obtained through the analysis of the light J-V curve based on the diode model. It needs to clarify that the series resistance value of sample 2 cannot be compared directly to the other two solar cells due to the S shape of the J-V curve.

No.	HSTL	ESTL	Voc (mV)	Jsc (mA/cm2)	FF (%)	Eff (%)	Rss (Ω)
1	a-Si:H(i)/MoO_x	a-Si:H(i)/TiO_x	654	35.16	67.07	15.42	4.77
2	a-Si:H(i)/SiO_x/MoO_x	a-Si:H(i)/SiO_x/TiO_2	631	32.19	60.20	12.22	13.21
3	a-Si:H(i)/MoO_x	a-Si:H(i)/SiO_x/TiO_2	691	37.92	72.34	18.90	3.11

indicates good isolation between the Ag/Al and Mg/Al/Ag electrodes on the back side of the solar cells. This demonstrates the feasibility of replacing lithography with mask technology in the fabrication process of the IBC solar cells. In addition, it is worth mentioning that the spin-coated TiO_2 covered the entire back surface of the devices during the fabrication process, as depicted in Fig. 1. We believe that the high resistance of the dopant-free TiO_2 layer also plays a positive role in reducing the transverse leakage between the electrodes.

Next, comparing the first and the third samples with different ESTL structures, we found that the UV-O_3 SiO_x layer shows good effect on the solar cell performance when it is inserted between the a-Si:H(i) and the TiO_2 layer. An efficiency (Eff) of 18.90% was achieved for the third device with the a-Si:H(i)/MoO_x HSTL and the a-Si:H(i)/SiO_x/TiO_2 ESTL. However, by comparing the second device with the third one (different HSTL), we can conclude that the UV-O_3 SiO_x layer is harmful when contacting with the MoO_x layer which makes the lowest efficiency of the second solar cell. By analyzing the photovoltaic parameters of the three devices, we can also conclude that, confined to our samples at present stage, the negative effect caused by the SiO_x/MoO_x contact outweighs the good effect brought by the SiO_x/TiO_2 contact. Thus, the performance of the sample 1 is better than that of the sample 2.

According to Kita et al. [37], electric dipoles are likely formed at the metal oxides/SiO_x interface due to the oxygen movement driven by the oxygen density difference. The direction of the oxygen movement determines the direction of the interface dipoles which may promote or hinder the transport of carriers at the ESTL and HSTL. We attribute the opposite effect of the silicon oxide layer on the HSTL and ESTL to the interface dipoles. The dipoles with the direction from TiO_2 to SiO_x

produce a downward band bending at the SiO_x/TiO_2 contact which can be regarded as a field-effect passivation and is beneficial for electron selective transportation in the ESTL. On the contrary, the dipoles with the direction from MoO_x to SiO_x at the SiO_x/MoO_x interface hinder the transport of holes. The occurance of S shaped light J-V characteristic of the second device reflects the influence of the additional energetic barrier on the carrier collection.

For the devices whose ESTL or HSTL cannot provide efficient carrier collection (sample 1 and sample 2), in addition to the reduction of the V_{oc}, the inefficient carrier collection can also cause drops in J_{sc} and FF, even though the optical absorptions of the devices are the same, as shown in Fig. 4 and Table 1. Similar phenomena have been found on other dopant-free SHJ solar cells [20,36].

The above discussion mainly compares the different impact of SiO_x/MoO_x and SiO_x/TiO_2 on the performance of the devices. To fully reveal the role of the UV-O_3 SiO_x in the interface passivation, the effective carrier lifetimes (τ_{eff}) as a function of excess carrier density for textured Si wafers passivated bifacially by a-Si:H(i), a-Si:H(i)/SiO_x, a-Si:H(i)/TiO_2, and a-Si:H(i)/SiO_x/TiO_2 were measured and depicted in Fig. 5. The Si wafers covered with TiO_2 were annealed at 140 °C for 5 min after spin coating to remove the solvent and some additives of TiO_2 sol. For the Si wafer passivated by a-Si:H(i)/SiO_x, the effective lifetime was measured before and after annealing (a-Si:H(i)/SiO_x-A). An effective carrier lifetime curve of a Si wafer passivated by a-Si:H(i)/WO_x is also included in Fig. 5.

First of all, the passivation effect of our a-Si:H(i) is acceptable if the size effect was considered and the Si wafer bifacially passivated by the a-Si:H(i) is taken to be a reference for other samples. Comparing with the reference wafer, the effective carrier lifetimes of the wafers with the a-Si:H(i)/SiO_x and a-Si:H(i)/TiO_2 passivation layers decrease significantly, which indicates that the interface passivated by the a-Si:H(i) was damaged by the UV-O_3 process (SiO_x) and also the sol-gel method (TiO_2). The reason why the UV-O_3 SiO_x and sol-gel TiO_2 damage the passivation quality so seriously needs to be further investigated. The τ_{eff} curve of the a-Si:H(i)/TiO_2 passivated sample is higher than that of the a-Si:H(i)/SiO_x sample, which is probably due to the annealing process used during the TiO_2 preparation that recovered the damaged interface to some extent. Furthermore, fixed positive charges possibly exist in the SiO_x and TiO_2 layers. The extreme decrease of the lifetime in the low injection region for the a-Si:H(i)/SiO_x and a-Si:H(i)/TiO_2 passivated samples are probably caused by the fixed positive charges [38].

To confirm the annealing effect, the τ_{eff} of the a-Si/SiO_x passivated wafer was measured again after annealing (140°C for 5min, curve a-Si/SiO_x-A). The τ_{eff} is recovered significantly after annealing, especially in the low injection region, which indicates that annealing is helpful to eliminate both interface defects and interface fixed charges. However, we need to note that higher annealing temperature will destroy the MoO_x/a-Si:H/c-Si contact in the devices [11].

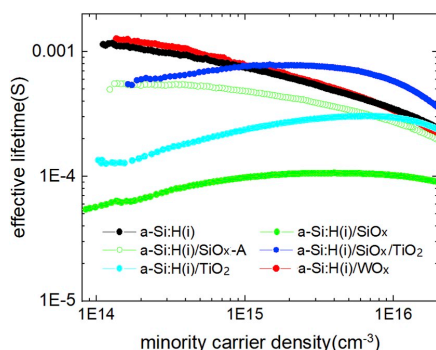

Fig. 5. Effective carrier lifetimes as a function of excess carrier density for textured silicon wafers bifacially passivated by a-Si:H(i), a-Si:H(i)/SiO_x, a-Si:H(i)/TiO_x, a-Si:H(i)/SiO_x/TiO_2 and a-Si:H(i)/WO_x layers. The effective carrier lifetime curve of a-Si:H(i)/SiO_x-A was measured after annealing at 140°C for 5min. The samples for effective carrier lifetime measurement are about 5 cm × 5 cm in size. (For interpretation of the references to colour in this figure legend, the reader is referred to the Web version of this article.)

For the wafer passivated by the stack structure of a-Si/SiO_x/TiO_2, the lifetime is also recovered significantly compared with the a-Si/SiO_x or a-Si/TiO_2 passivated samples. As discussed above, annealing used during the TiO_2 preparation is beneficial for the lifetime recovering. In addition, dipoles [37] are probably formed at the SiO_x/TiO_2 interface, which play a positive role in the interface passivation and promote the electron selective transportation as well.

Finally, we can also see from Fig. 5 that the τ_{eff} curves are almost identical for the Si wafers passivated by a-Si:H(i) and a-Si:H(i)/WO_x. This indicates that, for the a-Si:H(i)/WO_x sample, the passivation effect is mainly determined by the a-Si:H(i) layer. The extremely slight increase of τ_{eff} in the low injection region for the a-Si:H(i)/WO_x sample compared with the reference sample implies a quite weak field-effect passivation of the WO_x. The equivalent τ_{eff} of a-Si:H(i) and a-Si:H(i)/WO_x passivated samples also shows that the HWRSD process does not damage the interface quality at all, which makes the HWRSD WO_x a good choice of the antireflection layer in the IBC-SHJ solar cells.

The recombination current density (J_0) of the textured silicon wafer bifacially covered with different stack layers were measured at the same time, as shown in Table 2. The values of J_0 show consistent behavior with the effective lifetime for different passivation layers. A lowest J_0 of 13.1A fA/cm^2 was obtained for the textured silicon wafer passivated with a-Si:H(i)/SiO_x/TiO_2 stack layer.

Finally, an efficiency of 20.24% was achieved on a champion lithography-free IBC-SHJ device with a-Si:H(i)/SiO_x/TiO_2, a-Si:H(i)/MoO_x, and WO_x as the ESTL, HSTL, and antireflection layer, respectively. Except the metal electrodes and the a-Si:H(i) passivation layers, all other functional films in the IBC-SHJ solar cell are dopant-free metal oxides. Light J-V curve of the champion IBC-SHJ solar cell is shown in Fig. 6a. The fairly high V_{oc} of 696 mV and J_{sc} of 38.6 mA/cm^2 showcase the great potential of the lithography-free and dopant-free IBC-SHJ solar cell. The external quantum efficiency (EQE) and 1-R (reflectance) spectra of the champion IBC-SHJ solar cell are shown in Fig. 6b. The integrated photocurrent density (38.12 mA/cm^2) calculated from the EQE data is in good agreement with the measured short circuit current density (38.61 mA/cm^2) of the solar cell, which indicates that the light J-V measurement procedure is correct. From the gap between EQE and 1-R spectra, it can be seen that the short circuit current need to be further improved.

Energy band diagram of the dopant-free SHJ solar cell with TiO_2 ESTL and MoO_x HSTL is sketched in Fig. 6c. Although an additional layer of TiO_2 was formed on the top of the HSTL layer due to our device fabrication steps, considering that the TiO_2 layer is not directly formed on MoO_x but on Ag/Al electrode and the thickness of the TiO_2 layer is about 10 nm, the possible influence of TiO_2 on the band diagram of the HSTL side is neglected. On the premise that the interfaces are well passivated, MoO_x and TiO_2 lead to the strong band bending of the c-Si in the surface regions, which provide efficient carriers collection for the SHJ solar cells. This is the essential advantage of the DASH solar cells using high or low work-function dopant-free carrier selective contacts over the traditional pn junction type devices depended on doped Si.

Table 2
J_0 of the textured silicon wafers bifacially covered with different passivation layers.

	a-Si:H (i)	a-Si:H(i)/ SiO_x	a-Si:H(i)/ TiO_2	a-Si:H(i)/ SiO_x/TiO_2	a-Si:H(i)/ WO_x
J_0 (fA/cm^2)	51.6	422.3	326.3	13.1	34.9

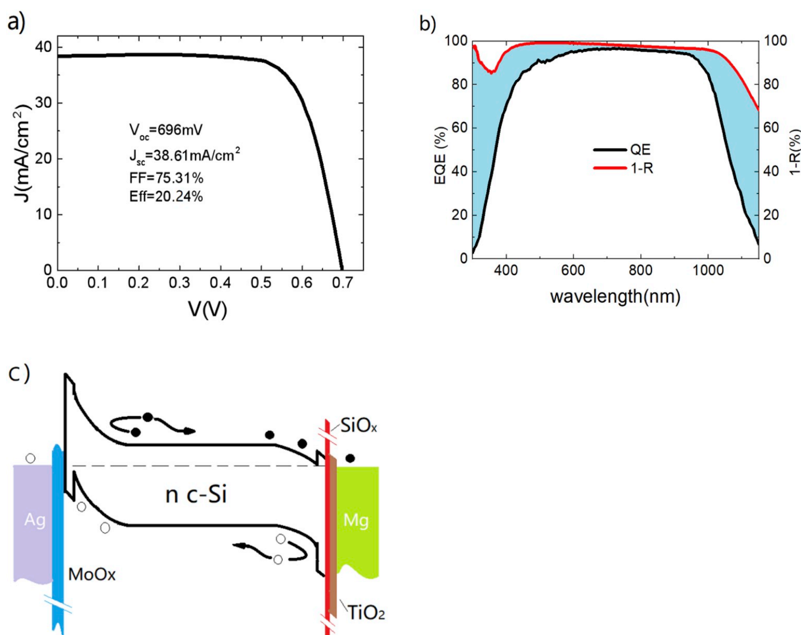

Fig. 6. (a) Light J-V curve of the champion lithography-free IBC-SHJ solar cell (aperture area = 1 × 1 cm^2) with an a-Si:H(i)/SiO_x/TiO_2 ESTL, an a-Si:H(i)/MoO_x HSTL, and a WO_x antireflection layer. (b) The EQE and 1-R spectra of the champion IBC-SHJ solar cell. (c) The sketched energy band diagram of c-Si solar cell with TiO_2 ESTL and MoO_x HSTL.

Our lithography-free and dopant-free IBC-SHJ solar cell shows advantages over the double-side contact DASH devices [11,12]. First, J_{sc} higher than that of the DASH solar cells was achieved on our IBC-SHJ solar cell, which should be attributed to the back contact configuration. Furthermore, owing to the absence of the TCO layer, the possible deterioration of the MoO_x thin film caused by the TCO fabrication process and the following annealing step can be avoided. Thus the related performance degradation of the devices can be avoided and higher efficiency can be expected.

The fabrication process of our lithography-free and dopant-free IBC-SHJ solar cells show advantages in many aspects compared with the IBC devices based on doped a-Si:H. The preparation processes of the TiO_2 and MoO_x are both simpler than that of the doped a-Si:H in which expensive PECVD system and toxic precursors are needed. It should be pointed out that, although the preparation process of TiO_2 is quite simple, the non-uniform coverage in the spin-coated TiO_2 on textured Si surface may lead to an increase in contact resistance and then have a detrimental influence on FF of the devices. If spin coating can be replaced by a spray or mist deposition technique, the contact quality could probably be improved in the future. Moreover, for IBC-SHJ solar cells based on doped a-Si:H, although TCO free Al back contacts can be used as presented by Stang et al. [39], a layer stack of TCO/Ag are still widely adopted as the back contacts [9]. For our IBC-SHJ solar cells, both the TiO_2 and MoO_x can contact directly with both Ag and Al electrodes without the transition of TCO.

4. Conclusions

The lithography-free and dopant-free IBC-SHJ solar cells with a-Si:H (i)/SiO_x/TiO_2 layer stack as the ESTL, a-Si:H(i)/MoO_x as the HSTL, and WO_x as the antireflection layer were successfully fabricated. Mask technology was used to replace photolithography during the fabrication of the back contact devices. The TiO_2 layer was fabricated using spin-coating and the MoO_x and WO_x layers were deposited by a simple HWRSD technique. For the ESTL, insertion of a thin SiO_x layer between the a-Si:H(i) and TiO_2 greatly improves the solar cell performance due to the enhanced passivation effect of the a-Si:H(i)/SiO_x/TiO_2 layer stack. An efficiency of 20.24% was achieved on the champion IBC-SHJ device with oxide ESTL, HSTL and antireflection layer.

The novel IBC-SHJ solar cells have the advantages of both DASH and IBC solar cells. Compared with the IBC-SHJ devices using doped a-Si:H as the carrier selective transport layers and using photolithography to form the interdigitated contact, the fabrication costs of the novel IBC-SHJ solar cells can be significantly reduced by using the simple mask technology, solution process, and HWRSD technique. This work highlights the potential of the lithography-free and dopant-free technologies in high-efficiency and low-cost c-Si heterojunction solar cells with interdigitated back contact.

Acknowledgments

This work was supported by the National Key R&D Program of China (2018YFB1500102) and the National Natural Science Foundation of China (No.61604153 and No.61674150). Support from the Sino-Danish Center for Education and Research (SDC) is fully acknowledged.

Appendix A. Supplementary data

Supplementary data to this article can be found online at https://doi.org/10.1016/j.solmat.2019.110196.

References

[1] K. Yoshikawa, H. Kawasaki, W. Yoshida, T. Irie, K. Konishi, K. Nakano, T. Uto, D. Adachi, M. Kanematsu, H. Uzu, K. Yamamoto, Silicon heterojunction solar cell with interdigitated back contacts for a photoconversion efficiency over 26%, Nature Energy 2 (2017) 8.

[2] K. Masuko, M. Shigematsu, T. Hashiguchi, D. Fujishima, M. Kai, N. Yoshimura, T. Yamaguchi, Y. Ichihashi, T. Mishima, N. Matsubara, T. Yamanishi, T. Takahama, M. Taguchi, E. Maruyama, S. Okamoto, Achievement of more than 25% conversion efficiency with crystalline silicon heterojunction solar cell, IEEE J. Photovolt. 4 (2014) 1433–1435.

[3] F. Haase, C. Hollemann, S. Schafer, A. Merkle, M. Rienacker, J. Krugener, R. Brendel, R. Peibst, Laser contact openings for local poly-Si-metal contacts enabling 26.1%-efficient POLO-IBC solar cells, Sol. Energy Mater. Sol. Cells 186 (2018) 184–193.

[4] K. Yoshikawa, W. Yoshida, T. Irie, H. Kawasaki, K. Konishi, H. Ishibashi, T. Asatani, D. Adachi, M. Kanematsu, H. Uzu, K. Yamamoto, Exceeding conversion efficiency of 26% by heterojunction interdigitated back contact solar cell with thin film Si technology, Sol. Energy Mater. Sol. Cells 173 (2017) 37–42.

[5] M.A. Green, Y. Hishikawa, W. Warta, E.D. Dunlop, D.H. Levi, J. Hohl-Ebinger, A.W. Y. Ho-Baillie, Solar cell efficiency tables (version 50), Prog. Photovolt. 25 (2017) 668–676.

[6] M.L. Xu, T. Bearda, M. Filipic, H.S. Radhakrishnan, I. Gordon, J. Szlufcik, J. Poortmans, Simple emitter patterning of silicon heterojunction interdigitated back-contact solar cells using damage-free laser ablation, Sol. Energy Mater. Sol. Cells 186 (2018) 78–83.

[7] A. Tomasi, B. Paviet-Salomon, Q. Jeangros, J. Haschke, G. Christmann, L. Barraud, A. Descoeudres, J.P. Seif, S. Nicolay, M. Despeisse, S. De Wolf, C. Ballif, Simple processing of back-contacted silicon heterojunction solar cells using selective-area crystalline growth, Nature Energy 2 (2017), 17062.

[8] M. Despeisse, L. Barraud, B.P. Salomon, A. Descoeudres, L. Senaud, C. Allebé, J. Levrat, J. Horzel, A. Lachowicz, F. Debrot, J. Champliaud, A. Faes, N. Badel, J. Geissbühler, S.M. Nicolas, G. Christmann, J. Diaz, L. Ding, S. Nicolay, C. Ballif, Engineering of thin film silicon materials for high efficiency crystalline silicon solar cells, in: Proceedings of 2018 IEEE 7th World Conference on Photovoltaic Energy Conversion, WCPEC, 2018, https://doi.org/10.1109/PVSC.2018.8547369.

[9] D. Lachenal, P. Papet, B. Legradic, R. Kramer, T. Kössler, L. Andreetta, N. Holm, W. Frammelsberger, D.L. Baetzner, B. Strahm, L.L. Senaud, J.W. Schüttauf, A. Descoeudres, G. Christmann, S. Nicolay, M. Despeisse, B. Paviet-Salomon, C. Ballif, Optimization of tunnel-junction IBC solar cells based on a series resistance model, Sol. Energy Mater. Sol. Cells 200 (2019) 110036.

[10] Y.S. Kim, C. Mo, D.Y. Lee, S.C. Park, D. Kim, J. Nam, J. Yang, D. Suh, H.J. Kim, H. Park, S.J. Park, D. Kim, J. Song, H.S. Lee, S. Park, Y. Kang, Gapless point back surface field for the counter doping of large-area interdigitated back contact solar cells using a blanket shadow mask implantation process, Prog. Photovolt. 25 (2017) 989–995.

[11] J. Geissbuhler, J. Werner, S.M. de Nicolas, L. Barraud, A. Hessler-Wyser, M. Despeisse, S. Nicolay, A. Tomasi, B. Niesen, S. De Wolf, C. Ballif, 22.5% efficient silicon heterojunction solar cell with molybdenum oxide hole collector, Appl. Phys. Lett. 107 (2015), 081601.

[12] J. Bullock, M. Hettick, J. Geissbuhler, A.J. Ong, T. Allen, C.M. Sutter-Fella, T. Chen, H. Ota, E.W. Schaler, S. De Wolf, C. Ballif, A. Cuevas, A. Javey, Efficient silicon solar cells with dopant-free asymmetric heterocontacts, Nature Energy 1 (2016) 7.

[13] C. Battaglia, X.T. Yin, M. Zheng, I.D. Sharp, T. Chen, S. McDonnell, A. Azcatl, C. Carraro, B.W. Ma, R. Maboudian, R.M. Wallace, A. Javey, Hole selective MoO_x contact for silicon solar cells, Nano Lett. 14 (2014) 967–971.

[14] M. Mews, L. Korte, B. Rech, Oxygen vacancies in tungsten oxide and their influence on tungsten oxide/silicon heterojunction solar cells, Sol. Energy Mater. Sol. Cells 158 (2016) 77–83.

[15] M. Mews, A. Lemaire, L. Korte, Sputtered tungsten oxide as hole contact for silicon heterojunction solar cells, IEEE J. Photovolt. 7 (2017) 1209–1215.

[16] O. Almora, L.G. Gerling, C. Voz, R. Alcubilla, J. Puigdollers, G. Garcia-Belmonte, Superior performance of V_2O_5 as hole selective contact over other transition metal oxides in silicon heterojunction solar cells, Sol. Energy Mater. Sol. Cells 168 (2017) 221–226.

[17] G. Masmitja, L.G. Gerling, P. Ortega, J. Puigdollers, I. Martin, C. Voz, R. Alcubilla, V_2O_x-based hole-selective contacts for c-Si interdigitated back-contacted solar cells, J. Mater. Chem. 5 (2017) 9182–9189.

[18] X.B. Yang, Q.Y. Bi, H. Ali, K. Davis, W.V. Schoenfeld, K. Weber, High-performance TiO_2-based electron-selective contacts for crystalline silicon solar cells, Adv. Mater. 28 (2016) 5891.

[19] Y.M. Wan, C. Samundsett, J. Bullock, M. Hettick, T. Allen, D. Yan, J. Peng, Y.L. Wu, J. Cui, A. Javey, A. Cuevas, Conductive and stable magnesium oxide electron-selective contacts for efficient silicon solar cells, Adv. Energy Mater. 7 (2017) 16177.

[20] J. Cho, J. Melskens, M. Recaman Payo, M. Debucquoy, H. Sivaramakrishnan Radhakrishnan, I. Gordon, J. Szlufcik, W.M. Kessels, J. Poortmans, Performance and thermal stability of an a-Si: H/TiO_x/Yb stack as an electron-selective contact in silicon heterojunction solar cells, ACS Appl. Energy Mater. 2 (2019) 1393–1404.

[21] J. Cho, J. Melskens, M. Debucquoy, M. Recamán Payo, S. Jambaldinni, T. Bearda, I. Gordon, J. Szlufcik, W. Kessels, J. Poortmans, Passivating electron-selective contacts for silicon solar cells based on an a-Si: H/TiO_x stack and a low work function metal, Prog. Photovolt. Res. Appl. 26 (2018) 835–845.

[22] Q. Jiang, L.Q. Zhang, H.L. Wang, X.L. Yang, J.H. Meng, H. Liu, Z.G. Yin, J.L. Wu, X. W. Zhang, J.B. You, Enhanced electron extraction using SnO2 for high-efficiency planar-structure $HC(NH_2)(2)PbI_3$-based perovskite solar cells, Nature Energy 2 (2017) 1–7.

[23] N.J. Jeon, J.H. Noh, Y.C. Kim, W.S. Yang, S. Ryu, S.I. Seok, Solvent engineering for high-performance inorganic-organic hybrid perovskite solar cells, Nat. Mater. 13 (2014) 897–903.

[24] J.N. Ding, Y.R. Zhou, G.Q. Dong, M. Liu, D.H. Yu, F.Z. Liu, Solution-processed ZnO as the efficient passivation and electron selective layer of silicon solar cells, Prog. Photovolt. 26 (2018) 974–980.

[25] S. Essig, J. Dreon, E. Rucavado, M. Mews, T. Koida, M. Boccard, J. Werner, J. Geissbuhler, P. Loper, M. Morales-Masis, L. Korte, S. De Wolf, C. Ballif, Toward annealing-stable molybdenum-oxide-based hole-selective contacts for silicon photovoltaics, Solar RRL 2 (2018) 1700227.

[26] T. Zhang, C.-Y. Lee, Y. Wan, S. Lim, B. Hoex, Investigation of the thermal stability of MoO_x as hole-selective contacts for Si solar cells, J. Appl. Phys. 124 (2018), 073106.

[27] D. Sacchetto, Q. Jeangros, G. Christmann, L. Barraud, A. Descoeudres, J. Geissbuhler, M. Despeisse, A. Hessler-Wyser, S. Nicolay, C. Ballif, ITO/MoO_x/a-Si:H(i) hole-selective contacts for silicon heterojunction solar cells: degradation mechanisms and cell integration, IEEE J. Photovolt. 7 (2017) 1584–1590.

[28] http://arxiv.org/abs/1902.09127.

[29] A.S. Kale, W. Nemeth, H. Guthrey, E. Kennedy, A.G. Norman, M. Page, M. Al-Jassim, D.L. Young, S. Agarwa, P. Stradins, Understanding the charge transport mechanisms through ultrathin SiO_x layers in passivated contacts for high-efficiency silicon solar cells, Appl. Phys. Lett. 114 (2019), 083902.

[30] J. Kang, Y.-H. Kim, J. Bang, K.J. Chang, Direct and defect-assisted electron tunneling through SiO_2 layers from first principles, Phys. Rev. B 77 (2008) 195321.

[31] E.A. Davis, N. Piggins, S.C. Bayliss, optical-properties of amorfhous SiN_x(H) films, J. Phys. C Solid State Phys. 20 (1987) 4415–4427.

[32] H.-D. Um, N. Kim, K. Lee, I. Hwang, J.H. Seo, K. Seo, Dopant-free all-back-contact Si nanohole solar cells using MoO_x and LiF films, Nano Lett. 16 (2016) 981–987.

[33] W. Weiliang, L. Wenjie, Z. Sihua, B. Paviet-Salomon, M. Despeisse, L. Zongcun, M. Boccard, S. Hui, C. Ballif, 22% efficient dopant-free interdigitated back contact silicon solar cells, AIP. Conf. Proc. 1999 (2018), 040025.

[34] X. Yang, K. Weber, Z. Hameiri, S. De Wolf, Industrially feasible, dopant-free, carrier-selective contacts for high-efficiency silicon solar cells, Prog. Photovolt. 25 (2017) 896–904.

[35] M. Liu, Y. Zhou, G. Dong, W. Wang, F. Liu, D. Yu, SnO_2/Mg combination electron selective transport layer for Si heterojunction solar cells, Sol. Energy Mater. Sol. Cells 200 (2019) 109996.

[36] B.V. Zeghbroeck, in: Principles of Semiconductor Devices, University of Colorado, Boulder CO, 2006. http://ecee.colorado.edu/~bart/book/book/index.html.

[37] K. Kita, A. Toriumi, Origin of electric dipoles formed at high-k/SiO_2 interface, Appl. Phys. Lett. 94 (2009), 132902.

[38] C. Leendertz, N. Mingirulli, T.F. Schulze, J.P. Kleider, B. Rech, L. Korte, Discerning passivation mechanisms at a-Si:H/c-Si interfaces by means of photoconductance measurements, Appl. Phys. Lett. 98 (2011), 202108.

[39] J. Stang, T. Franssen, J. Haschke, M. Mews, A. Merkle, R. Peibst, B. Rech, L. Korte, Optimized metallization for interdigitated back contact silicon heterojunction solar cells, Sol. RRL 1 (2017) 1700021.

Supplementary Information:

Lithography-free and Dopant-free Back-contact Silicon Heterojunction Solar Cells with Solution-processed TiO_2 as the Efficient Electron Selective Layer

Yurong Zhou[1*],Qunfang Zhang[2], Zongheng Sun[1], Fengchao Li[1], Zhenghao Liu[1], Zhengxiong Cai[1], Yuqin Zhou[1], Fengzhen Liu[1*]

1.Center of Materials Science and Optoelectronics Engineering & College of Materials Science and Opto-Electronic Technology, University of Chinese Academy of Sciences, 100049, Beijing, China
2. Hanenergy Mobile Energy Holding Group

Supplementary note 1: The photographs of metal masks A and B

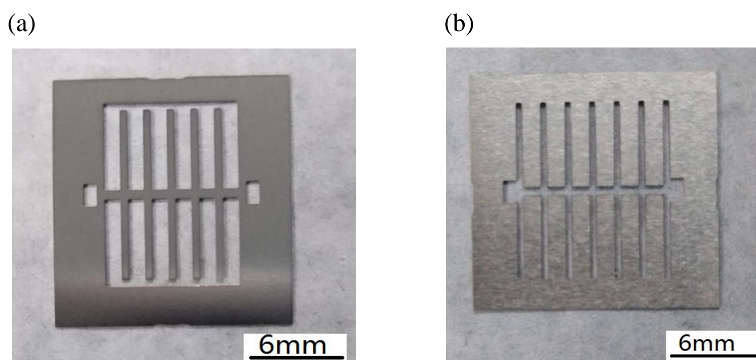

Figure S1 (a) Photograph of the metal mask A used for the MoO_x HSTL and Ag/Al electrode deposition. (b) Photograph of metal mask B used during the evaporation of Mg/Al/Ag metal electrode.

Supplementary note 2: Thickness of the oxide layer on the a-Si:H film formed by UV-O_3 photo-oxidization was analyzed by ellipsometric spectrometer. The measured and fitted delta-wavelength curves are shown in Figure S1. The fitting result shows that the SiO_x layer is about 2.4nm with the refractive index of 1.45.

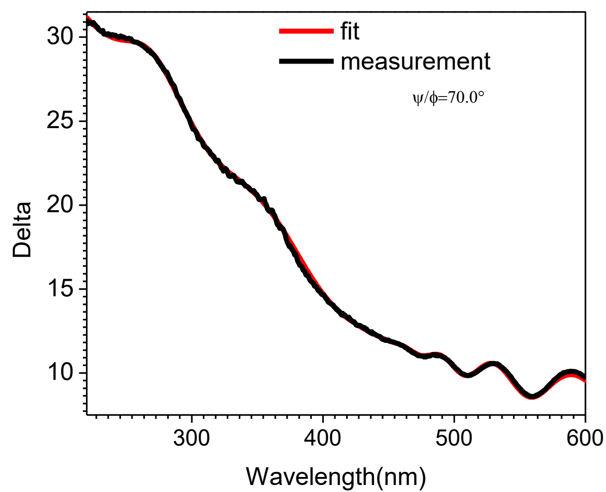

Figure S2 Ellipsometric spectrometer measurement and fitting results of UV-O3 treated a-Si:H(i) film(about 500nm) on the polished crystalline silicon substrate. The treatment time was 8 minutes.

ISSN (online): 2446-1636
ISBN (online): 978-87-7210-803-2
AALBORG UNIVERSITY PRESS